ALBERTO CANALI

STRONGLY INTERACTING MIXTURES OF ^{161}Dy AND ^{40}K

STRONGLY INTERACTING MIXTURES OF ^{161}Dy AND ^{40}K

ALBERTO CANALI

universität
innsbruck

Feshbach Molecules and Hydrodynamic crossover

February 2025 – classicthesis v4.8

Ohana means family.
Family means nobody gets left behind, or forgotten.

— Lilo & Stitch

Dedicated to the loving memory of Rudolf Miede.

1939 – 2005

ABSTRACT

Short summary of the contents in English. . . a great guide by Kent Beck how to write good abstracts can be found here:

https://plg.uwaterloo.ca/~migod/research/beckOOPSLA.html

ZUSAMMENFASSUNG

Kurze Zusammenfassung des Inhaltes in deutscher Sprache. . .

[January 13, 2026 at 11:47 – classicthesis v4.8]

PUBLICATIONS

This might come in handy for PhD theses: some ideas and figures have appeared previously in the following publications:

Attention: This requires a separate run of bibtex for your refsection, e. g., ClassicThesis1-blx for this file. You might also use biber as the backend for biblatex. See also http://tex.stackexchange.com/questions/128196/problem-with-refsection.

CONTENTS

ACRONYMS

MOT mageto-optical trap

ODT optical dipole trap

QGM quantum gas microscope

Part I

INTRODUCTION

ULTRACOLD GASES AND QUANTUM MIXTURES

It is only in very recent times that it has begun to dawn upon the mind of man that there is another world only one degree less complex and wonderful than the stellar universe – the world of molecules and atoms

— Albert A. Michelson [1]

1.1 WHY COLD ATOMS?

Right at the turn of the 20th century
why it is so interesting and relevant, great tunabilty, great test field
Atoms are the most fundamental components that we can control with great precision

1.2 QUANTUM MIXTURES

increase of the possibility to study
BEC-BCS crossover here

1.3 FROM FERMIONIC SPIN MIXTURES TO HETERO-NUCLEAR MIXTURES

Describe why mass imbalance and some description of the result obtained with other mixtures and describe why Dy-K is our choice
Zaccanti's varenna notes have a lot of good reference on this

1.4 OUR CHOICE: DY-K

Explorative experimentm, first lanthanide+alkali
This works in explaining another advantage (or difference) that comes with using Dy Evaporative cooling in a fermionic experiment requires some extra tricks compared to a bosonic system. The lack of interaction between identical particles prevent the realization of evaporative cooling in a single component atomic cloud. In the early years of ultracold fermionic quantum matter two approaches were successfull in cooling to degeneracy an atomic could. The method developed by the group of Debbie Jin at JILA consisted in evaporative cool a bosonic rubidium cloud while sympathetic cooling a sample of fermionic potassium atoms. Thje

The two main approaches are to either use an another atomic species for which efficient evaporative cooling

sysmpathtic cooling for K, with either rubidium cita Jin et al and

Li has prove very successful felikx, despite the wrong mass ration of the two clouds. This approach has been also very successful in the more exotic mixture of Li and Cr, despite requiring an extra step (Feshbach cooling) to achieve complete thermalization.

The large dipole moment of highly magnetic atoms like Er and Dy

In standard fermionic experiments, evaporative cooling is performed between two spin states of the same atomic species, in order to allow for the interaction necessary for rethermalization.

In other heteronuclear fermionic mixture like the LiK and LiCr experiments, the typical procedure is to perform evaporative cooling of one of the species, lithium in particular, in two spin states, while the other atomic specie is sympathetic cooled to degeneracy. With highly magnetic atoms, like Dy and Er, quantum degeneracy can be reached in a single spin state, thanks to universal dipolar scattering

SCATTERING THEORY AND FESHBACH RESONANCES

2.1 BASIS OF SCATTERING THEORY

2.2 FESHBACH RESONANCES IN ULTRACOLD GASES

THESIS OUTLINE

Part II

DʏK MIXTURE: THE QUEST FOR AN ISOLATED
FESHBACH RESONANCE

DʏK EXPERIMENT

While ultracold atoms laboratories are in general on the technically heavy side of table-top experiments, the Dy-K machine is a challenging set up even for the standards of the community. While recently the flourishing of ultracold atomic experiments where new, controlled, complexity is added, mostly in the form of quantum gas microscope (QGM), use to selectively control individual atoms in lattices or projecting arbitrary potential. The Dy-K set up, while focusing on bulk physics in harmonic traps, proves to be a cumbersome at times. For example, a standard ultracold experiment working with an alkali atom in a bulk system, typically uses one or two lasers resonant with the D2 and D1 lines for cooling, in the mageto-optical trap (MOT) and grey molasses stages, and one or two high power infrared beam for trapping and evaporative cooling. Working with an heteronuclear mixture requires additional resonant laser sources for the different transitions of the various atomic species. Moreover, lanthanides atoms like dysprosium, erbium, europium cite present a richer electronic structure, which can be used to produce colder sub-μK atomic samples before evaporative cooling, as is the case in the Dy-K experiment. this part to be reduced a bit

When I joined the team at the end of 2021, the experiment was already fully operational. Many important results were already successfully achieved, in particular regarding the preparation of the doubly degenerate mixture [2], the precise measurement of dysprosium polarizability [3, 4], the observation of interspecies Feshbach resonance [5], and intr [6]. In this chapter, I will first briefly summarize, in Sec. 4.1, the procedure developed to obtained the doubly-degenerate Fermi mixture, while in Sec. 4.2, I will describe the results already obtained concerning the investigation of interaction in the mixture [5] and in Dy alone [6].

4.1 EXPERIMENTAL SEQUENCE AT A GLANCE

In this section I will give an overview of the sequence routinely used in the our experiment to produce the doubly degenerate mixture. This procedure is the result of many years of cumulative work from past and current generations [2, 7–10], and it is presented here in its most updated form.

In our experiment we use on of the two fermionic isotope of dysprosium, ^{161}Dy, combined with the only fermionic isotope of potassium, ^{40}K. We employ an all optical approach to cool the mixture to de-

generacy. Due to the different magnetic moments of the two atomic species, the magnetic field gradients applied during the MOT are very different, requiring a sequential loading. Since the magnetic gradient used for potassium is about 5 times stronger than the one needed for dysprosium, it is convenient to first load the K MOT and then the Dy one, in order to avoid large losses in the Dy cloud.

Potassium is loaded in to the 3D MOT from its atomic source, a 2D MOT prepared in a separated glass cell. Both 3D and 2D MOTs operate on the potassium D2 line at 767 nm (linewidth $\Gamma_{D2}/2\pi \sim 6\,\text{MHz}$), and all the light beams are generated with the same source[1]. After the MOT, potassium is further cooled by performing gray molasses on the D1 line (wavelength 770 nm with linewidth $\Gamma_{D1}/2\pi \sim 6\,\text{MHz}$), reaching a temperature of around 30 μK, with an almost ($\sim 80\%$) spin polarised sample in the lowest hyperfine state $|9/2, -9/2\rangle$. During the grey molasses cooling, the K cloud is transferred in a large volume reservoir crossed optical dipole trap (ODT), operating in the near infrared at a wavelength of 1064 nm[2]. add some ref on the general preparation of K in other systems, see also pra cornee

Once potassium is trapped in the reservoir ODT, the preparation of the Dy cloud can start. The dysprosium atomic source is a high-temperature effusion oven, operating at around 1000 °C. The atomic beam is then decelerated using a Zeeman slower, operating along the broad transition at 421 nm ($\Gamma_{421}/2\pi \sim 32\,\text{MHz}$). The slowed atomic beam is capture in a 3D MOT generated at the narrow intercombination transition at 626 nm (linewidth $\Gamma_{626}/2\pi \sim 135\,\text{kHz}$). Thanks to narrowness of transition used in the MOT, the cold atomic sample obtained is already spin polarized in the lowest hyperfine state [11], that is the stretched state $|21/2, -21/2\rangle$. At the end of the compressed MOT stage, the temperature of the atomic cloud is approximately 8 μK. After the compressed MOT the Dy cloud is also transferred in the same reservoir ODT of K.

Before the evaporative cooling stage, necessary to reach the degenerate regime, Dy undergoes an additional resonant cooling stage[3], performed near the narrow transition at 741 nm, with linewidth $\Gamma_{741}/2\pi \sim 1.7\,\text{kHz}$ [13]. We perform this cooling stage after transferring the atomic clouds in an elongated ODT. Thanks to this cooling stage, we manage to reach temperatures around 1 μK with the Dy cloud. More details on the narrow-line cooling sequence are reported in Sec. 5.6.2. It is worth noticing here that, while as reported in [12] no effect of the 741 nm light are observed on the potassium component, the rapid changes in the trap configuration, strongly affects the potassium cloud, which loses a sizeable amount of atoms. This does not strictly affect the efficiency of evaporative cooling, and has not been a limiting factor

---

1 Toptica TA Pro
2 Azurlight ALS-IR-1064-5-I-CC-SF
3 This additional stage was implemented in the experiment before I joined the team, but reported for the first time in Ref. [12], which is part of this thesis as chapter 5.

in most of the experiments presented in this thesis, but reduces the tunability of the potassium atom number. This limitation and possible solutions are also discussed in Chapter one of the concluding chapters.

At the end of the 741 nm cooling stage, the atomic mixture is transferred in 300 ms in a crossed ODT generated at 1064 nm. This trap is formed by two tightly focused beams[4], an horizontal one with waist 25 µm, and a vertical one with waist of 60 µm. The tighter waist of the trap compared to the reservoir is chosen to increase the density, and improve thermalization.

Contrary to other fermionic experiments, for highly magnetic lanthanides, it is possible to perform evaporative cooling with a single spin state, thanks to universal dipolar scattering [14, 15]. In our case, we perform evaporative cooling with Dy in its lowest hyperfine state, while also sympathetically cool K. At the end of the evaporative cooling sequence, we are able to reach the deeply degenerate regime, with typical numbers of $N_{Dy} = 1.2 \times 10^5$, $T_{Dy}/T_F^{Dy} \approx 0.13$ and $N_K = 2.5 \times 10^4$, $T_K/T_F^K \approx 0.1$.

Evaporative cooling in the Dy-K mixture has been found to be most effective for low magnetic field, below 500 mG. Above this field, for temperatures $\gtrsim 1\,\mu K$, strong three-body losses in Dy, also observed in Er [16], prevent efficient cooling. A more detailed discussion on Dy intraspecies interaction is reported in the next section, while a discussion regarding the limitations of evaporative cooling in specific is reported in Sec. second to last chapter.

During the years, other trapping beams were aligned on the atoms to explore the role of trapping-light wavelength in our experiments (a good portion of Part III is dedicated to this investigation). For the purpose of the mixture preparation, it is important to mention here that after discovering the beneficial role of the 1547-nm light on the molecules lifetime, two beams, one horizontal and on vertical, generated at this wavelength[5], were permanently added to the experiment. In particular, the horizontal beam, with waist 90 µm, has been successfully employed during the evaporative cooling sequence, allowing us to reach the same degeneracy conditions, with an higher number of dysprosium atoms, and in a more robust way, i.e. with less optimization required in the day-by-day running of the experiment. In Fig. 4.1, I present a recap of the ODT scheme, with the two additional 1547 beam and an *exp beam*, which represents all of the additional beams at different wavelengths tested during my PhD.

4.2 FESHBACH RESONANCES IN DY-K

Once degeneracy is obtained, the main ingredient missing in order to approach the study of crossover physics is a suitable Feshbach

---

4 Both generated from the Mephisto MOPA 18 NE
5 NKT Koheras BOOSTIK E15
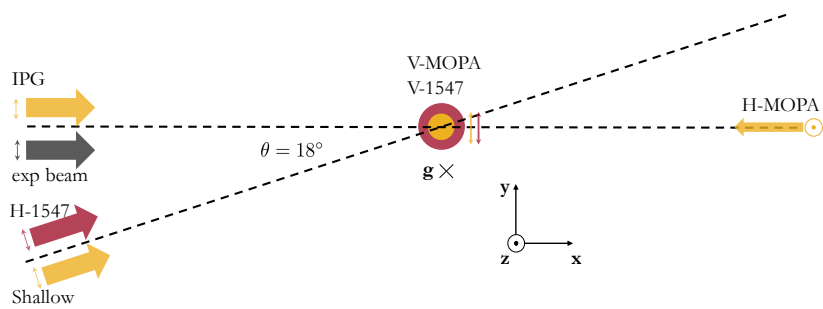
Figure 4.1: ODT setup in the Dy-K experiment. In yellow are reported the trapping beam with a wavelength of 1064 nm, while in red the one with a wavelength of 1547 nm. The grey path is for all the other different ODTs tested during the years and reported in Chapter 10. Double arrows and the circle-dot indicate the polarization of the beams (linear or circular).

resonance to tune interspecies interaction. As previously mentioned, the sheer complexity of the Dy-K system prevented any theoretical prediction of the interaction spectrum.

Scan of the magnetic field up to 400G... Suitable resonances individuated around 200 G... Thermalization measure... Hydrodynamic expansion to prove strong interaction at 217 G.

However not well isolated... Difficulties in keeping the degeneracy when ramping to high field... No preparation achieved at higher fields... Need to investigate why... look into Dy interaction alone... Study of loss spectrum at low field 1 G range... more than 40 resonance found...

-Investigation of the low field behavior of Dy alone to try to understand why no evaporative cooling at higher field –> Dy has a shit on of resonance even in a single spin state.

WTF.

Gross.

FML. Necessary to improve B field control

With better resolution worth trying to recheck also lower fields for narrower features
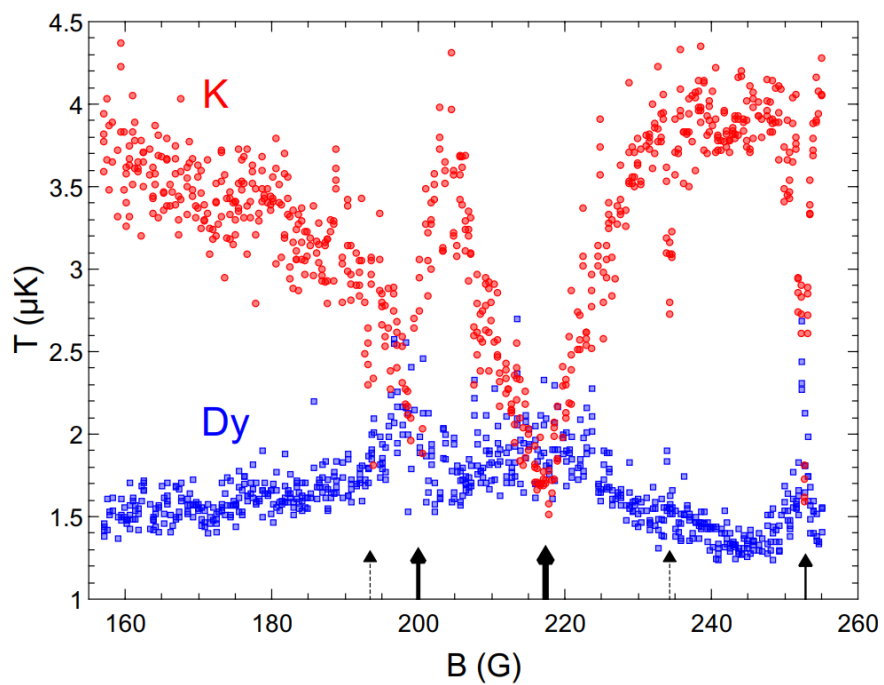
Figure 4.2: Figure taken from Ref. [5]
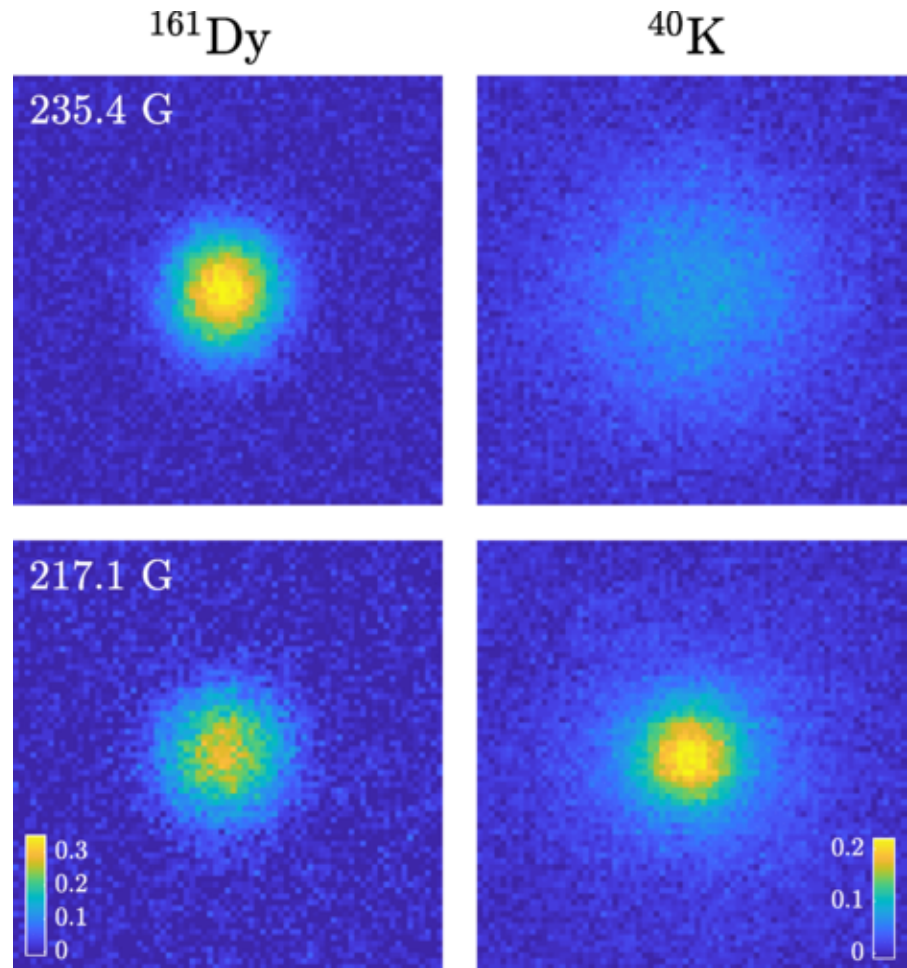
Figure 4.3: Figure taken from Ref. [5]
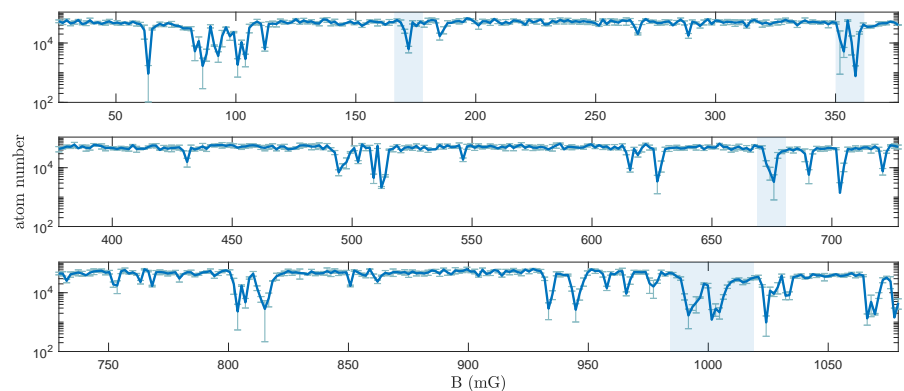
Figure 4.4: Figure taken from Ref. [6]

Published as Editor's Suggestion:

Zhu-Xiong Ye, Alberto Canali, Elisa Soave, Marian
Kreyer, Yaakov Yudkin, Cornelis Ravensbergen, Emil
Kirilov, and Rudolf Grimm.

Author contribution: The author took a supporting role in the
process of acquiring and analyzing the data described in this
publication as well as writing the manuscript.

[January 13, 2026 at 11:47 – classicthesis v4.8]

We report on the observation of Feshbach resonances at low magnetic-field strength (below 10 G) in the Fermi-Fermi mixture of ^{161}Dy and ^{40}K. We characterize five resonances by measurements of interspecies thermalization rates and molecular binding energies. As a case of particular interest for future experiments, we consider a resonance at 7.29 G, which combines accurate magnetic tunability and access to the universal regime of interactions with experimental simplicity. We show that lifetimes of a few hundred milliseconds can be achieved for the optically trapped, resonantly interacting mixture. We also demonstrate the hydrodynamic expansion of the mixture in the strongly interacting regime and the formation of DyK Feshbach molecules. Our work opens up experimental possibilities in view of mass-imbalanced superfluids and related phenomena.

5.1   INTRODUCTION

Exciting research avenues in the field of quantum gases rely on the possibility to control interactions via magnetically tuned Feshbach resonances [17]. For ultracold systems composed of fermionic atoms [18], such resonances play a major role in pair formation and eventually in the creation of fermionic superfluids [19–21]. The majority of experiments on resonantly interacting fermions have been carried out on spin mixtures of fermionic species, which naturally imposes a limitation on equal-mass systems. Beyond that, theoretical work has predicted fermionic quantum gases with mass imbalance to favor exotic interaction regimes [22]. Mass-imbalanced systems hold particular promise in view of superfluid states with unconventional pairing mechanisms [23–25], most notably the elusive Fulde-Ferrell-Larkin-Ovchinnikov (FFLO) state [26–28].

Ultracold heteronuclear Fermi-Fermi mixtures have so far been produced in the laboratory using four different combinations of fermionic atoms: ^{6}Li-^{40}K [29–32], ^{6}Li-^{173}Yb [33, 34], ^{161}Dy-^{40}K [2, 5], and ^{6}Li-^{53}Cr [35–37]. Feshbach resonances have been found in all these combinations, but (with one exception [5]) they all turned out to be quite narrow. On the practical side, this limits the possibility of accurate experimental interaction tuning. On a more fundamental side, the narrowness imposes severe limitations to universal behavior in the resonance region [17] and thus also compromises the great benefit of fermionic loss suppression in a strongly interacting fermion mixture [38–40]. The only exception is a rather broad resonance that we recently identified in the Dy-K mixture at a field of 217 G [5]. Its experimental application, however, turned out to be challenging because of complications owing to the exceptionally rich structure of both Dy-K interspecies and Dy intraspecies resonances, which lead to a complex

behavior of inelastic losses [6, 41]. This has motivated our search for alternative Feshbach resonances in the Dy-K system.

In this article, we report on the observation and characterization of five interspecies Feshbach resonances in the low-field region (below 10 G). Although all of them belong to the class of narrow resonances [17], they offer very interesting properties for experiments. Most notably, we find that a resonance near 7.29 G offers the possibility of accurate magnetic tuning in combination with access to resonant interactions in the universal regime. In Sec. 5.2, we briefly introduce the basic properties of narrow Feshbach resonances. In Sec. 5.3, we present a survey of the resonances in the low-field region, characterizing their strengths and the binding energies of the underlying molecular states. In Sec. 5.4, we consider the particularly interesting 7.29-G resonance in more detail. We demonstrate that this low-field resonance offers an application potential similar to the 50 times wider resonance at 217 G, but with less experimental complications. As examples, we present the hydrodynamic expansion of the mixture and the formation of DyK Feshbach molecules. In Sec. 6.6, we finally summarize the main conclusions of our work.

5.2 NARROW FESHBACH RESONANCES

Near a single, isolated s-wave Feshbach resonance, elastic scattering is described by the scattering length a as a function of the magnetic field strength B, following the expression [17, 42]

$$a(B) = a_{\text{bg}} - \frac{A}{B - B_0}\, a_0 \,. \tag{5.1}$$

Accordingly, the near-resonant scattering behavior in the zero-energy limit is fully characterized by a set of three parameters: the resonance position B_0, the background scattering length a_{bg}, and the strength parameter A. The latter is related to the common definition of a resonance width Δ by $A = \Delta\, a_{\text{bg}}/a_0$ and provides a direct measure for the strength of the resonance pole. The Bohr radius a_0 is used as a convenient unit of length.

To characterize a narrow (closed-channel dominated) Feshbach resonance [17], an additional parameter is needed. Following Ref. [43] it is convenient to introduce the range parameter

$$R^* = \frac{\hbar^2}{2m_{\text{r}}a_0\, \delta\mu\, A} \tag{5.2}$$

as an additional length scale, where m_{r} denotes the reduced mass and $\delta\mu$ represents the differential magnetic moment between the molecular state (closed channel) underlying the resonance and the

atomic scattering state (entrance channel). Using this definition, the binding energy of the molecular state can be modeled as [43, 44]

$$E_{\mathrm{b}} = \frac{\hbar^2}{8\,(R^*)^2\,m_{\mathrm{r}}} \left(\sqrt{1 - \frac{4R^*(B - B_0)}{a_0 A}} - 1 \right)^2. \tag{5.3}$$

In addition to that, R^* also characterizes the effective range of scattering, corresponding to the momentum dependence at low, but finite collision energies.

For $|a| \gg R^*$, i.e. in a narrow range of magnetic detunings $|B - B_0| \ll A\,a_0/R^*$, one recovers universal behavior as it is the case for broad (entrance-channel dominated) resonances. The molecular binding energy then reduces to the universal expression $E_{\mathrm{b}} = \hbar^2/(2m_{\mathrm{r}}a^2)$. An important experimental benefit of the universal regime is also the Pauli suppression of inelastic losses [38–40].

5.3 SURVEY OF LOW-FIELD FESHBACH RESONANCES

In this Section, we present a survey of the interspecies Feshbach resonances that we found in the magnetic field range from 0 to 10 G. In Sec 5.3.1, we summarize the main experimental sequence for the preparation of the ultracold Dy and K mixture. In Sec. 5.3.2, we introduce interspecies thermalization scans to detect the resonances and to estimate their relative strengths. In Sec. 5.3.3, we describe measurements of the binding energy for each resonance and their analysis by the model introduced in the preceding Section.

5.3.1 *Preparation of the mixture*

The starting point of our experiments is a Fermi-Fermi mixture of ^{161}Dy and ^{40}K atoms in a crossed-beam optical dipole trap (ODT), realized with near-infrared (1064 nm) light. The preparation procedure is based on our previous work [2], with implementation of an additional narrow-line (741 nm) in-trap cooling stage for Dy and further optimizations as described in detail in Appendix 5.6. Both species are spin polarized in their lowest hyperfine sublevels $|F, m_F\rangle = |21/2, -21/2\rangle$ and $|9/2, -9/2\rangle$, respectively.

Under typical experimental conditions, forced evaporative cooling results in a mixture of $N_{\mathrm{Dy}} = 8 \times 10^4$ and $N_{\mathrm{K}} = 9 \times 10^3$ atoms in a trap with mean (geometrically averaged) oscillation frequencies of $\bar{\omega}_{\mathrm{Dy}}/2\pi = 150\,\mathrm{Hz}$ and $\bar{\omega}_{\mathrm{K}}/\bar{\omega}_{\mathrm{Dy}} = 3.60$ [3] at a temperature of $T_{\mathrm{Dy}} = 70\,\mathrm{nK}$. This corresponds to deeply degenerate conditions with $T_{\mathrm{Dy}}/T_F^{\mathrm{Dy}} = 0.13$, where $T_F^{\mathrm{Dy}} = \hbar\bar{\omega}_{\mathrm{Dy}}(6N_{\mathrm{Dy}})^{1/3}/k_B$ denotes the Dy Fermi temperature. The K temperature $T_{\mathrm{K}} = 90\,\mathrm{nK}$ is somewhat higher than for Dy because of a possibly incomplete interspecies thermalization in the final stage of the evaporation [2] but, in any case, we
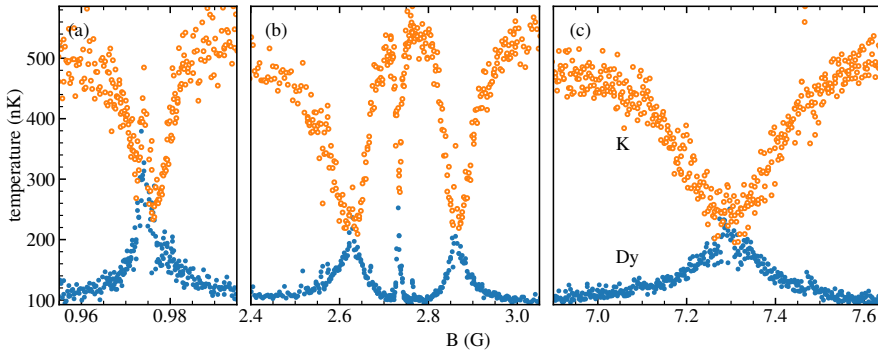
Figure 5.1: Interspecies thermalization scans revealing five Feshbach resonances below 10 G. The hold time is 50 ms for (a) and 100 ms for (b) and (c). Note the ten-fold extended B-field scale in (a) as compared to (b) and (c). Further note the narrow heating feature observed near 7.47 G, which indicates an additional ultranarrow Feshbach resonance.

reach deep degeneracy also for the K component with $T_K/T_F^K \approx 0.09$. The improvement with respect to our previous work [2] is essentially due to the additional narrow-line cooling stage for Dy described in Appendix 5.6, which provides us with a lower initial temperature before evaporation. The final temperature of the sample can be controlled by variation of the endpoint of evaporation, and the number ratio N_{Dy}/N_K by the initial conditions for loading the ODT from a laser-cooled sample.

While evaporative cooling is carried out at a magnetic field of 230 mG, where we found three-body losses to be extremely low [6], experiments near interspecies Feshbach resonances in general require a transfer of the sample to higher magnetic fields. The system then inevitably has to cross many interspecies Dy-K resonances and intraspecies Dy resonances, the latter exhibiting an extremely large density of narrow Feshbach resonances (typically 50 resonances per gauss [6]). To minimize loss and heating we decompress the sample by loading it adiabatically into a very shallow ODT with $\bar{\omega}_{Dy}/2\pi = 39$ Hz before we quickly (within a few ms) ramp up the magnetic field to its target value.

The shallow ODT is very sensitive to the effect of gravity, in particular for the heavy Dy atoms. Holding Dy in such a trap requires magnetic levitation [2, 45]. A full compensation of the gravitational force for Dy is achieved by a gradient of 2.83 G/cm. A gradient slightly below this value (2.69 G/cm) leads to the 'magic' levitation condition introduced in Ref. [46], where both species experience the same gravitational sag and thus feature maximum overlap in the trap. A controlled deviation from this condition gives us a handle to vary the spatial overlap between the two species. This also allows us to separate both species, still keeping them in the trap. In this way, detrimental effects

of interspecies resonances can be avoided during the transfer to the target magnetic field. This is of particular importance if many interspecies resonances need to be crossed to reach the final field, as is the case for experiments near the strong 217-G resonance [5]. Under optimized conditions, we can accomplish a transfer of a deeply cooled mixture from the evaporation field to target fields up to $\sim$10 G without significant losses and with minimal heating to $T_{\mathrm{Dy}}/T_F^{\mathrm{Dy}} = 0.16$. Note, however, that most of the experiments reported here are carried out at higher temperatures with moderately degenerate or near-degenerate mixtures.

At the end of the sequence, standard absorption images are taken to record the optical depth of each species after time-of-flight expansion. K images are taken after a few ms, while the expansion time for Dy is typically twice as long. The imaging for experiments in this paper is performed at a magnetic field of 230 mG, except for the experiments on hydrodynamic expansion and Feshbach molecules (Secs. 5.4.3 and 5.4.5), which are imaged at a magnetic field near 7 G. For extracting the temperatures from the density profiles of deeply degenerate samples in the weakly interacting regime, we use fits based on the polylogarithmic function.

5.3.2 *Interspecies thermalization scan*

Interspecies thermalization provides us with a powerful tool to investigate elastic scattering between the two species [47]. In Ref. [5] we applied such measurements to characterize a scenario of broad overlapping Feshbach resonances in the ^{161}Dy-^{40}K mixture at high magnetic fields (150 - 250 G) and to identify a particularly strong one centered near 217 G. Here we proceed in an analogous way, focusing on the low-field region up to about 10 G.

We interrupt the evaporation after cooling the mixture to 110 nK with $N_{\mathrm{Dy}} = 3.3 \times 10^4$ and $N_{\mathrm{K}} = 1.8 \times 10^4$, and decompress the mixture to a low trap frequency of $\bar{\omega}_{\mathrm{Dy}}/2\pi = 45.2$ Hz and $\bar{\omega}_{\mathrm{K}}/2\pi = 164$ Hz. We apply species-selective parametric heating by modulating the intensity of the ODT at twice the vertical trapping frequency of K to induce a temperature difference between Dy and K. The temperature of K is increased to approximately 500 nK within 100 ms of parametric heating, while the temperature of Dy remains constant. At this point, the mixture is near thermal with $T_{\mathrm{Dy}}/T_F^{\mathrm{Dy}} \approx 0.9$ and $T_{\mathrm{K}}/T_F^{\mathrm{K}} \approx 1.3$. Afterwards, we ramp the magnetic field rapidly (within 5 ms) to the variable target field, where it is held for typically 100 ms to allow for interspecies thermalization. The fixed hold time is chosen for optimum contrast in the thermalization spectrum. We switch the magnetic field back to 230 mG within 5 ms, before carrying out time-of-flight diagnostics. The temperatures and atom numbers of Dy and

K are extracted from their density profiles after a 12-ms and a 5-ms time of flight, respectively.

We observe five interspecies resonances (along with a few ultranarrow, hardly resolved features) in the range from 0 to 10 G. Figure 5.1 [1] shows the temperatures reached for Dy and K after the hold time versus magnetic field. Away from the resonances, the temperatures are very close to their initial values because of the relatively small interspecies cross section associated with the background scattering length a_{bg} (see also Sec. 5.4.1). Close to a resonance, the enhanced interspecies collisions cause Dy and K atoms to reach thermal equilibrium rapidly. We identify two isolated resonances at 0.97 and 7.29 G, see Fig. 5.1 (a) and (c), and a group of three resonances at 2.61, 2.72, and 2.86 G, see Fig. 5.1 (b).

The observed thermalization behavior is consistent with the one expected for Feshbach resonances in s-wave scattering. In particular, the observed five features do not disappear at very low temperatures, in contrast to higher partial wave resonances identified in the dense spectra of magnetic lanthanide atoms [48, 49]. Our further analysis is therefore based on the assumption of an s-wave character and the model presented in Sec. 5.2.

The widths of the thermalization features contain information on the values of the strength parameter $A = \Delta a_{\mathrm{bg}}/a_0$ as characterizing the different resonances according to Eq. (5.1). Following our thermalization model [5, 47], the temperature difference decreases exponentially according to $\exp\left(-A^2 C t/(B - B_0)^2\right)$, where t is the hold time at the target magnetic field and C is a constant determined by the experimental parameters. Even without knowledge of the constant C, our features provide relative information on the values of A. Using the broadest feature (at 7.29 G) for normalization, we obtain A_{rel}= 0.06, 0.41, 0.05, 0.28, and 1 for our five resonances (in increasing field order). The relative A parameters indicate that the Feshbach resonances at 2.61 G and 2.86 G have a similar strength, which is about 1/2 to 1/3 of the value at 7.29 G. For the resonances at 0.97 G and 2.72 G, the A parameter values are about 20 times smaller than that of 7.29 G, showing that they are very narrow resonances. Compared with the much broader, previously observed resonance at 217 G [5], the value of A is about 60 times smaller for the 7.29-G resonance.

Note that the magnetic-field scan in Fig. 5.1(a) reveals a narrow heating feature, which is located slightly below the resonance center. We also observe (not shown) substantial three-body recombination losses right at this point and we thus interpret the heating as a manifestation of an anti-evaporation effect [50], resulting from losses in the center of the trap. The corresponding scan of the much broader resonance in Fig. 5.1(c) does not show such a heating feature, but we

---

1 See Supplemental Material on **Arxiv** or on the **APS** website for the data files of all figures.

find it to appear in measurements at longer hold times (see Sec. 5.4.4). We speculate that this behavior is a consequence of a stronger Pauli suppression of recombination losses for broader resonances.

In addition to the resonances presented here, we explore the Dy-K Feshbach resonances in the range of 10 to 20 G and 50 to 60 G. We observe two resonances located at 13.5 G and 15.3 G and 12 resonances distributed in the range of 51 to 55 G, with two isolated resonances located at 51.2 G and 54.9 G, respectively. Based on these observations we can give a rough estimate of one resonance per 1.5 G for the density of interspecies Feshbach resonances in the Dy-K system. This can be compared with a recent experimental investigation of Feshbach resonances in the Er-Li system [51], where about one resonance per 10 G was observed consistent with theoretical predictions [52]. The higher density in the Dy-K system can be (at least partially) attributed to the smaller rovibrational spacing resulting from the about six times larger reduced mass.

5.3.3 *Binding energy measurements*

To further characterize the observed *s*-wave Feshbach resonances, we measure the binding energy of the DyK dimer at the different resonances by wiggling the magnetic field [17, 53]. The mixture is prepared in the decompressed ODT with mean trap frequencies of $\bar{\omega}_{\mathrm{Dy}} = 2\pi \times 36.8\,\mathrm{Hz}$ and $\bar{\omega}_{\mathrm{K}} = 2\pi \times 132\,\mathrm{Hz}$ in thermal equilibrium with a temperature of $T \approx 370\,\mathrm{nK}$. To obtain a strong signal, the atom number ratio between Dy and K is prepared to be around 1:1 ($N_{\mathrm{Dy}} \approx N_{\mathrm{K}} \approx 3 \times 10^4$), and the magic levitation field is applied to ensure maximum overlap. The magnetic field is modulated in a frequency range between 10 kHz and 3 MHz. If the modulation frequency matches the binding energy of the DyK dimer at the selected magnetic field, the free atom pairs are associated into weakly bound molecules, which causes losses due to inelastic collisions. We adjust the modulation amplitude and duration to produce a clearly visible loss feature, where the loss of atoms is between 1/3 and 2/3 of the initial value. The typical magnetic field modulation amplitude and duration are roughly 400 mG and 200 ms, respectively. The loss features show typical widths of 20 to 40 kHz (full width at half maximum), and we fit them with a Lorentzian curve to determine the resonant frequency. We calibrate the magnetic field by measuring the frequency of the K transition $|F, m_F\rangle = |9/2, -9/2\rangle \rightarrow |9/2, -7/2\rangle$ as described in Appendix 5.7.

Figure 5.2 displays the binding energy versus magnetic field, measured near 1 G, 3 G, and 7 G. The solid curves show the best fits to the data according to Eq. (5.3), with B_0, A, and $\delta\mu$ as free parameters, and R^* is calculated from A and $\delta\mu$ using Eq. (5.2). The resulting parameter values are summarized in Table 5.1. In addition, we have carried
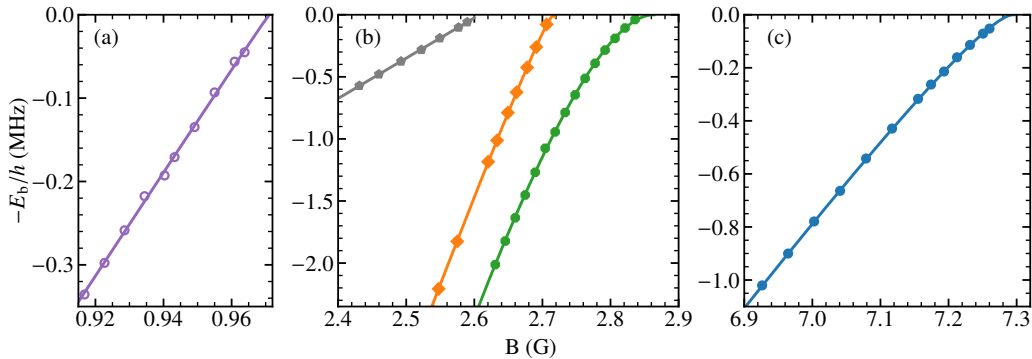
Figure 5.2: Binding energy of Feshbach molecules related to the observed resonances below 10 G. The symbols represent experimental data measured by wiggling the magnetic field, and the solid lines are the fitted curves based on Eq. (5.3). The uncertainties are smaller than the size of symbols. Note the five-fold extended B-field scale in (a) as compared to (b) and (c).

out binding energy measurements (data not shown) for the isolated resonance near 51 G and analyzed them in the same way. The results are included in Table 5.1.

Table 5.1: Parameters of the observed Feshbach resonances from fits of Eq. (5.3) to the measured binding energies. The uncertainties represent the 1σ statistical errors from the fit. They do not include additional uncertainties (2 mG for $B < 10$ G, and 10 mG for $B \approx 50$ G) from the magnetic field calibration, see Appendix 5.7. The symbol μ_B represents the Bohr magneton. Note that the three resonances near 3 G are presumably too close to each other to justify an interpretation in terms of isolated resonances, which obscures the physical meaning of the fit parameters (see text).

B_0 (G)	A (G)	$\delta\mu/\mu_B$	R^*/a_0
0.971(2)	0.6(2.3)	4.5(3)	$\gtrsim 3000$
2.608(2)	0.0(1.8)	2.3(1)	$\gtrsim 10^4$
2.717(1)	4.4(3)	11.1(1)	831(70)
2.864(1)	28.1(7)	22(1)	65(5)
7.295(1)	23.2(9)	2.71(3)	643(30)
51.242(2)	15(1)	4.2(1)	646(60)

It is important to note that the model underlying Eq. (5.3) is based on the assumption of a single, isolated resonance, not overlapping with other resonances. This is the case for the resonances at 0.97, 7.29, and 51.24 G, but not for the group of three resonances near 3 G. Even though the data can be well fitted by Eq. (5.3), the fit parameters will lose their direct physical meaning and they will no longer reflect the real physics. In particular, the value extracted for the strength parameter A will no longer correspond to the value of A that describes

the behavior of the scattering length near the pole according to Eq. (5.1).
In a similar way, the value extracted for the asymptotic differential
magnetic moment $\delta\mu$ may no longer reflect the magnetic moment of
the closed-channel molecule, and the true pole position may also be
somewhat shifted from the best fit value of B_0. In fact, comparing
the fitted A values for the overlapping resonances near 3 G with each
other and with the ones of the 7.29-G resonance shows that their
relative values do not correspond to the behavior observed in the
thermalization measurements. Also, the anomalously large fit value
for the differential magnetic moment of the 2.86-G resonance appears
likely as an artefact resulting from coupling between the different
closed channels of the overlapping resonances. A proper description
would require a more sophisticated coupled-channels model [54, 55],
which is beyond the scope of the present article.

The resonance at 7.29 G has no significant overlap with other res-
onances, and we can therefore expect Eqs. (5.1-5.3) to describe the
situation properly. The resulting value of the strength parameter ($A \approx$
23 G) highlights that a magnetic detuning of $|B - B_0| = 10$ mG already
leads to a large value for the scattering length of $|a| \approx 2400 a_0$. The uni-
versal range of the resonance (see the bending of the binding energy
curve in Fig. 5.2(c) near threshold) is realized for $|B - B_0| \ll A a_0 / R^* =$
36 mG. In experiments at low magnetic fields [6], control of the field
strength to a few mG is rather straightforward, and the resonance
thus appears to be well suited for exploring universal physics at large
values of the scattering length. Note that the resonance near 51 G offers
very similar properties, but at a higher magnetic field.

5.4   CASE STUDY OF THE 7.29-G RESONANCE

The 7.29-G resonance is the broadest Feshbach resonance with the
largest universal range that we found in the low-field range up to 10 G.
Moreover, it is well isolated from other resonances, which allows for a
description in terms of a two-channel model as underlying Sec. 5.2.
Even in the range of up to 300 G, it is one of very few resonances
offering similar properties. The low magnetic field facilitates accurate
experimental control, and it allows us to minimize atom loss and heat-
ing, which usually occurs when the field is ramped to its target value
and other resonances need to be crossed. Because of these favorable
properties, we examine this particular resonance more closely.

In Sec. 5.4.1, we start with presenting thermalization measurements
at different magnetic field strengths, from which we obtain the rela-
tionship between scattering length and magnetic field. In Sec. 5.4.2, we
investigate a possible light shift of the resonance by measuring binding
energies at different ODT depths. In Sec. 5.4.3, we present the hydro-
dynamic expansion of the strongly interacting mixture and investigate
its resonance behavior by comparing our experimental results with

Monte-Carlo simulation. In Sec. 5.4.4, we study inelastic losses in the vicinity of resonance and provide an estimate for the three-body loss rate at the pole position. In Sec. 5.4.5, we finally present the first results on the observation of DyK Feshbach molecules.

5.4.1   *Elastic scattering cross section and scattering length*

.

To determine the scattering length as a function of the magnetic field in the vicinity of the 7.29-G resonance, we measure the interspecies cross section between Dy and K atoms at different magnetic field strengths. The method is the same as we have already applied to the Dy-K mixture in our previous work [2, 5], and is based on the model introduced in Ref. [47]. The model describes how the interspecies scattering cross section σ can be extracted from the evolution of the temperature difference ΔT between Dy and K atoms.

As an example, Fig. 5.3(a) illustrates a typical thermalization process at 5.97 G. Here, the initial atom numbers are $N_{Dy} = 8 \times 10^4$ and $N_K = 1.7 \times 10^4$, and the mixture is prepared in a trap with $\bar{\omega}_{Dy} = 2\pi \times 88$ Hz and $\bar{\omega}_K = 2\pi \times 318$ Hz. After species-selective heating, see Sec. 5.3.2, the initial temperatures are $T_{Dy} = 0.5\,\mu K$ and $T_K = 2.5\,\bar{}K$. Both species approach thermal equilibrium on the time scale of 1 s. The orange solid line shows a numerical fit, which yields an interspecies scattering length of magnitude $|a| = 53(9)a_0$.

The gray dots in Fig. 5.3(b) show the values of the scattering length measured with the same method at different magnetic field strengths[2]. The corresponding signs are determined by the position of the magnetic field relative to the resonance pole. As a general fact, the sign of the scattering length is positive on the low-field side of a Feshbach resonance in the lowest spin channel. In this channel, the atom-pair state carries the maximum magnetic moment and thus always experiences a larger Zeeman shift than the molecular state underlying the Feshbach resonance.

The solid blue line shows the best fit based on Eq. (5.1). The parameter values show a background scattering length of $a_{bg} = +23(5)a_0$, which is smaller than earlier results of $|a_{bg}| \approx 62a_0$ obtained at 430 mG [2] and $|a_{bg}| \approx 60a_0$ in the 200-G region [5]. The resonance width according to the common definition [17] is $\Delta = Aa_0/a_{bg}$. For the width Δ and the position of the zero crossing $B_{zc} = B_0 + \Delta$, we obtain $\Delta = 0.94(21)$ G and $B_{zc} = 8.25(20)$ G from a fit with variable B_0, and $\Delta = 1.02(21)$ G and $B_{zc} = 8.32(21)$ G from a fit with B_0 fixed to 7.925 G, the value that was obtained from the binding energy measurements.

As shown in Table 5.2, thermalization and binding energy measurements give consistent results on the resonance position B_0 and the

---

2 The magnetic field was deliberately chosen to minimize the Dy alone loss to reduce the harmful effect on the interspecies thermalization process.
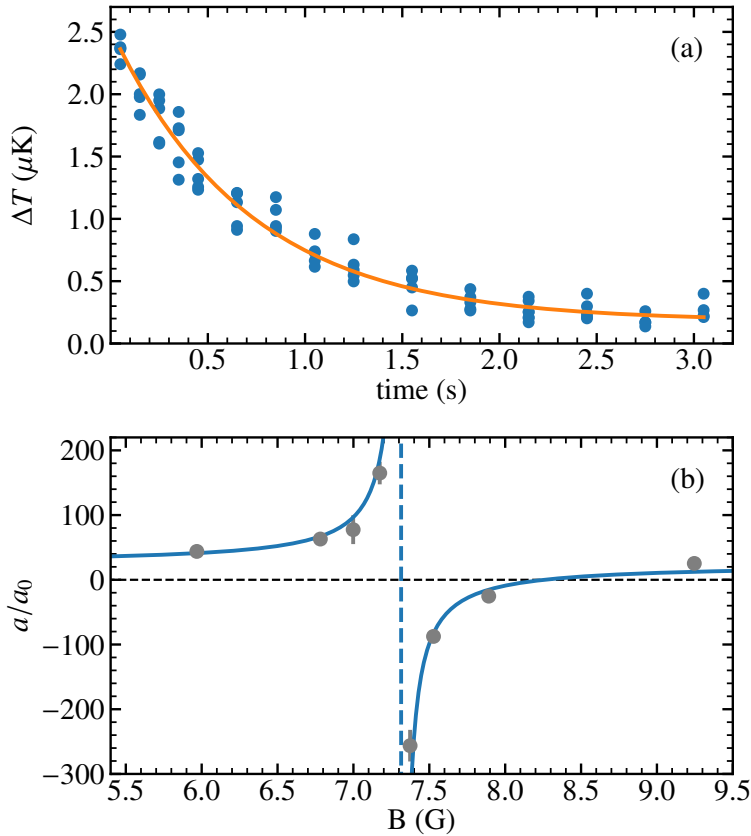
Figure 5.3: Scattering length measurement in the vicinity of the 7.29-G res-
onance. (a) Temperature difference $\Delta T = T_K - T_{Dy}$ versus hold
time in ODT at 5.97 G. The orange solid line shows the numerical
fit curve with the s-wave scattering length $a = 53(9)a_0$. (b) Scat-
tering length between Dy and K versus magnetic field strength.
The gray points represent the values measured by interspecies
thermalization. The solid blue line is a fit based on Eq. (5.1), and
the dashed vertical line indicates the pole position.

resonance strength A. This also supports the validity of our assump-
tion of an isolated Feshbach resonance, where the binding energy
follows Eq. (5.3).

5.4.2   *Light shift*

A differential polarizability between the entrance channel (atom pair
state) and the closed channel (molecular state) in the infrared optical
trap may cause a light-induced shift in the position of a Feshbach
resonance. We have observed such an effect in the ^{6}Li-^{40}K Fermi-Fermi

---

3   The pole position B_0 is fixed to the value obtained from the binding energy measure-
ments.

4   The strength parameter A is fixed to the value obtained from the binding energy
measurements.

Table 5.2: Comparison of fit parameter values related to the 7.29-G Feshbach resonance extracted from different observations (see text).

Method	Section	B_0 (G)	A (G)	R^*/a_0	a_{bg}/a_0
Binding energy	5.3.3	7.295(1)	23.2(9)	643(30)	
Thermalization	5.4.1	7.314(20)	22.8(2.6)		24.2(4.7)
		7.295[3]	23.4(2.4)		22.8(4.5)
Hydrodynamics	5.4.3	7.290(2)	23.2[4]		

mixture [56] and the ^{6}Li-^{41}K Fermi-Bose mixture [44]. Taking this shift into account turned out to be essential for accurate interaction tuning, and also proved to be a very useful tool to implement extremely fast changes of the interaction strength [57]. Here we investigate whether the same effect is present in our Dy-K mixture.

To characterize this effect on the 7.29-G resonance, the Dy-K mixture is prepared in traps of different depths, then the same approach as described in Sec. 5.3.3 is applied to measure the binding energy at different magnetic field strengths. Fig. 5.4(a) shows our results with the solid blue line representing our reference measurement as shown in Fig. 5.2(c). The inset of Fig. 5.4(a) shows a zoom-in of the binding energy near 7.065 G. We observe a small frequency shift of the order of a few kHz between adjacent points. The dashed curves represent the fits to the data points based on Eq. (5.3) with only B_0 as a free parameter, keeping A and $\delta\mu$ fixed to the values of the reference curve. The best fit values for the pole position are shown as blue circles in Fig. 5.4(b). The orange dashed line represents the linear fit $B_0 = \xi U_K + B_{zero}$, which yields the pole position without light shift, $B_{zero} = 7.295(3)$ G, and the linear slope $\xi = 1.6(5) \times 10^{-4}$ G/$^-$K. This value for the slope ξ is about one order of magnitude smaller than typical values observed in Li-K mixtures [44, 56]. Such a small slope implies that the light shift effect is negligible for the shallow traps used in our experiment. It also tells us that the optical trapping potential for Feshbach molecules at 7.29 G can be simply regarded as the sum of the trap depths for free Dy and K atoms with only 3% deviation [5].

5.4.3 *Hydrodynamic expansion*

In Ref. [5], we reported on hydrodynamic expansion as a striking effect of resonant interspecies interaction. On top of the broad 217-G Feshbach resonance, the two components were observed to expand

---

5 The error η can be estimated by the $(\alpha_M/\alpha_a - 1)U_a = \delta\mu\Delta B$, where U_a is the trap depths of atoms, α_M/α_a is the polarizability ratio between molecules and atoms, $\delta\mu$ is the differential magnetic moment between open channel and close channel, such that $\xi = (\alpha_M - \alpha_f)/\delta\mu\alpha_f$ and the polarizability of molecules can be expressed by $\alpha_M = \alpha_f(\xi\delta\mu + 1) \approx 1.027\alpha_f$.
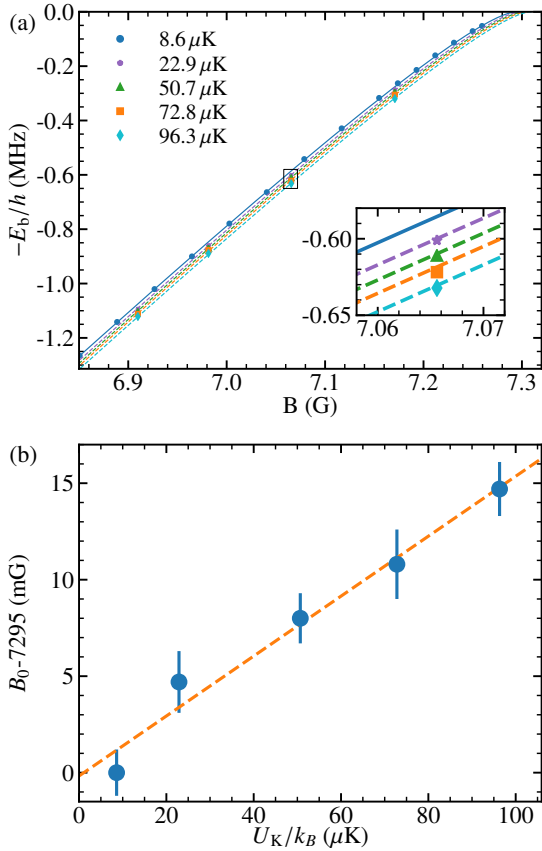
Figure 5.4: Light shift of the Feshbach resonance. (a) Binding energy versus magnetic field for different ODT depths. The symbols represent the measured data, and the solid and dashed lines show the fits based on Eq. (5.3), from which we extract the resonance position B_0. The solid blue curve is the same as shown in Fig. 5.2(c). (b) Resonance position B_0 versus the trap depth for the K atoms. The blue bullets show the fitted results of (a). The orange dashed line represents the linear fit according to $B_0 = \xi U_K + B_{zero}$, with ξ=1.6(5) $\times 10^{-4}$ G/¯K and $B_{zero} = 7.295(3)$ G.

jointly in a collisionally dense cloud after release from the trap. A Monte-Carlo simulation of the resonant collisional dynamics showed excellent agreement with the experimental data. Here we carry out essentially the same experiment, but on the 7.29-G resonance, which is more than 50 times weaker than the 217-G resonance.

The sequence here is similar to the one applied in the experiments described before, but without the decompression stage at the end of evaporation. The mixture is held in a tight ODT with the magic levitation field, where the trap frequencies are $\bar{\omega}_{Dy}/2\pi = 134$ Hz and $\bar{\omega}_K/2\pi = 484$ Hz. To minimize atom loss and heating, the magnetic field is rapidly (in 2 ms) ramped from the evaporation field to 7.42 G and held for 50 ms to ensure a stable field strength. Here, the long lifetime of the Dy-K mixture and relatively large scattering length of $a \approx -200 a_0$ allow Dy and K atoms to reach thermal equilibrium in a

short time without inelastic losses and heating. At this particular field, also Dy losses [6] are found to be very weak. We get $N_{\mathrm{Dy}} = 6.5 \times 10^4$ and $N_{\mathrm{K}} = 2 \times 10^4$ atoms with a temperature of $T = 740\,\mathrm{nK}$, corresponding to $T_{\mathrm{Dy}}/T_F^{\mathrm{Dy}} = 1.6$ and $T_{\mathrm{K}}/T_F^{\mathrm{K}} = 0.6$. These conditions are close to the ones of Ref. [5]. To monitor the hydrodynamic expansion, the magnetic field is ramped to its target value in 2 ms and held for a further 2 ms in the ODT to establish a stable B field. After that, the ODT and the levitation field are switched off simultaneously, and time-of-flight absorption imaging is applied to record the optical depth profile of Dy and K atoms at the target magnetic field.

The resonant interaction regime is realized when the *s*-wave scattering length exceeds all other relevant length scales. These are the inverse wave number of relative motion $1/\bar{k}_{rel} \approx 1700a_0$, the inverse Fermi momentum $1/k_F \approx 1370a_0$, and the range parameter $R^* = 643a_0$. For the present experiments, we obtain a range of $\pm 15\,\mathrm{mG}$, about 50 times narrower than on the broad 217-G resonance explored in previous experiments.

In Figure. 5.5, we demonstrate the observed hydrodynamic behavior in the time-of-flight expansion of the mixture. The upper row shows the optical depths of Dy atoms and K atoms at 7.701 G with the estimated scattering length $a \approx -38a_0$. Here, we do not observe any significant effect of interaction between the two species. The lighter potassium atoms expand faster than the heavier dysprosium atoms, leading to a size ratio of $\sigma_{\mathrm{K}}/\sigma_{\mathrm{Dy}} = \sqrt{m_{\mathrm{Dy}}/m_{\mathrm{K}}} \approx 2$, where the σ_{K} and σ_{Dy} are defined as a standard deviation of the spatial distribution. The lower row in Fig. 5.5 shows the expansion on resonance, where the strong interspecies collision rate leads to collective behavior. The size of the K cloud becomes much smaller than at 7.701 G and its peak density is greatly enhanced. On the contrary, the size of the Dy cloud is slightly larger than at 7.701 G with a decreased peak density. For both species, the clouds have a similar size on resonance because of the collective expansion effect, and a few K atoms can be observed outside the overlap region of Dy and K cloud. The latter are the atoms that expand freely after having escaped from the hydrodynamic core [5].

To quantitatively analyze the hydrodynamic expansion [5], we explore the central fraction defined as the fraction of K atoms inside a circle with radius $\sqrt{2}\sigma_{\mathrm{Dy}}$. The orange dots in Fig. 5.6 show the experimental central fraction as a function of scattering length, which we calculated from Eq. (5.1) with a fixed $A = 23.2\,\mathrm{G}$ (see Table 5.1). Far away from the resonance (at 7.701 G), we get a central fraction of 0.22 (out of the range of Fig. 5.6) corresponding to the expansion of two non-interacting Gaussian clouds. The central fraction gradually increases to 0.45 as the scattering length increases. The width at half maximum of experimental data is about $|1000a_0/a| = 0.68$ from Lorentzian curve fit, which is consistent with our length scale estimated range of $B - B_0 \approx \pm 15\,\mathrm{mG}$.
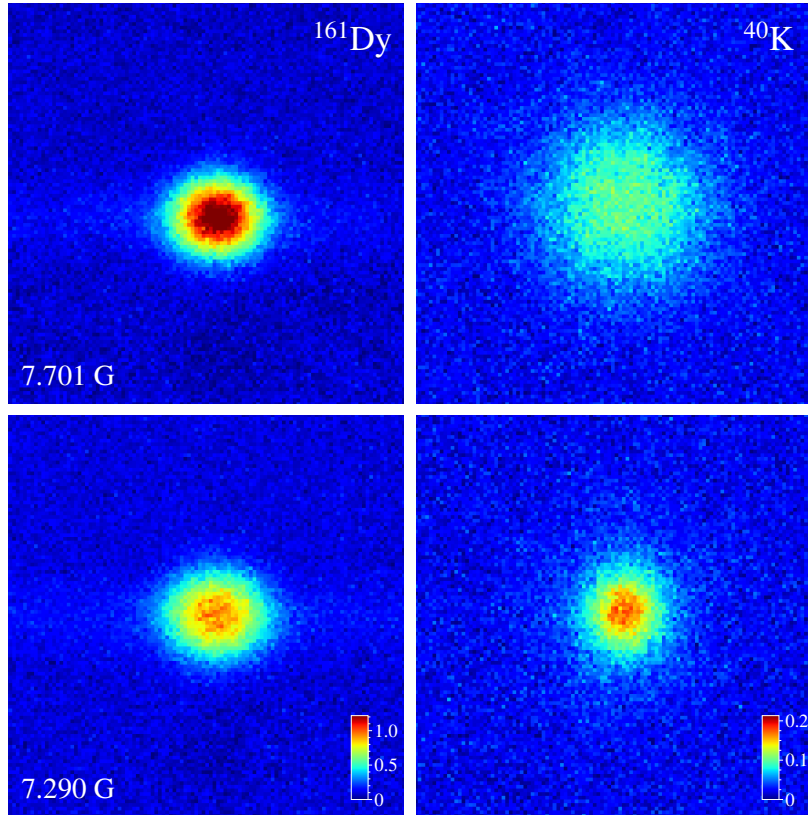
Figure 5.5: Absorption images of Dy and K far away from (upper row) and on (lower row) the 7.29-G Feshbach resonance after 4.5 ms of free expansion. The optical depth of K is significantly enhanced on resonance, while Dy decreases because of the collective expansion. The field of view of all images is 360 µm×360 µm. Each image is an average of five individual shots.

We also perform the same Monte-Carlo simulation as we did for the 217-G resonance [5] to extract the central fraction. We take into account the momentum dependence of the resonant collisional cross section, but neglect the small effect of R^*. The gray open circles in Fig. 5.6 show our simulation results as a function of the inverse scattering length. We find that the matching between simulation and experiment is very sensitive to the exact value of the pole position B_0. Therefore hydrodynamic expansion allows us to determine the best value of $B_0 =$ 7.290 G with an uncertainty of 2 mG, which is dominated by magnetic field fluctuations in our system.

As shown in Fig. 5.6, the experiment matches well with the simulation in most regions apart from a narrow central part. The good match confirms our value for the strength parameter A obtained from the binding energy and the thermalization measurements (see Table 5.2). The value of the pole position here is slightly below the value derived from the binding energy measurements, which we attribute to a systematic error in the binding energy measurements caused by
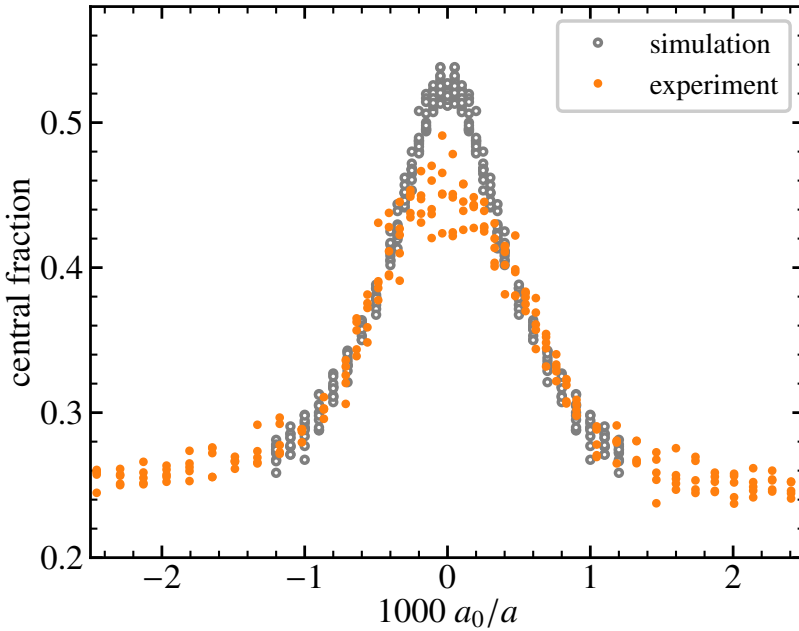
Figure 5.6: Comparison of the central fraction as a function of scattering length obtained from Monte-Carlo simulations (gray open circles) and experiment (orange solid circles). The central fraction is defined as the fraction of K atoms inside $\sqrt{2}\sigma_{\mathrm{D}y}$ region.

neglecting the small, but finite collision energies in the mixture. This indeed leads to a small overestimation of the binding energies and the fit produces a pole position, which is a few mG too high. Therefore, for the further discussion, we choose $B_0 = 7.290(2)\,\mathrm{G}$ as the presumably more accurate pole position.

We notice that the observed central fraction is smaller than the one from the simulation in the resonance range with $|a| \gtrsim 3000a_0$, while we did not observe such a deviation in our previous experiments near the broad 217-G resonance [5]. We suspect that uncontrolled magnetic field fluctuations of the order of a few mG may have been caused by turning off the levitation gradient when the mixture is released from the trap, which may have reduced the effect of interactions very close to resonance during the free expansion. Obviously, the 7.29-G resonance is much more sensitive to magnetic field fluctuations than the broad 217-G resonance. Apart from this rather technical issue, we observe essentially the same behavior of the hydrodynamic expansion for both resonances.

We finally note that the expanding clouds in Fig. 5.5 show small anisotropies, which may be related to hydrodynamic behavior and/or the dipole-dipole interacting in the strongly magnetic Dy component. The origin of this effect requires further investigations using more anisotropic trapping schemes than applied in the present work and will be subject of future work.

5.4.4 *Lifetime and three-body decay*

Collisional stability is an important ingredient for deep evaporative cooling of the Dy-K mixture and for future experiments on mass-imbalanced fermionic superfluids [22, 24, 25]. In Ref. [5], we have reported long lifetimes of the mixture near the 217-G resonance, which we attributed to Pauli suppression of inelastic few-body processes [38, 39]. Here we study whether we can achieve also comparably long lifetimes near the 7.29-G resonance.

To initiate the measurement, the sample is prepared in a shallow ODT with a mean trap frequency of $\bar{\omega}_{Dy} = 2\pi \times 35$ Hz and $\bar{\omega}_K = 2\pi \times 128$ Hz, where the initial temperature and atom number of the sample varies slightly for different measurements (see Figs. 5.7 and 5.8). The magnetic field is ramped to the target value and the atom numbers are recorded by absorption imaging after holding the mixture in the trap for a few 100 ms.

In Fig. 5.7(a), we present the loss spectrum for the mixture in a 50-mG wide range, showing both the number of remaining Dy and K atoms. For comparison, in Fig. 5.7(b), we show the corresponding spectrum for a pure Dy sample, which is expected to show three-body loss features because of the generally very dense spectrum of resonances in fermionic Dy [6, 41]. The gray dashed line indicates the pole position of the resonance as obtained from the hydrodynamic expansion measurement presented in the preceding section. Figure 5.7(a) shows a striking "valley" for both species, located on the lower side of the resonance. This is about 10 mG below the pole position, where we estimate a large positive value of the scattering length of $a \approx +2300a_0$. The loss feature appears in both Dy and K and is stronger in Dy by about a factor of two. A similar feature was observed for the 217-G resonance [5], which also resembles observations made in experiments on resonantly interacting spin mixtures of fermions [58–60]. We interpret this loss as being due to the formation of weakly bound dimers by three-body recombination and subsequent inelastic atom-dimer collisions. The fact that maximum losses are observed in the regime of weakly bound dimers and not on top of the resonance (as usually observed in bosonic systems) points to the presence of Pauli suppression on resonance.

Regarding Dy intraspecies losses, Fig. 5.7(b) shows a wide plateau of negligible intraspecies losses along with a narrow resonant loss feature on the upper side of the resonance. We find that, for the Feshbach resonance in the Dy-K mixture, the pole position and the range of weakly bound universal dimers are located within the low-loss plateau, which is a lucky coincidence and very favorable for future experiments on the resonantly interacting mixture.

Figure 5.8(a) shows the decay of the trapped mixture at 7.290 G, i.e. at the very center of the resonance. The initial atom numbers
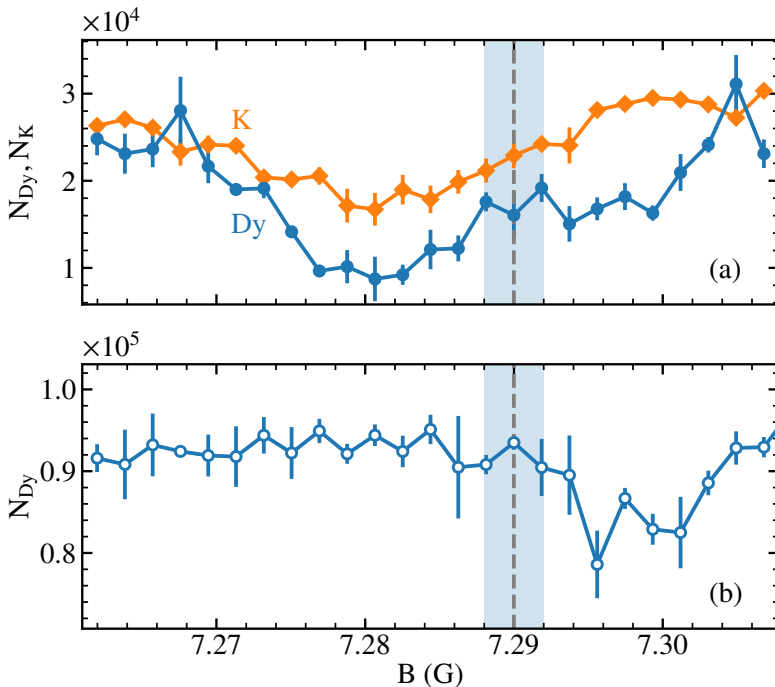
Figure 5.7: Loss scans in the vicinity of the 7.29-G resonance. (a) Atom number loss spectra of the two components of the mixture for a hold time of 140 ms in the ODT. The initial atom numbers are $N_{Dy} = 3.4 \times 10^4$ and $N_K = 3.3 \times 10^4$ with a temperature of $T = 170$ nK. A pronounced interspecies loss feature appear about 10 mG below resonance, where the s-wave scattering length is very large and positive. (b) Number of atoms in a pure Dy cloud in the same trap after a hold time of 220 ms, with an initial atom number of $N_{Dy} \approx 9.5 \times 10^4$ and a temperature of $T = 140$ nK. The gray dashed line indicates the pole position of the Feshbach resonance according to the hydrodynamic expansion measurements in Sec. 5.4.3. The shaded region indicates the uncertainty. Without K, significant losses of Dy only show up 5-10 mG above the resonance, while a 30-mG wide region below resonance appears to be essentially free of Dy loss features.

are $N_{Dy} = 3.4 \times 10^4$ and $N_K = 2.2 \times 10^4$ with an initial temperature $T = 115$ nK. We analyze the loss curve based on the assumption that three-body processes dominate the loss. Quantitatively, we extract the initial slope from a heuristic fit model as described in previous work [5, 6], which then allows us to derive a value for the three-body event rate coefficient. The solid curves in Figs. 5.8(a) and (b) represent the fitted curves. For the lifetime of the mixture, we obtain $\tau_{DyK} = 360$ ms,

which is much shorter than the one of Dy alone ($\tau_{Dy} \approx 5\,\text{s}$)[6]. Obviously, interspecies processes are the main cause of losses on resonance.
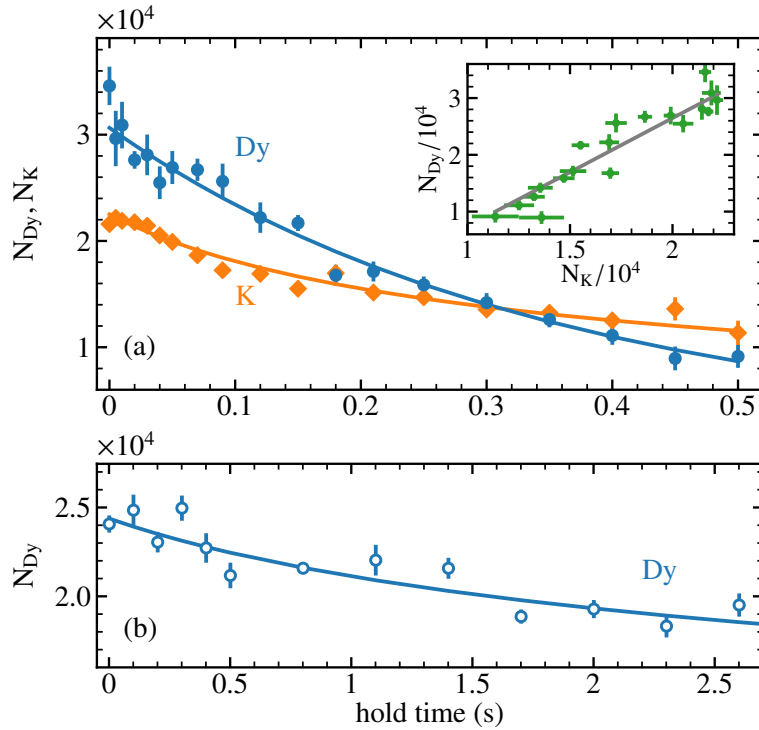
Figure 5.8: Comparison of atom number decay between (a) the Dy-K mixture and (b) a pure sample of Dy in the ODT at the pole position. The temperature of the mixture is $115\,\text{nK}$ and of the pure Dy cloud is $49\,\text{nK}$. The solid lines represent fits with the initial lifetime of $\tau_{DyK} = 360\,\text{ms}$ for the mixture and $\tau_{Dy} \approx 5\,\text{s}$ for Dy alone. The inset in (a) shows the relationship between the Dy and K atom numbers during the decay. The solid line represents a linear fit with $N_{Dy} = aN_K + b$, yielding $a = 1.9(2)$ and $b = -5.8(1.6) \times 10^3$.

To identify the dominant loss process, we plot in the inset of Fig. 5.8(a) the number of Dy atoms versus the number of K atoms during the decay. A linear fit yields a slope of $dN_{Dy}/dN_K = 1.9(2)$, which suggests a three-body process involving two heavy and one light atom as the dominant one. This may be interpreted as a consequence of the effective three-body attraction in a resonant heavy-heavy-light fermion system [56, 61]. Neglecting other processes, the loss of atoms in the mixture can be modeled by the loss-rate equation

$$\frac{dN_{Dy}}{dt} = 2\frac{dN_K}{dt} = -2K_3 \int n_{Dy}^2 n_K d^3r, \tag{5.4}$$

---

6 Attributing the observed decay of the pure Dy sample to three-body collisions would yield a rather large value of $K_{3,Dy} \approx 2 \times 10^{-26}\,\text{cm}^6/\text{s}$ for the event rate coefficient. Comparison with our previous work [6] shows that this is unrealistically large if resonances avoided. We therefore believe that another process (such as residual evaporation) is the dominant source of losses.

where n_{Dy} and n_K are the position-dependent atomic number densities of Dy and K atoms, respectively. The event rate coefficient K_3 quantifies Dy-Dy-K three-body losses. Under our conditions, background losses are negligible.

To obtain an approximate value for the event rate coefficient K_3, we assume that the atomic number densities follow thermal Gaussian distributions. For Dy with $T/T_F^{Dy} = 1.2$, the distribution is essentially thermal. The K component with $T/T_F^K \approx 0.3$ is degenerate, so that Fermi pressure increases the cloud size. However, because of the tighter optical confinement of K, this has only little effect on the overlap integral in Eq. (5.4). We also neglect any interaction effect on the spatial distributions. Under these assumptions, Eq. (5.4) leads to [5]

$$\frac{\dot{N}_K}{N_K} = -K_3 N_{Dy}^2 \left(\frac{\sigma}{2\pi\sigma_{Dy}^2 \sigma_K} \right)^3, \tag{5.5}$$

where $\sigma = (2\sigma_{Dy}^{-2} + \sigma_K^{-2})^{-1/2}$ and $\sigma_i = \omega_i^{-1}\sqrt{k_B T/m_i}$ ($i =$Dy, K). We finally obtain a value of $K_3 = 1.8(7) \times 10^{-24}\,\mathrm{cm}^6/\mathrm{s}$ for the three-body event rate coefficient on resonance.

We can compare the resulting K_3-value with measurements near the 217-G resonance in Dy-K mixture, related work on resonant Fermi-Bose mixtures of K-Rb and Li-K [44, 62], and Bose-Bose mixtures of K and Rb [63]. This indicates a Pauli suppression of inelastic few-body losses by roughly one order of magnitude, but not much more. In this respect, the 7.29-G resonance seems to be less favorable than the 217-G resonance. Nevertheless, with the very shallow ODT applied, we could demonstrate lifetimes of a few 100 ms, which gives enough time to carry out experiments in the resonant regime.

5.4.5 *Creation of Feshbach molecules*

An important application of Feshbach resonances is the association of weakly bound dimers by magnetic field ramps [17]. A common way to detect such Feshbach molecules is Stern-Gerlach separation [64, 65], facilitated by the different magnetic moment to mass ratio of dimers and free atoms. We here apply this technique to demonstrate the formation of weakly bound DyK molecules.

The starting point of these experiments is a degenerate mixture of $N_{Dy} = 6.4 \times 10^4$ and $N_K = 2.9 \times 10^4$ atoms in an ODT with $\bar{\omega}_{Dy} = 2\pi \times 40.3\,\mathrm{Hz}$ and $\bar{\omega}_K = 2\pi \times 146\,\mathrm{Hz}$. The temperature of $T = 125\,\mathrm{nK}$ corresponds to $T/T_F^{Dy} = 0.9$ and $T/T_F^K = 0.33$. The magic levitation gradient of 2.69 G/cm is applied to eliminate the differential gravitational sag, see Sec. 5.3.1. The magnetic field is then ramped up to 7.62 G, which is about 330 mG above the resonance center. This particular field has been chosen to exploit a minimum of loss and heating related to Dy intraspecies processes. The ramp to this preparation

field takes only 2 ms, but additional 20 ms are given for the magnetic field to settle to a stable value.

The Feshbach molecules are created by sweeping the magnetic field to 7.11 G within 2 ms, i.e. at a rate of $\dot{B} = -0.25$ G/ms. At the end of the sweep, the ODT is switched off and the magnetic field gradient is raised to 7.5 G/cm in 0.5 ms. For the Dy atoms, this increased gradient results in a total, upward-directed acceleration of 1.65g (2.65g from the magnetic gradient and -g from the field of gravity). For the DyK dimer (molecular magnetic moment of about 8.9μ_B), the acceleration amounts to 0.89g. The K cloud is nearly levitated with a small acceleration of only 0.07g. During a time of flight of 5 ms, the DyK dimers are efficiently separated from free Dy and free K atoms, which puts the molecular cloud between the two atomic clouds. Finally, for detection, molecules are dissociated to free atoms by ramping back the magnetic field to 7.62 G in 1 ms, and absorption images are taken for Dy (K) atoms after further 2 ms (1 ms).

In Fig. 5.9, we present the resulting absorption images of Dy atoms (a) and K atoms (b). The free Dy and K atomic clouds are at the top and bottom of the images, respectively. The smaller clouds located closer to the center of the images result from the dissociation of Feshbach molecules. Note that the Dy and K clouds resulting from the dissociating dimers are not exactly at the same vertical position. This is due to the different acceleration in the short time between dissociation and imaging. More than $N_{mol} = 7.5 \times 10^3$ molecules were created with a transfer efficiency of of $N_{mol}/N_{K,0} \approx 20\%$, where $N_{K,0}$ is the K atom number right before the association ramp.

The small size of the expanding molecular cloud, as clearly seen in the images in comparison with the atomic clouds, points to a rather low temperature. From the temperature in expansion and the trap potential, we can infer a phase-space density of about 0.1 for the trapped molecular cloud [66]. With further optimization, this preliminary observation is very promising for reaching the quantum-degenerate regime, i.e. Bose-Einstein condensation of these molecules. Experiments pursuing this goal are underway in our laboratory.

5.5 SUMMARY AND CONCLUSION

In the Fermi-Fermi mixture of ^{161}Dy and ^{40}K, prepared in the lowest spin states, we have identified in total five Feshbach resonances in the magnetic-field region below 10 G. We have characterized these resonances by observing the enhanced interspecies thermalization and by measuring binding energies of the molecular states underlying the resonances. We have extracted the main resonance parameters: position, strength, and magnetic moment of the molecular state. The five resonances can all be classified as narrow (closed-channel dominated) resonances [17], but for some of them the universal range,
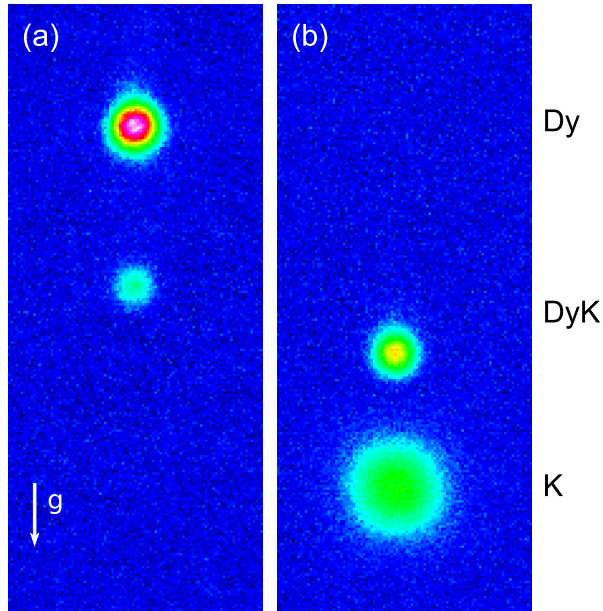
Figure 5.9: Stern-Gerlach analysis of the Dy-K mixture after association of dimers by a Feshbach ramp and dissociation by an inverse ramp. Absorption images of (a) Dy and (b) K are taken at the magnetic field of 7.62 G with a gradient of 7.5 G/cm. The images in (a) and (b) are finally taken after a further 2 ms and 1 ms, after completion of the dissociation ramp. The arrow shows the direction of gravity. The field of view of all images is 329 ̄m×785 ̄m.

where the physics of broad resonances is recovered, is wide enough to be conveniently addressable in experiments.

As a case of particular interest, we have investigated the resonance at 7.29 G in more detail and demonstrated several applications. This resonance is well separated from other ones and can thus be modeled within a basic two-channel approach [43]. We have extracted the resonance strength in three different ways: Measured binding energies and elastic scattering in thermalization and in hydrodynamic expansion yielded consistent results, which confirms our good understanding of the resonance.

We have also studied the decay properties of the Dy-K mixture near the 7.29-G resonance and found a qualitative behavior very similar to our previous work [5] near the broad 217-G resonance in the same system. A loss maximum is found in the universal range on the lower side of the resonance, where the scattering length is large and positive and weakly bound molecules are produced by three-body recombination. Such a behavior is typical for fermionic mixtures with loss suppression on resonance. Our measurement of three-body decay on top of the resonance reveals a relatively large decay rate in comparison with the 217-G resonance, which is in accordance with the general trend that broader resonances are more favorable for fermionic loss suppression.

Our experiments show that, employing the 7.29-G resonance, one can do essentially everything that has been done for the broad 217-G resonance. The low field offers major practical advantages in simplicity, speed, and accuracy of magnetic field control. Another very important advantage consists in the fact that the interspecies resonance region is not contaminated by the many intraspecies Dy resonances. A price one has to pay for these advantages seems to be a weaker suppression of inelastic decay, but our experiments have shown that, in a very shallow optical trap, lifetimes of a few hundred milliseconds can be achieved for the resonant mixture, which is enough for many experimental applications.

We have also presented a proof-of-principle demonstration of the creation of Feshbach molecules by sweeping across the resonance, which indicates a high efficiency of the process. Our near-future work will be dedicated to identifying the optimum conditions for molecule creation, the investigation of collisional processes involving the molecules, and to reaching the necessary phase-space densities for molecular Bose-Einstein condensation. This will be an important step towards our general goal to realize novel superfluid states in fermionic mixtures of ultracold atoms.

We finally note that the spectrum of interspecies Feshbach resonances in mixtures of submerged-shell lanthanide atoms with alkali atoms can be expected to be non-chaotic [52], in contrast to intraspecies resonances in experiments with Dy and Er [48]. Therefore, we are confident that, with input from our experiments, a scattering model can be developed that fully describes the resonance scenario and allows experimentalists to identify the best suited resonances for specific purposes.

5.6   APPENDIX A: PREPARATION

The sources of Dy and K, the magneto-optical traps for the two species, the gray-molasses cooling stage for K, and the sequential dipole trap loading scheme have been described already in Ref. [2]. Here we discuss a more refined sequence of optical dipole trapping (Sec. 5.6.1), which also facilitates in-trap narrow-line Doppler cooling (Sec. 5.6.2). With these improvements and some further optimizations, we find that the atom numbers in the deeply degenerate regime of the mixture can be increased by typically a factor of five.

5.6.1   *Optical dipole trapping schemes*

Our preparation sequence relies on four stages of optical dipole trapping. We employ in total four infrared laser beams in the configuration illustrated in Fig. 5.10 (top); the beam parameters are listed in Table 5.3. The timing scheme in Fig. 5.10 (bottom) shows which combination of

crossing beams is employed to realize the optical dipole traps in the four different stages.

Table 5.3: Trapping beam properties. Waist w and maximum power $P_{\mathrm{m}ax}$ for each of the four beams. The two RDT (CDT) beams are derived from an Azurlight ALS-IR-1064-5-I-CC-SF (Mephisto MOPA 18 NE) and frequency offset by 160 MHz (220 MHz) by acousto-optical modulation.

Parameter	RDT1	RDT2	CDT1	CDT2
w (μm)	94	93	24	62
$P_{\mathrm{m}ax}$ (W)	12	11	0.4	0.73

In the first stage, a large-volume reservoir dipole trap (RDT) facilitates efficient loading of both species from magneto-optical traps. This dipole trap is realized with two high-power infrared beams (labeled RDT1 and RDT2), crossing in the horizontal plane at an angle of 18°. In a later stage, in which evaporative cooling is performed, we use a crossed-beam dipole trap (CDT) realized with two tightly focused beams. The beam CDT1 propagates horizontally in opposite direction to RDT1, and CDT2 is directed vertically. These two dipole traps (RDT and CDT) for loading and evaporative cooling have been introduced in our previous work [2]. For the present work, we have introduced two upgrades:

(1) Between the RDT and the CDT stage, we have implemented an additional stage for narrow-line Doppler cooling of Dy. For this purpose, an elongated trap is realized with beams RDT1 and CDT1.

(2) After the CDT stage, the evaporatively cooled mixture is transferred into a shallow dipole trap formed by beams RDT2 and CDT2. This decompresses the sample, facilitates transfer to high magnetic fields with minimized collisional losses, and is used for most of the experiments reported here.

5.6.2 *In-trap narrow-line laser cooling of Dy*

Laser cooling on the narrow 741-nm line of Dy [13] is carried out as an intermediate step before evaporative cooling. The line is an inner-shell transition ($4f \rightarrow 5d$) with a narrow linewidth of 1.8 kHz. The Doppler temperature of 43 nK is an order of magnitude lower than the recoil temperature of 213 nK, which makes it very interesting for deep laser cooling.

We generate the 741-nm light with an external-cavity diode laser (Moglabs ECDL) locked to a high-finesse cavity. The narrowing of the laser linewidth is achieved by a fast feedback loop acting directly on the diode current (Toptica mFALC 110). We combine the 741-nm cooling light with the 626-nm beams of the magneto-optical trap, using
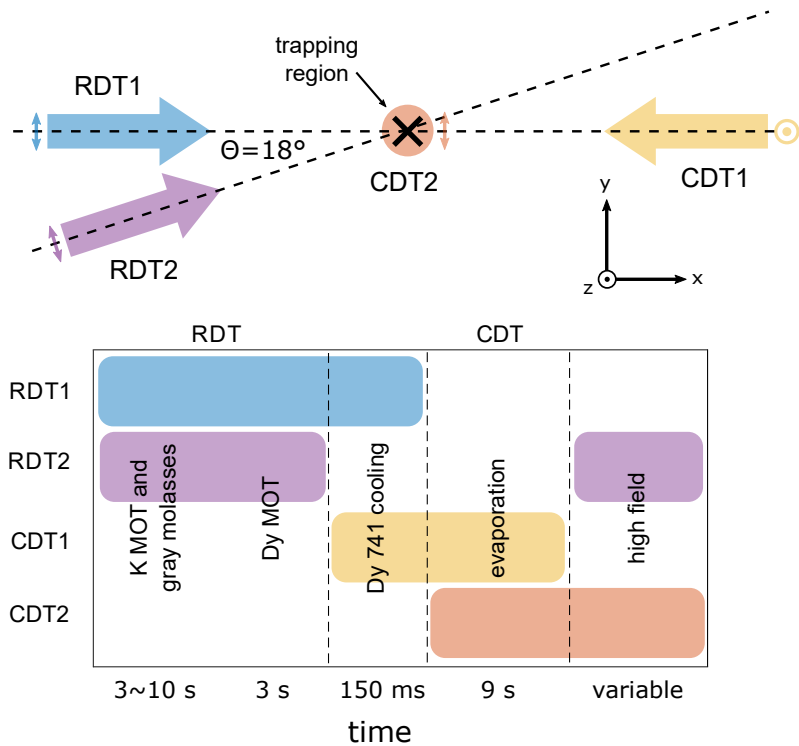
Figure 5.10: Laser beam configuration for optical dipole trapping (top), and timing sequence (bottom) of the different combinations in the four trapping stages. While the large-volume reservoir dipole trap (RDT) is applied for loading, the tightly confining crossed dipole trap (CDT) is used for evaporative cooling. In an intermediate stage between RDT and CDT, in-trap narrow-line cooling is applied to Dy. In the last stage, the sample is decompressed and transferred to the desired target magnetic field, at which the specific experiments are carried out.

the same polarizations. A magnetic bias field of $230 \, \text{mG}$ defines the quantization axis. The saturation intensity of the transition is as low as $0.57 \, \mu\text{W}/\text{cm}^2$.

Doppler cooling is carried out in an elongated trap, into which the atoms are transferred from the RDT by adiabatically ramping the power of beam RDT2 down and simultaneously ramping CDT1 up to a power of $300 \, \text{mW}$. The beam RDT1 remains unchanged at a power of $10 \, \text{W}$. The resulting elongated trap geometry with a low atomic density is important to minimize the detrimental effect of reabsorption of scattered photons. After transfer, narrow-line cooling starts with 2.6×10^6 Dy atoms at a temperature of $\sim 9 \, \mu\text{K}$.

In-trap Doppler cooling is carried out in two steps: First, the beam intensity is set to about $6 \, \mu\text{W}/\text{cm}^2$. A red laser detuning of $969 \, \text{kHz}$ is chosen with respect to the free-space resonance frequency at zero magnetic field, which is larger than light shift introduced by the trap and the Zeeman shift. Figure 5.11 shows the evolution of temperature
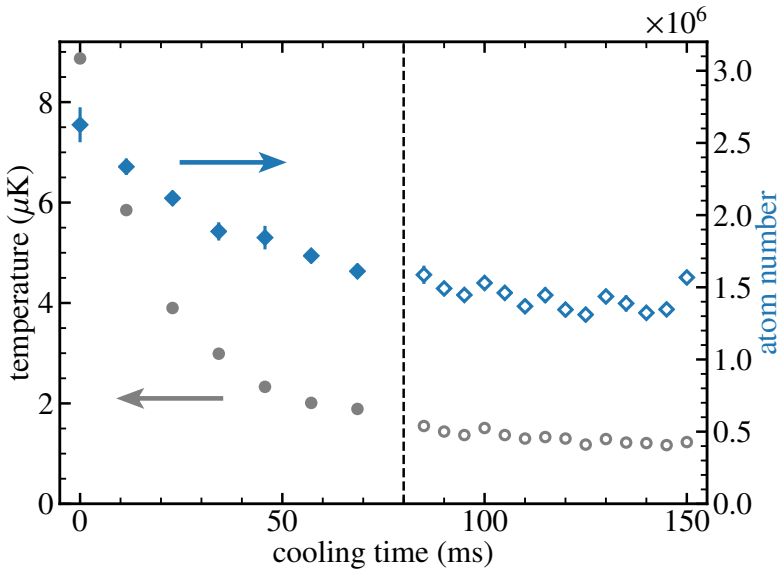
Figure 5.11: Laser cooling using the narrow 741-nm line. The evolution of temperature and atom number is shown within the 150-ms duration of the cooling process. After 80 ms (vertical dashed line), the laser parameters are changed to optimize the cooling process (see text).

and atom number during the Doppler cooling process. Within 80 ms (vertical dashed line), the Dy temperature is reduced to 1.7 μK, while the number of trapped atoms decreases by roughly a factor of two. We attribute the latter to plain evaporation along the weak axis of the trap. In a second step, we reduce the trap power (RDT1 beam reduced to 1.7 W within 10 ms), and we simultaneously decrease the cooling laser detuning and intensity to 532 kHz and 3 μW/cm^2. Doppler cooling is then continued for 60 ms, and we finally reach a temperature of 1.2 μK for 1.6×10^6 Dy atoms. We found this second Doppler cooling step crucial to accumulate the atoms in the center of the trapping region with maximum overlap with the CDT then used for evaporative cooling.

In a mixture of Dy and K, the K component is not affected by the Dy cooling light and the cooling performance of Dy is not compromised by the presence of K atoms.

5.7   APPENDIX B: MAGNETIC FIELD CALIBRATION

We calibrate the magnetic field by RF spectroscopy on K. As an example, we here discuss the calibration in the range of interest for the binding energy measurements near the 7.29-G Feshbach resonance. The preparation sequence is the same as described in Sec. 5.3.3. After the ramp to the target field, we blow away all Dy atoms with 421-nm resonant light, leaving only K atoms in the ODT, which populate
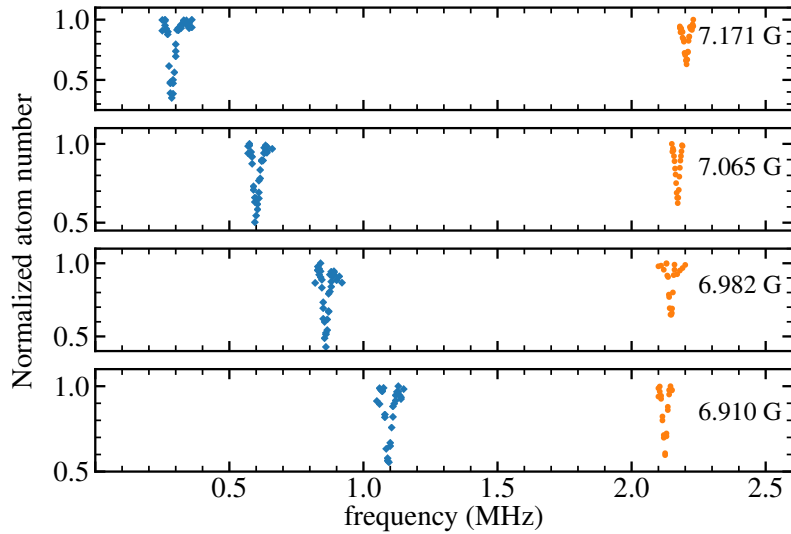
Figure 5.12: Magnetic field calibration for the binding energy measurements near the 7.29-G resonance. The blue diamond show the signal from molecular association in the Dy-K mixture, and the orange circle show the atomic RF spectroscopic signal in the absence of Dy. The atom number is normalized by the initial values of $N_K = 3 \times 10^4$.

the lowest hyperfine state $K|1\rangle$ ($|F = 9/2, m_F = -9/2\rangle$). We apply a short RF-pulse (100 μs) to transfer atoms to the second-to-lowest state $K|2\rangle$ ($|F = 9/2, m_F = -7/2\rangle$). Imaging near 7 G cannot distinguish between the $K|1\rangle$ and the $K|2\rangle$ state, since the Zeeman splitting at 7 G is much smaller than the linewidth of the transition. To overcome this problem, we ramp up the field strength to a high value (168 G, limited by the power supply used), where the imaging frequency difference of 28.9 MHz for imaging $K|1\rangle$ and $K|2\rangle$ is large enough to detect each spin state independently. Time-of-flight imaging is finally applied to record the number of atoms in the state $K|1\rangle$ and $K|2\rangle$.

Figure 5.12 shows the RF spectroscopic signal on the atomic transition in comparison with the molecular binding energy measurements by magnetic-field wiggle spectroscopy as discussed in Sec. 5.3.3. The signals are compared for four different magnetic field strengths below the 7.29-G resonance. Obviously, the atomic transition (with a differential magnetic moment corresponding to 0.44μ_B) shifts much less than the molecule association signal (shift corresponding to about $-2.2\mu_B$). The magnetic field can be extracted accurately from the atomic signal based on the Breit-Rabi formula. Here, the field uncertainty comes from a fit of a Lorentzian to the signal and typically amounts to about 1.5 mG.

The calibration of the magnetic field versus current is done in the following way: We first calibrate the magnetic field for different currents, then we extract the dependence of the magnetic field on

the current from a linear fit, and finally, the field strengths for other currents are calculated from this linear fit.

We also investigated the magnetic field stability in our setup, again using RF spectroscopy on the K$|1\rangle$ - K$|2\rangle$ transition. The coil setup used for fields up to $1.6\,$G possesses a current stability that corresponds to a field stability (the root mean square value of noise) as low as $0.2\,$mG. With the different pair of coils and power supply used to generate higher fields (up to $370\,$G), the corresponding stability is $2\,$mG. In addition to that, we identify ambient magnetic field noise (mostly $50\,$Hz) with a stability of $1.2\,$mG.

PUBLICATION: DIPOLE-MODE SPECTRUM AND HYDRODYNAMIC CROSSOVER IN A RESONANTLY INTERACTING TWO-SPECIES FERMION MIXTURE

Zhu-Xiong Ye, Alberto Canali, Chun-Kit Wong, Marian Kreyer, Emil Kirilov, and Rudolf Grimm.

Author contribution: The author took a supporting role in the process of acquiring and analyzing the data described in this publication as well as writing the manuscript.

Ultracold quantum-gas mixtures of fermionic atoms with resonant control of interactions offer a unique test-bed to explore few- and many-body quantum states with unconventional properties. The emergence of such strongly correlated systems, as for instance symmetry-broken superfluids, is usually accompanied by hydrodynamic collective behavior. Thus, experimental progress in this field naturally requires a deep understanding of hydrodynamic regimes. Here, we report on experiments employing a tunable Fermi-Fermi mixture of ^{161}Dy and ^{40}K near quantum degeneracy. We investigate the full spectrum of dipole modes across a Feshbach resonance and characterize the crossover from collisionless to deep hydrodynamic behavior in measurements of frequencies and damping rates. We compare our results with a theoretical model that considers the motion of the mass centers of the two species and we identify the contributions of friction and mean-field interaction. We show that one oscillating mode exists over the whole range of interactions, exhibiting striking changes of frequency and damping in the deep hydrodynamic regime. We observe the second oscillating mode to split into two purely exponential damping modes. One of these exponential modes shows very fast damping, faster than any other relevant timescale, and is largely insensitive against experimental imperfections. It provides an accurate measure for the interspecies drag effect, which generalizes the concept of spin drag explored in other experiments. We finally characterize the interspecies drag in terms of a microscopic friction coefficient and we discuss its unitarity-limited universal behavior on top of the resonance.

6.1 INTRODUCTION

More than two decades of research on ultracold fermionic quantum gases have yielded a wealth of exciting insights into quantum matter featuring strong interactions [18–20, 67, 68]. Two-component mixtures are commonly used in the experiments to enable *s*-wave interaction, which facilitates efficient cooling and allows to implement strong tunable interactions near Feshbach resonances [17]. While spin mixtures of fermionic atoms of the same species are routinely employed in many present experiments, mixtures composed of different fermionic species are much less established, presumably owing to their complex interaction properties and additional challenges in the preparation process. However, fermionic species mixtures hold great promise for future experiments, enabling the exploration of novel phenomena through the introduction of mass imbalance as an additional degree of freedom.

Systems of fermions with constituents of different masses are at the heart of new phenomena in the few-body sector [56, 69–77], regarding the physics of quantum impurities [74, 78, 79], and in relation to unconventional pairing mechanisms [22–25, 80–86] and the emergence of novel superfluids [21, 87]. A particular example and motivation for our work on two-species fermion mixtures is the prospect to observe the elusive Fulde-Ferrell-Larkin-Ovchinnikov (FFLO) state [26–28], which in the case of mass imbalance can be expected [22–25, 86] under realistically attainable experimental conditions.

The main requirements for experiments towards novel few- or many-body quantum states in fermionic mixtures include efficient cooling into the quantum-degenerate regime, the existence of sufficiently broad Feshbach resonance for interaction tuning, and collisional stability of the mixture in the resonance regime. To our best knowledge, five different two-species fermion mixtures have been realized so far: ^{6}Li-^{40}K [29–32, 88], ^{161}Dy-^{40}K [2, 5, 12, 89], ^{6}Li-^{53}Cr [35–37, 90], ^{6}Li-^{167}Er [91] and ^{6}Li-^{173}Yb [33, 34]. Among these mixtures the Dy-K system features a unique combination of favorable properties. It is rather straightforward to cool the mixture deep into the doubly degenerate regime, following standard procedures of laser cooling and trapping and subsequent evaporative cooling [2]. The mixture features an ample spectrum of interspecies Feshbach resonances in the lowest spin channel, which is immune against two-body losses. The observed resonances include a broad one centered at a magnetic field of 217 G [5] and a bunch of low-field Feshbach resonances [12] below 10 G. As a particularly interesting candidate for interaction tuning and molecule formation we have identified a resonance near 7.3 G [12, 89]. This isolated resonance lies in a magnetic-field region not contaminated by ultra-narrow interspecies and intraspecies [6] resonances and it facilitates fast interaction control by relatively small, but not too small changes of the magnetic fields. For resonant atomic Dy-K mixtures, we have observed long lifetimes close to one second and measured low three-body rate coefficients, indicating a substantial suppression of recombination losses [1].

Strongly interacting Fermi gases exhibit hydrodynamic behavior [18, 92]. Related phenomena have been observed in many experiments on spin mixtures, mainly studying the expansion dynamics [92, 93] and collective modes [94–99]. The dependence of such phenomena on the interaction strength and temperature provides information on the properties of the system and elucidates the basic mechanisms leading to hydrodynamics. In fermionic species mixtures, only few observations of hydrodynamic behavior have been reported so far.

---

[1] Although the interaction properties in the Dy-K mixture sound almost ideal, it should be mentioned that the extremely dense spectrum of intraspecies ^{161}Dy resonances [6, 41] causes problems when the magnetic field is to be ramped from the preparation field to the resonance of interest for the experiments and thus requires carefully optimized ramping protocols.

The anisotropic expansion of a ^{6}Li-^{40}K mixture after release from the trap [88] was demonstrated as an effect already well known from spin mixtures [93]. An interesting class of phenomena, distinct from those seen in spin mixtures, emerges when species with markedly different properties are hydrodynamically coupled, leading to a composite fluid with novel characteristics. Manifestations of such joint behavior have been observed in the expansion of the ^{161}Dy-^{40}K mixture [5] and in collective oscillations of the ^{6}Li-^{53}Cr mixture [90].

Here, we probe hydrodynamic behavior in an optically trapped Dy-K Fermi-Fermi mixture by characterizing the full spectrum of two-species dipole modes across a Feshbach resonance. Such modes (Sec. 6.2) can be understood as the response of the harmonically trapped mixture to a small displacement between the two components, and they can be conveniently excited by application of a species-dependent force (Sec. 6.3). In spin mixtures, the corresponding spin dipole mode has been observed in Refs. [100–102] and analyzed to characterize universal spin transport and ferromagnetic correlations. In species mixtures, the behavior is generally richer because the un-coupled oscillations of the two components naturally take place with different frequencies. This lifts a degeneracy that is normally present in optically trapped spin mixtures and there leads to a coexistence of the spin dipole mode with an undamped center-of-mass oscillation. In contrast, in interacting species mixtures, all modes are damped and exhibit complex-valued eigenfrequencies. Wide tuning of the in-terspecies s-wave interaction allows us to realize the full spectrum of dipole modes in the crossover from collisionless to hydrodynamic behavior. Below a critical friction strength, the spectrum consists of two damped oscillation modes. For stronger dissipative coupling, one of these modes splits into two pure exponential damping modes, whereas the other one ('crossover mode') survives with a substantially shifted eigenfrequency.

We show that all our observations (Sec. 6.4) can be described quanti-tatively within a simple model considering the center-of-mass motion of both species together with a dissipative coupling effect (friction) and a reactive coupling (mean-field interaction). Fitting the model to the experimental results, we extract the values for the corresponding coupling constants and analyze their resonance behavior. We find our experimental results on all modes in full agreement with the theo-retical model, which gives a complete picture of the crossover from collisionless to hydrodynamic behavior over a wide interaction range.

Deep in the hydrodynamic regime, the two exponential modes ex-hibit vastly different damping rates. While the slow mode corresponds to a strongly overdamped motion in position space, the fast mode essentially reflects a drag effect that, analogously to spin drag in a spin mixture, damps the relative motion in momentum space on a very short time scale. We find that the latter mode offers great prac-

tical advantages for accurate measurements, since it appears on a very short time scale, where other systematic effects like heating or interaction-induced deformations of the atomic clouds are negligible.

We finally go beyond the macroscopic description of the drag effect between the two species (Sec. 6.5), introducing a microscopic friction coefficient to describe the local interspecies friction effect separated from the global trap dynamics. We extract experimental values for this coefficient from our measurements of the fast damping mode. In our analysis we pay particular attention to the unitarity-limited regime on top of the resonance. This shows how our results are linked to a universal description of friction in a resonant two-component Fermi gas near quantum degeneracy and facilitates a comparison with other systems.

The detailed understanding of hydrodynamic behavior represents an essential prerequisite (Sec. 6.6) for future experiments exploring fermionic systems in interaction regimes beyond the present state of the art, such as novel superfluids.

6.2 TWO-SPECIES DIPOLE MODE SPECTRUM

6.2.1 *Model*

The basic idea to probe hydrodynamic behavior in a two-component Fermi gas by a dipole mode goes back to early theoretical work [103], which considered collisional relaxation of the spin-dipole mode in a balanced spin mixture of fermions. To describe the spectrum of dipole modes in a harmonically trapped two-species quantum gas, we adopt a model from the literature. In Refs. [104, 105] the model was applied to imbalanced situations (spin and species mixtures) with different populations and trap frequencies. In further theoretical work [106, 107], a reactive term was added to the model to describe the attractive or repulsive mean-field interaction between the two components. The approach is intuitive and straightforward on a phenomenological basis. Formally, it can be derived from the Boltzmann equation as described in some detail in Ref. [106], see also Refs. [103, 107, 108]. Solutions can also be obtained by numerical simulations [109, 110].

The model considers the one-dimensional motion of the mass centers of the two species. We assume rigid mass distributions, neglecting all dynamical effects related to the size and shape of the clouds. It contains three contributions to the forces on the atomic clouds, (1) the species-dependent restoring force of the harmonic trap, (2) a friction term for the relative motion, and (3) a reactive term for the mean-field interaction between the two components. All corresponding terms are linear, based on the assumptions of small displacements (smaller than the cloud sizes) and small relative velocities (smaller than typical velocities within the clouds).
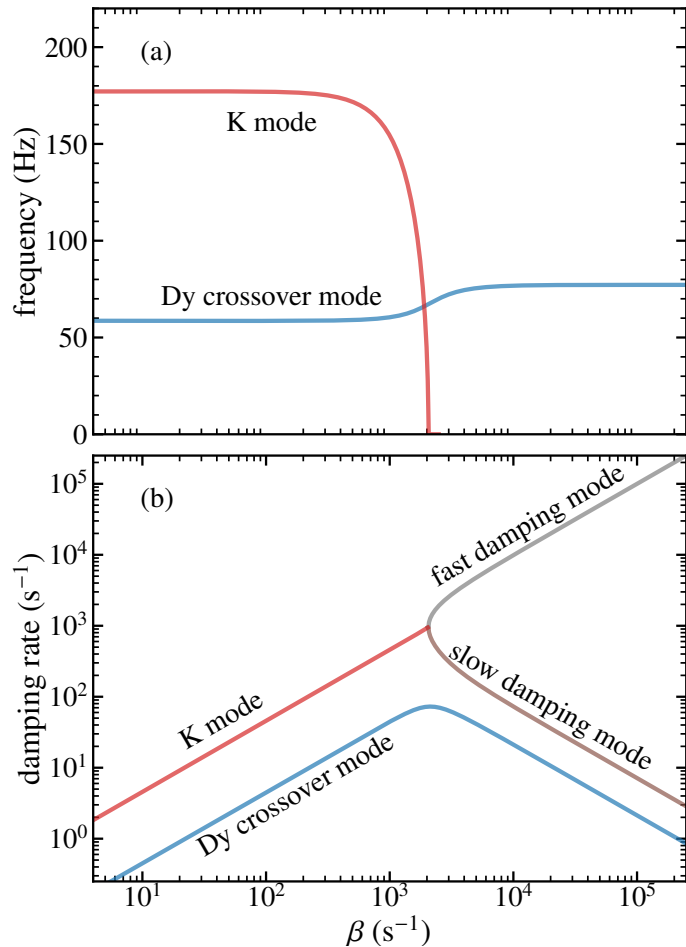
Figure 6.1: Predictions of the theoretical model for the dependence of dipole-mode frequencies (a) and damping rates (b) on the friction parameter β. Here we assume $\kappa = 0$ (no reactive coupling) and typical experimental conditions ($\omega_{\mathrm{D}y}/2\pi = 59\,\mathrm{Hz}$, $\omega_{\mathrm{K}}/2\pi = 177\,\mathrm{Hz}$, $N_{\mathrm{D}y}/N_{\mathrm{K}} = 2.5$).

Within these assumptions, the equations of motion (see App. 6.7 for more details) can be written as a system of second-order linear differential equations for the center-of-mass positions $y_{\mathrm{D}y}$ and y_{K} of the two clouds:

$$\ddot{y}_{\mathrm{D}y} = -\omega_{\mathrm{D}y}^2 y_{\mathrm{D}y} - q_{\mathrm{D}y}\beta\,\dot{\delta y} - q_{\mathrm{D}y}\kappa\,\delta y\,, \qquad (6.1a)$$

$$\ddot{y}_{\mathrm{K}} = -\omega_{\mathrm{K}}^2 y_{\mathrm{K}} + q_{\mathrm{K}}\beta\,\dot{\delta y} + q_{\mathrm{K}}\kappa\,\delta y\,, \qquad (6.1b)$$

with $\delta y = y_{\mathrm{D}y} - y_{\mathrm{K}}$ representing the relative displacement. The mass factors are defined as $q_{\mathrm{D}y} = M_r/M_{\mathrm{D}y}$ and $q_{\mathrm{K}} = M_r/M_{\mathrm{K}}$, where $M_r = M_{\mathrm{D}y}M_{\mathrm{K}}/(M_{\mathrm{D}y} + M_{\mathrm{K}})$ is the reduced total mass with $M_{\mathrm{D}y} = N_{\mathrm{D}y}m_{\mathrm{D}y}$ and $M_{\mathrm{K}} = N_{\mathrm{K}}m_{\mathrm{K}}$. The interaction coefficients β and κ represent the dissipative drag and the reactive interspecies interaction, respectively.

6.2.2 *Dipole modes*

Solving the equations of motion (6.1) as outlined in App. 6.7, we obtain the complete mode spectrum with its complex-valued eigenfrequencies and eigenvectors. We find that, under our typical experimental conditions, the dissipative friction effect generally dominates over the reactive mean-field effect. Note that this stands in contrast to experiments on dipole oscillations of mixed superfluids [111, 112], where the reactive coupling plays the dominant role. Here we focus our discussion on the general behavior in the case of dissipative coupling, at this point setting $\kappa = 0$ and deferring a discussion of the weaker effects induced by the reactive coupling to the later Sec. 6.4.2.

In Fig. 6.1, we show the dipole-mode frequencies (a) and damping rates (b) as a function of the friction parameter β, assuming typical experimental conditions. The behavior illustrates the transition of the system from a weakly coupled regime, where the oscillations of the two species keep their individual character, to a hydrodynamic regime, where both species behave jointly. This transition is marked by a critical value of the friction parameter ($\beta_{cr} \approx 2000\,\mathrm{s}^{-1}$ in our example). For weak friction, the system exhibits two damped oscillatory modes, which in the uncoupled limit correlate with the independent oscillations of the two species at their bare frequencies ω_{Dy} and ω_K. With increasing dissipative coupling, the two frequencies approach each other and damping increases for both modes. Once the critical damping rate β_{cr} is reached, one of the two oscillatory modes becomes overdamped and splits up into two purely exponential modes. Under the conditions of our experiments, this splitting happens for the mode correlated with the bare oscillation of the K component and we thus refer to this mode as "K mode". With further increasing dissipative coupling the damping of one of these exponential modes increases ("fast damping mode"), while it decreases for the other one ("slow damping mode").

The second oscillatory mode, which for $\beta \to 0$ correlates with the bare Dy oscillation, exists for any strength of the dissipative coupling. In contrast to the K mode, this mode shows a smooth crossover between the regimes of weak and the strong friction, and we thus refer to it as "Dy crossover mode". For $\beta < \beta_{cr}$ the coupling to the K component introduces damping along with a frequency upshift. With the friction strength reaching β_{cr}, the mode exhibits maximum damping. For further increasing coupling, the mode damping again decreases. For $\beta \gg \beta_{cr}$ the mode can be understood in terms of a locked hydrodynamic oscillation, in which both components act jointly and the system behaves like a single fluid.

6.2.3 *Case of strong friction*

The case of strong friction ($\beta \gg \beta_{cr}$) is of particular relevance for mixtures in the strongly interacting regime. Here one can derive rather simple analytical expressions for the frequency of the crossover mode and the damping rates of all modes. Solving the equations of motion (6.1) in a perturbative way, we obtain

$$\omega_c = \sqrt{\frac{M_1 \omega_1^2 + M_2 \omega_2^2}{M_1 + M_2}} \tag{6.2}$$

for frequency of the locked hydrodynamic oscillation in the crossover mode and

$$\Gamma_c = \frac{\frac{1}{2} M_r (\omega_2^2 - \omega_1^2)^2}{M_1 \omega_1^2 + M_2 \omega_2^2} \beta^{-1} \tag{6.3}$$

for the corresponding damping rate.

For the slow damping mode, we obtain

$$\Gamma_{slow} = \frac{(M_1 + M_2)\, \omega_1^2 \omega_2^2}{M_1 \omega_1^2 + M_2 \omega_2^2} \beta^{-1}, \tag{6.4}$$

while for the fast damping mode the simple result is

$$\Gamma_{fast} = \beta. \tag{6.5}$$

We point out that, in the strongly interacting limit, the fast damping mode can be interpreted as a direct manifestation of the drag effect between the two species in case of a relative motion. Measurements of damping of this particular mode, which appears on a very short time scale, allow us to extract the corresponding friction parameter β (also refered to as "drag coefficient") with high accuracy.

6.3 EXPERIMENTAL PROCEDURES

6.3.1 *Sample preparation*

The preparation of the optically trapped mixture has been described in our previous work [2, 12, 89]. Summarized in brief, a two-species magneto-optical trap (MOT) is loaded with ^{161}Dy from a Zeeman-slowed atomic beam and with ^{40}K from a two-dimensional MOT. The mixture is transferred into an optical dipole trap (ODT) operating with near-infrared light (wavelength 1064 nm). Both species are spin polarized in their lowest hyperfine sublevels $|F, m_F\rangle = |21/2, -21/2\rangle$ and $|9/2, -9/2\rangle$, respectively. Forced evaporative cooling, based on universal dipolar collisions within the Dy component [14, 15] and sympathetic cooling of K by Dy [2], brings the sample into degeneracy. Evaporative cooling is most efficiently performed at a low magnetic

field of 250 mG. The sample is then transferred to higher magnetic fields close to the interspecies Feshbach resonance near 7.3 G [12, 89], which we use for interaction tuning.

The final ODT, in which all experiments are carried out, is realized with trap light at 1547 nm. This is further in the infrared than the trap light used in all our previous experiments on Dy-K mixtures. We found that this reduces inelastic trap losses resulting from coupling to excited molecular states [89]. As a consequence of this change, the ratio of optical polarizabilities and thus trap depths for both species [3] is different from our previous work. With scalar polarizabilities of 383 a.u. for K [113] and 173 a.u. estimated for Dy [114, 115] we obtain a trap frequency ratio of $\omega_K/\omega_{Dy} = 2.99(4)$. We employ a standard crossed-beam ODT, realized with a horizontal beam (power 1.5 W, waist 87 µm) combined with a vertical beam (power 310 mW, waist of 123 µm). The trap provides a nearly axially symmetric optical potential with radial frequencies $\omega_{Dy}/2\pi = 59$ Hz and $\omega_K/2\pi = 177$ Hz (relevant for the dipole oscillations), and axial frequencies of about four times less. This corresponds to mean trap frequencies of $\bar{\omega}_{Dy}/2\pi = 37$ Hz and $\bar{\omega}_K/2\pi = 112$ Hz.

In our trap, we reach typical conditions of $N_{Dy} = 5 \times 10^4$ Dy atoms and $N_K = 2 \times 10^4$ K atoms a temperature of $T = 100$ nK. With Fermi temperatures $T_F^{Dy} = \sqrt[3]{6N_{Dy}}\,\hbar\bar{\omega}_{Dy}/k_B \approx 120$ nK and $T_F^K = \sqrt[3]{6N_K}\,\hbar\bar{\omega}_K/k_B \approx 260$ nK, we are in a regime of moderate Fermi degeneracy [2]. As discussed in App. 6.8, the spatial profiles of the two components nearly match (the Dy cloud being slightly larger), which provides us with a good overlap between both species.

The atom number ratio N_{Dy}/N_K can be varied by changing the loading times of the MOTs. We have investigated a maximum range between 0.5 and 7.5, but for most of our experiments we found optimum conditions for typical ratios near 2.5 (Sec. 6.4.2) or 4.5 (Sec. 6.4.3).

Magnetic levitation [2, 45] plays a very important role in our experiments. Without a vertical magnetic field gradient, which (partially) compensates for the effect of gravity, our rather shallow optical trap would not be able to keep the atoms. A 'magic' levitation gradient of 2.63 G/cm, with equal gravitational sag of both species [46, 89], ensures maximum spatial overlap between the two components. A controlled deviation from this particular gradient induces a vertical displacement between the two components. Correspondingly, we apply short gradient pulses (or a sequence of such pulses) as versatile tools to excite the two-species dipole modes.

---

2 Our temperatures are currently limited by residual heating effects in the transfer from the low evaporation magnetic field to the magnetic field region of interest, presumably by crossing many narrow intraspecies Dy Feshbach resonances [6].
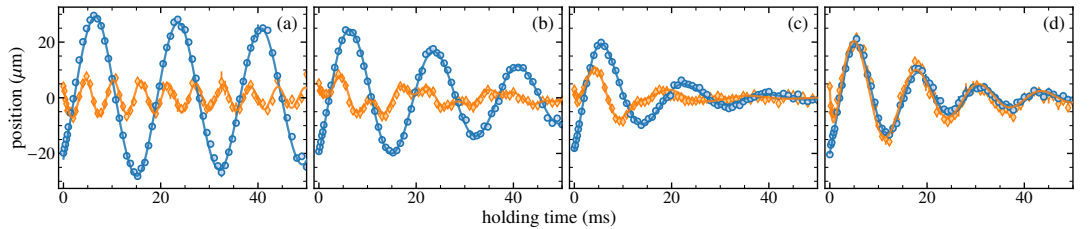
Figure 6.2: Center-of-mass oscillations of the Dy (blue) and K (orange) clouds for increasing interaction strength. The vertical position is obtained from time-of-flight images and plotted versus the hold time in the trap. The atom number ratio is fixed, $N_{\mathrm{Dy}}/N_{\mathrm{K}} = 2.42$. (a) Near the zero crossing of the scattering length, where $x \rightarrow \pm\infty$, the two clouds oscillate independently. (b) and (c) When approaching the resonance, $x = 1.6$ and 0.7, increasing interaction effects are observed. (d) On resonance, $x = 0$, the interspecies interaction results in a locked hydrodynamic motion of both components. The positions of the clouds are detected after a time of flight of $10\,\mathrm{ms}$ for Dy and $5\,\mathrm{ms}$ for K. For better comparison, the K signal is rescaled by a factor of 2. The uncertainties are smaller than the size of the symbols and the solid curves represent fits based on our theoretical model (see text).

6.3.2   *Interaction tuning*

We control the interacting strength in the mixture via a magnetically tuned Feshbach resonance [12, 89], which is centered at $B_0 = 7.276(2)\,\mathrm{G}$. In the resonance region, well-isolated from other resonances, the interspecies s-wave scattering length is given by

$$a = a_{\mathrm{bg}} - \frac{A}{\delta B}\,a_0, \tag{6.6}$$

where $\delta B = B - B_0$ represents the magnetic detuning, the parameter $A = 24.0(6)\,\mathrm{G}$ characterizes the strength of the resonance, and a_0 denotes the Bohr radius. The quantity $a_{\mathrm{bg}} = +23(5)\,a_0$ represents the background scattering length, which is rather small and can be neglected close to the resonance center.

For convenience in the following discussion, we introduce the dimensionless interaction parameter

$$x \equiv 1000\,a_0/a\,, \tag{6.7}$$

which close to resonance is proportional to the magnetic detuning, $x \approx -\delta B/24\,\mathrm{mG}$. The root-mean-square fluctuations of the magnetic field stay within typically $2.5\,\mathrm{mG}$, which translates into an interaction parameter uncertainty of $\sigma_x \approx 0.1$.

6.3.3   *Excitation and detection*

To excite the various two-species dipole modes we apply pulsed changes of the magnetic levitation gradient, thus inducing motion

in the vertical direction. These pulses are always applied at a large magnetic detuning where the interspecies interaction is negligible on the timescale of the excitation process. In all present experiments, we choose $\delta B = -132\,\text{mG}$, corresponding to $x = +4.9$. Having induced the motion of the two clouds in the weakly interacting regime, the magnetic field is ramped within typically 0.2 ms to the target value where the mode is studied at a well-defined interaction strength. This ramp, starting from below the resonance, always increases the magnetic field strength, which is crucial to avoid molecule association [17, 89].

Our typical magnetic gradient pulses are applied for 0.2 ms and increase the levitation gradient from its magic value (2.63 G/cm) to values about 1 G/cm higher. The higher gradient pulls both species out of the equilibrium position. This predominantly affects the Dy atoms because of their exceptionally large magnetic dipole moment of $10\,\mu_B$ (as compared to $1\,\mu_B$ for K); here μ_B is Bohr's magneton. To optimize the excitation of particular modes we can apply a second gradient pulse, which depending on the delay cancels or enhances the excited motion in a species-selective way. Another important parameter for the optimization of the excitation sequence is the time delay after which the magnetic field is ramped to its target value, which controls the point where the system is converted from the regime of independently oscillating motions to a coupled motion of both components. The details of the procedure depend on the particular mode to be excited.

After a variable hold time, in which the dynamics of interest takes place, we turn off the ODT and quickly switch the magnetic field to a large detuning ($\delta B = +472\,\text{mG}$, corresponding to $x = -36$). At this field, the two components expand ballistically without any significant further interaction. We finally apply standard time-of-flight imaging after 10 ms (for Dy) or 5 ms (for K) of free expansion, from which we determine the vertical center-of-mass positions of the two species.

Inelastic losses, reducing the number of trapped atoms during the hold time in the trap, generally stay well below a few 10% and have a weak effect on the oscillation curves. Only in a narrow range (few mG wide) very close to the center of the resonance, we have observed faster losses. In the worst case, we have measured lifetimes in the mixture of about 150 ms for Dy and 50 ms for the K component.

Typical oscillation signals are shown in Fig. 6.2 (see also Supplemental Material[3]) for increasing strength of the interspecies interaction. The observed behavior follows the basic predictions of the model introduced in Sec. 6.2. For the non-interacting case (a), both species oscillate independently at their individual trap frequencies. In this collisionless regime, damping due to interspecies interaction is essentially absent. Weak residual damping may be attributed to trap imperfections, such as anharmonicities. When approaching the resonance, the observed

---

3 See Supplemental Material at the following link

oscillations in (b) and (c) reveal increasing interaction effects. While both components show collisional damping, the K signal also reveals the emergence of two frequency components, which we interpret as a superposition of the K mode with the Dy crossover mode. In our experiments, the K component generally shows much stronger interaction effects because of the much larger total mass of the Dy cloud ($161N_{Dy}/40N_K \approx 10$). For the strongest interaction, realized on top of the resonance (d), we observe the expected locked hydrodynamic oscillation, in which both species oscillate jointly together with a well-defined frequency according to Eq. (6.2). In the regime of strong interactions, damping becomes weaker with increasing interaction, which confirms a central prediction pointed out in Sec. 6.2 for the Dy crossover mode.

The on-resonance oscillation curves in Fig. 6.2(d) reveal another interesting feature. The two curves overlap almost perfectly, owing to the locked hydrodynamic oscillation of the two species in the Dy crossover mode, except for an initial transient in the first millisecond. This is a signature of the fast damping mode, as we will discuss in detail in Sec. 6.4.3.

6.3.4   *Fit analysis of oscillation curves*

The frequencies and damping rates of the dipole modes at a specific interaction strength can be extracted by fitting the time-dependent solutions $y_{Dy}(t)$ and $y_K(t)$ of our model to the observed center-of-mass motion of the two species. See, for example, the solid lines in Fig. 6.2. For an oscillating mode, the in-trap positions, which describe the motion before time-of-flight expansion, follow damped harmonic oscillations

$$y_i^{trap}(t) = \hat{A}_i\, e^{-\gamma t} \cos(\omega t + \phi_i)\,, \qquad (6.8)$$

where $i = $ Dy, K. While, for a particular mode, the two species share the same frequency ω and the same damping rate γ, the amplitudes and phases are generally different. Taking into account the ballistic motion of the clouds during the free time-of-flight expansion, the resulting positions are described by

$$y_i(t) = \hat{A}_i\, e^{-\gamma t} \left[(1 - \gamma t_{TOF}) \cos(\omega t + \phi_i) \right. \\ \left. - \omega t_{TOF} \sin(\omega t + \phi_i)\right]. \qquad (6.9)$$

For a damping mode ($\omega = 0$), the behavior simplifies to

$$y_i(t) = \hat{A}_i\, e^{-\gamma t} (1 - \gamma t_{TOF})\,. \qquad (6.10)$$

Below the critical damping point, we fit the observed behavior by assuming a superposition of two oscillating modes according to Eq. (6.9). For each mode, there are six free parameters: frequency ω, damping

rate γ, and the species-dependent amplitudes A_{Dy} and A_{K} and phases ϕ_{Dy} and ϕ_{K}. In total we have to deal with 14 free parameters, six per mode and two additional parameters for the equilibrium positions of the two species without excitation. This complexity requires combined (not individual) fits to the data recorded for $y_{\mathrm{Dy}}(t)$ and $y_{\mathrm{K}}(t)$. Above the critical damping point the complexity of the fit remains the same as the fit has to take into account one oscillatory mode and two damping modes, the latter according to Eq. (6.10).

Finally, to fully characterize each mode, the quantities of interest are its frequency ω and damping rate γ (corresponding to the complex-valued eigenfrequencies) and the relative amplitude $A_{\mathrm{K}}/A_{\mathrm{Dy}}$ and phase $\Delta\phi \equiv \phi_{\mathrm{K}} - \phi_{\mathrm{Dy}}$ (representing the eigenvectors). A damping mode is fully characterized by the damping rate γ and the amplitude ratio $A_{\mathrm{K}}/A_{\mathrm{Dy}}$. In the experiments described in the following section, we measure all these quantities in the full range of interaction strengths across the resonance.

6.4 EXPERIMENTAL RESULTS

In this Section, we present our main experimental results on the two-species dipole mode spectrum across resonance. In Sec. 6.4.1, we first give an overview of the observed spectrum. Then, in Sec. 6.4.2, we discuss the Dy crossover mode in detail. This particular mode exists for any interaction strength and allows for an accurate determination of the parameters of our interaction model. Then, in Sec. 6.4.3, we turn our attention to the damping modes.

6.4.1 *Mode spectrum overview*

We recorded a large set of oscillation curves for typical atom numbers $N_{\mathrm{Dy}} = 5.8 \times 10^4$, $N_{\mathrm{K}} = 2.4 \times 10^4$ ($N_{\mathrm{Dy}}/N_{\mathrm{K}} = 2.42$) and temperatures $T \approx 100\,\mathrm{nK}$. The 30 recorded curves (per species) cover an interaction parameter range of $-6 \leq x \leq +6$ ($|a| \geq 167\,a_0$). Each curve consists of 90 data points with 3 to 5 repetitions taken in a time interval of 70 ms after the excitation by a double-pulse sequence. To get a first impression of the mode spectrum, we carried out a fast Fourier transform (FFT) for each curve and visualize the resonance behavior of the amplitude spectrum in the pseudo-color plots of Fig. 6.3, where panel (a) refers to the signal obtained from the K component and (b) from the Dy component.

Already the simple FFT analysis demonstrates the essential features of the mode spectrum across resonance. In the K signal (a), we can identify both modes with their bare frequencies of 177 Hz and 59 Hz in the weakly interacting regime. On resonance, only the locked oscillation ($\sim 78\,\mathrm{Hz}$) is observed. In the Dy signal (b), the off-resonant K mode excitation is too weak to be observed in the data, but the reso-
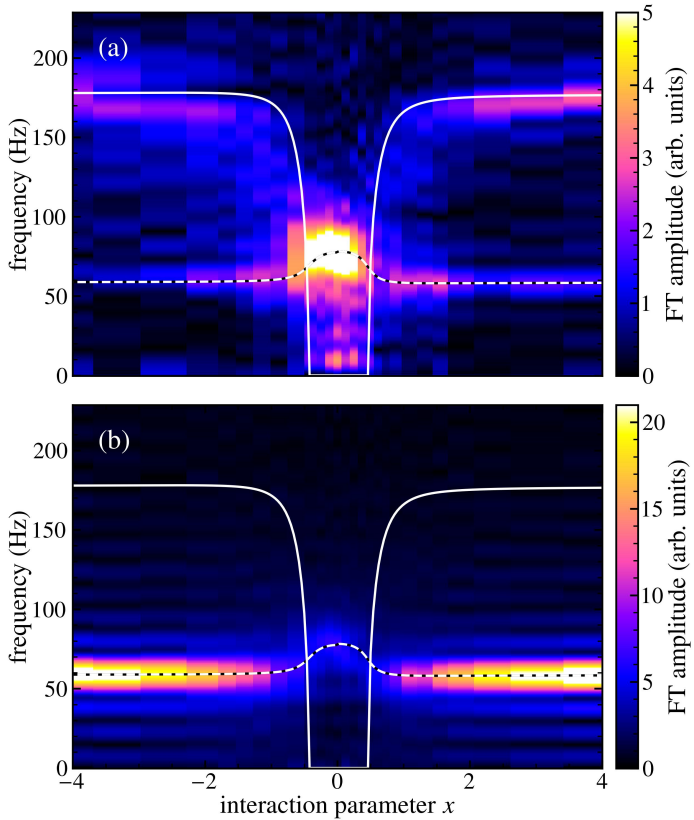
Figure 6.3: Mode spectrum across the resonance. The pseudo-color plot shows the amplitude spectrum derived by Fourier transforming the oscillation signals recorded for (a) the K atoms and for (b) the Dy atoms. The solid white line and the black-white dashed line are the theoretical curves for the K mode and the Dy crossover mode (for details see Sec. 6.4.2). Note that the horizontal stripes visible in (b) are an artefact related to the Fourier transform of the rectangular time window.

nant crossover to the locked mode can be clearly seen. For comparison, we also show theoretical curves for the frequencies of the Dy crossover mode (dashed line) and the K mode (solid line) as derived from our model and explained in detail in the following Sections.

6.4.2 *Crossover mode*
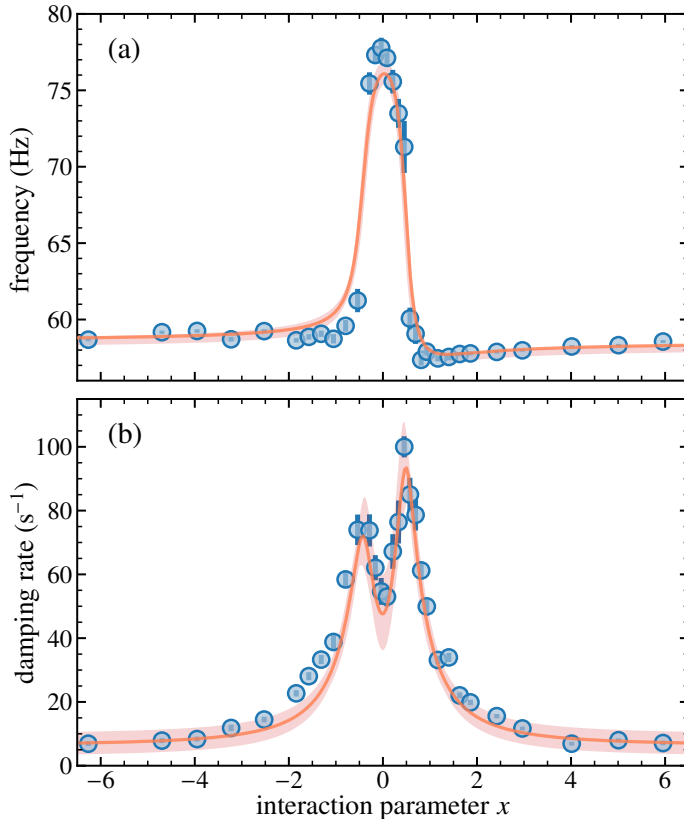
Figure 6.4: Resonance behavior of (a) frequency and (b) damping rate of the Dy crossover mode. The blue data points represent the measured values with 1σ error bars (in most cases smaller than the symbol size). The red solid curves show the results of a joint fit to frequency and damping based on the model presented in Sec. 6.2. The red shaded area represents the 95% confidence band of the fit.

We analyze the recorded oscillation curves as explained in Sec. 6.3.4, extracting full information on the mode spectrum. Based on the theoretical model of Sec. 6.2 and model assumptions for the resonance dependence of the interaction coefficients $\beta(x)$ and $\kappa(x)$, we can then fit the full resonance behavior. Here, as a case of particular interest, we focus on the resonance behavior of the Dy crossover mode.
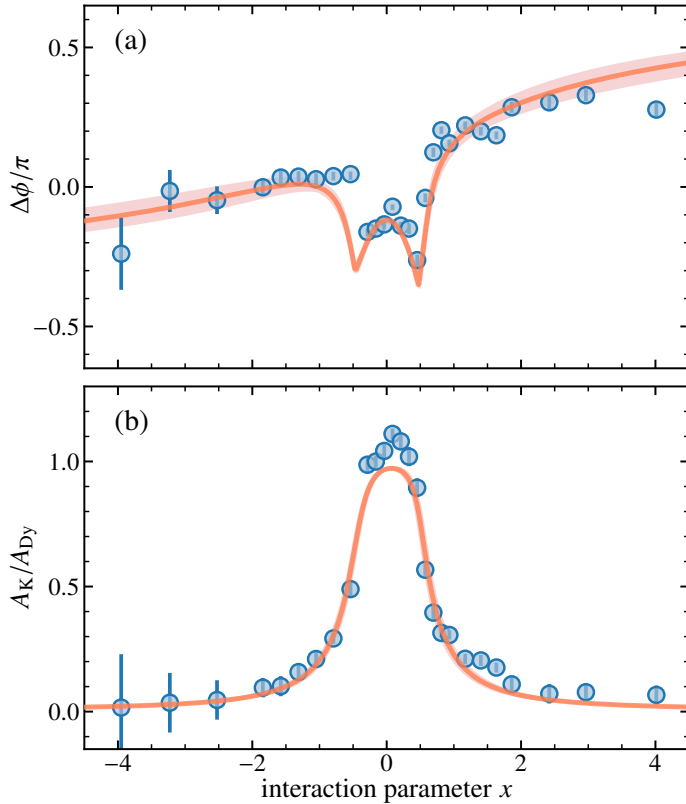
Figure 6.5: (a) Phase shift $\Delta\phi = \phi_K - \phi_{Dy}$ and (b) amplitude ratio A_K / A_{Dy}
of the two species oscillating in the Dy crossover mode. The blue
data points represent the measured values with 1σ error bars.
The red solid curves show the result of our model with the same
parameter values as used in Fig. 6.4 (no independent fit carried
our here).

6.4.2.1 *Frequency and damping rate*

The data points in Fig. 6.4 show the experimental values obtained for
the frequency and damping rate. In panel (a), the frequency change
from the bare oscillation (56 Hz) for weak interaction to the locked
oscillation (78 Hz) on resonance is clearly visible. The locked oscilla-
tion frequency is in full agreement with Eq. (6.2). The damping rate
measurements in panel (b) reveal maxima at $|x| \approx 0.5$ ($|a| \approx 2000\,a_0$),
indicating that the critical damping rate β_{cr} is reached at the corre-
sponding interaction strength. Closer to resonance, a clear decrease of
damping is observed, in accordance with the behavior in Fig. 6.2(d).

While all these observations can essentially be understood within
our model as a result of friction (dissipative coupling) between the two
species, our data also reveal a distinct asymmetry, which manifests
itself in slightly higher frequencies measured on the side of attractive
interaction ($x < 0$) and somewhat larger damping rates observed on
the repulsive side ($x > 0$). This asymmetry points to the effect of

reactive interaction, which we have so far neglected in our discussion of the mode spectrum in Sec. 6.2 by setting $\kappa = 0$.

The phase difference and the relative amplitude of the two-species oscillations provide additional information on the resonance behavior of the mode. Our corresponding results are displayed in Fig. 6.5. The phase in panel (a) exhibits a pronounced asymmetry, which turns out to be the most pronounced manifestation of the reactive interaction between the two components. The amplitude ratio in panel (b) clearly shows that, in the weakly interacting regime, the mode is dominated by the oscillation of the Dy component with a small admixture of K oscillation. For increasing interaction this smoothly connects to a locked oscillation, where both components feature essentially the same amplitude.

6.4.2.2 *Fit analysis*

For a quantitative interpretation of the experimental observations in terms of the model presented in Sec. 6.2, we introduce the functions $\beta(x)$ and $\kappa(x)$ to describe the dissipative and reactive coupling across the resonance. Based on standard theory of resonant *s*-wave scattering and adopting a collisional mean-field approach (see App. 6.9), we write

$$\beta(x) = \frac{\beta^*}{x^2 + x_c^2} \tag{6.11}$$

and

$$\kappa(x) = -\frac{\kappa^* x}{x^2 + x_c^2} . \tag{6.12}$$

Here the quantities β^* and κ^* characterize the overall strength of the dissipative and the reactive coupling, respectively, depending on the particular experimental conditions. The parameter $x_c = 1000\, a_0/a_c$ corresponds to a characteristic value of the scattering length, a_c, above which the interaction is limited by the finite collisional momenta. In a thermal gas, this length is determined by the thermal de Broglie wavelength of the relative motion, $a_c \approx 1.21\, \lambda_{th}/(2\pi)$ with $\lambda_{th} = \sqrt{2\pi\hbar^2/(m_r k_B T)}$; see App. 6.9.1.

We perform a combined fit to the complete set of measurements of frequency and damping rate, as displayed in Figs. 6.4(a) and (b). The three main parameters of the fit are β^*, κ^* and a_c. The bare K frequency is fixed to a value $\omega_K/2\pi = 177.2\,\text{Hz}$, accurately determined in a separate measurement. The bare Dy frequency, for which separate measurements are subject to relatively large uncertainties [4], is kept

---

4 The bare oscillation frequencies can be measured with standard methods [3]. For both species, the absolute uncertainties are similar, which means that typical uncertainties are three times large for Dy than for K. Moreover, the trap anharmonicity has a stronger effect in the shallower potential experienced by the Dy atoms.

as a free parameter and its value is extracted from the fit ($\omega_{\mathrm{Dy}}/2\pi =$ 58.6 Hz). In the fit to the damping rate data, we phenomenologically take into account a weak background ($\sim 6\,\mathrm{s}^{-1}$), which was measured in the absence of interspecies interactions near the zero crossing of the scattering length.

Our fit (solid lines in Fig. 6.4) describes the experimentally observed resonance behavior remarkably well. All basic features of the Dy crossover mode are reproduced and satisfying quantitative agreement is reached within the uncertainties. For the dissipative coupling strength we obtain the parameter value $\beta^* = 750(60)\,\mathrm{s}^{-1}$, which is fully consistent with the theoretical result of $680(120)\,\mathrm{s}^{-1}$ from the collisional model described in App. 6.9. Maximum damping is observed at $|x| = 0.46$ ($|a| = 2200\,a_0$), which according to Eq. (6.11) corresponds to a critical value of $\beta_{cr} = 2100\,\mathrm{s}^{-1}$ for the friction parameter. This fully agrees with the expectation from Fig. 6.1. The fit also provides us with a value for the friction parameter on resonance, $\beta_0 = \beta^*/x_c^2 \approx 5000\,\mathrm{s}^{-1}$.

For the finite-momentum limitation of the interaction strength, as imposed by unitarity, our fit yields $x_c = 0.38(3)$, corresponding to $a_c = 2600(200)\,a_0$. This is essentially consistent with the value $a_c = 3500\,a_0$ as expected under the present experimental conditions for collisions in a thermal gas; see App. 6.9.1. In view of the moderate Fermi degeneracy in our mixture, it is also close to the length scales set by the inverse Fermi wavenumbers of the two species, $1/k_F^{\mathrm{Dy}} \approx 2100\,a_0$ and $1/k_F^{\mathrm{K}} \approx 2900\,a_0$.

Remarkably, the fit also reproduces the slight asymmetry in the data of Fig. 6.4, for which it yields a value of $\kappa^* = 7.7(1.5) \times 10^4\,\mathrm{s}^{-2}$ for the reactive coupling strength. This is about twice larger than the result of $\sim 4 \times 10^4\,\mathrm{s}^{-2}$ calculated within our mean-field approach in App. 6.9, but still reasonable in view of the simplifying assumptions of the theoretical approach, such as neglecting interaction-induced distortions of the spatial cloud profiles.

Keeping the parameter values as extracted from the fit above, we also apply our model to describe the resonance behavior of the phase difference $\Delta\phi \equiv \phi_{\mathrm{K}} - \phi_{\mathrm{Dy}}$ and the amplitude ratio $A_{\mathrm{K}}/A_{\mathrm{Dy}}$ between the two components (red solid lines in Fig. 6.5). Without any further fitting, we find excellent agreement with the measured values (blue data points). This again confirms the validity of the model introduced in Sec. 6.2.

A particularly interesting observable is the phase difference $\Delta\phi$ between the oscillations of the Dy and the K component in the crossover mode. Here the contribution by the reactive mean-field effect plays an important role over the whole range of interaction investigated. The observed behavior of the phase can only be understood by taking into account the reactive term. For $\kappa = 0$, our model would predict a flat phase across resonance outside of the locking region, whereas a finite

value of κ breaks the symmetry and shifts the phase even for moderate interaction strength in the non-resonant regime ($|x| > 1$). Note that, away from resonance, the strength of the reactive coupling effect falls of proportional to x^{-1}, whereas the dissipative effect drops faster with x^{-2}. In particular the larger phase difference on the repulsive side can be understood as a result of a delay originating from the repulsion between the two clouds.

Our results provide a complete characterization of the two-species 'crossover' dipole mode that exists for any interaction strength across a resonance, with full information on the complex-valued eigenfrequency (frequency and damping rate) and on the eigenvector (relative phase and amplitude ratio). While previous experiments [90, 104, 105, 116] have demonstrated the effect of a joint oscillation of both species as an effect of dissipative coupling (interspecies friction), we also observe the weaker additional effect of reactive coupling, caused by attraction or repulsion between the two components.

6.4.2.3 *Dependence on atom number ratio*

To further investigate the validity of the theoretical model, we examine the frequency and the damping rate of the Dy crossover mode on resonance in a wide range of atom number ratios $N_{\mathrm{Dy}}/N_{\mathrm{K}}$ from 0.5 to 7.5. In Fig. 6.6, we show the experimental results (data points) in comparison with the predictions of the theoretical model (solid lines). In this set of measurements, the particular experimental conditions (absolute atom numbers N_{Dy}, N_{K}, and temperature T) vary, depending on the particular loading sequence applied. For the lowest number ratio, $N_{\mathrm{Dy}} = 4.2 \times 10^4$, $N_{\mathrm{K}} = 8.3 \times 10^4$, and $T = 170\,\mathrm{nK}$, For the highest ratio, $N_{\mathrm{Dy}} = 1.5 \times 10^5$, $N_{\mathrm{K}} = 2.0 \times 10^4$, and $T = 130\,\mathrm{nK}$.

For calculating the theoretical frequency and damping rate values, we have to consider the individual conditions for each data point. We separately measure the numbers N_{Dy}, N_{K} and the temperature T. Following App. 6.9.1, we calculate the value of the friction parameter β. The reactive interaction can be neglected on resonance ($\kappa = 0$). Again applying the model of Sec. 6.2 we can finally calculate the mode frequency and damping rate.

With increasing $N_{\mathrm{Dy}}/N_{\mathrm{K}}$, the measurements demonstrate the behavior of the oscillation frequency expected from Eq. (6.2): The frequency of the locked oscillation changes from a value near the bare K frequency to a value close to the bare Dy frequency. On the other hand, the damping rate decreases with increasing $N_{\mathrm{Dy}}/N_{\mathrm{K}}$, which reflects the decreasing effect of the K component on the oscillation of Dy, the latter having a much larger total mass.
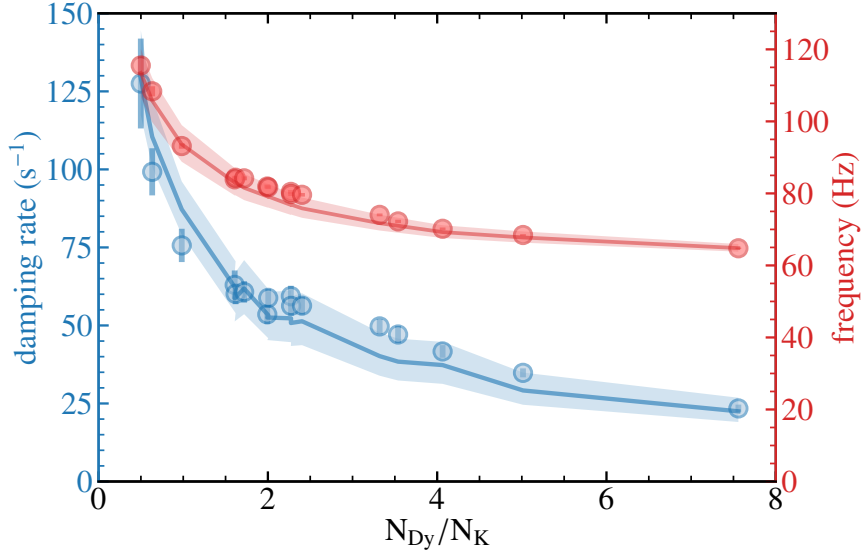
Figure 6.6: Frequency and damping rate of the Dy crossover mode on resonance ($x = 0$) as a function of the atom number ratio. With increasing N_{Dy}/N_K, the temperature decreases from 170 to 130 nK. The bullet symbols represent the experimental data with 1σ uncertainties. The solid curves show the theoretical behavior according to our model (see text). The shaded regions represent the effect of $\pm 10\%$ atom number uncertainties.

6.4.3   Damping modes

In this Section, we focus on the two non-oscillating damping modes. According to our model, introduced in Sec. 6.2, the fast and the slow damping mode exist if the friction parameter exceeds a critical value ($\beta > \beta_{cr}$). These two modes coexist with the oscillating crossover mode discussed before.

The experiments have been carried out in the same optical trap setting as in Sec. 6.4.2 ($\omega_{Dy}/2\pi = 58.6$ Hz, $\omega_K/2\pi = 177.2$ Hz), but with a larger number of initially loaded Dy atoms. After evaporative cooling, we keep $N_{Dy} = 8.6 \times 10^4$ and $N_K = 1.9 \times 10^4$ atoms, corresponding to a number ratio of $N_{Dy}/N_K = 4.5$. The temperature of the mixture is $T = 130$ nK. Our choice of a larger number of Dy atoms (as compared to the experiments on the crossover mode) was originally motivated by the idea to realize a broader magnetic-field range where hydrodynamic behavior occurs and thus to obtain data with better resolution on the interaction parameter scale. However, it turned out that this effect is rather small and that the overall damping behavior is quite robust against changes in the number ratio.

For excitation and detection, we employ the methods described in Sec. 6.3.3. The mixture is first kicked by a single magnetic-gradient pulse under conditions of negligible interspecies interaction. After a carefully chosen time delay, the interspecies interaction is introduced

by rapidly ramping the magnetic field to its target value. For exciting the fast damping mode, the delay is chosen to maximize the velocity difference between the two species, while minimizing the spatial displacement. For the slow damping mode, the delay is set to maximize the initial displacement, keeping the velocity difference small. For detection, we perform standard time-of-flight imaging, extracting the center-of-mass velocities at the time of release from the corresponding displacements observed after long times of ballistic flights ($t_{TOF} = 10\,\text{ms}$ for Dy, and 5 ms for K). In addition, for the slow mode, we also apply *in*-situ imaging to detect the center-of-mass positions of the two components.
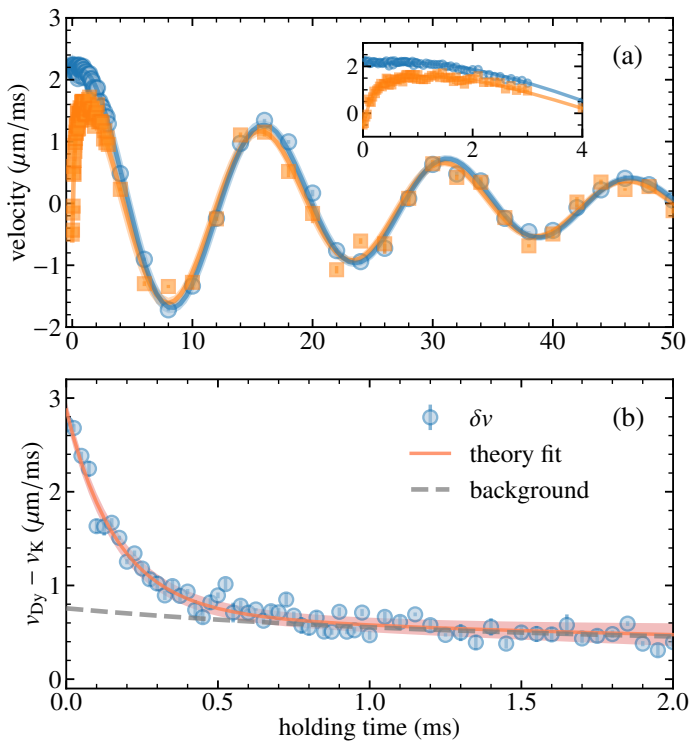
Figure 6.7: Fast damping mode on resonance for $N_{Dy}/N_K = 4.5$. In (a), we show the center-of-mass velocities of the two components, Dy (blue) and K (orange), as a function of the hold time in the ODT. The solid curves represent fits based on a superposition of the two damping modes and the crossover mode, as detailed in Sec. 6.3.4. The inset zooms into the initial behavior from 0 to 4 ms. In (b), we plot the velocity difference between Dy and K in the first 2 ms. While the solid curve represents the result of the full fit, the dashed line illustrates the slowly varying background resulting from both the slow mode and the crossover mode. The difference between the solid and the dashed curve corresponds to the fast mode. The symbols represent the experimental data with standard errors derived from five repetitions per hold time. The shaded region indicates the 95% confidence band of the fit.

6.4.3.1 *Fast damping mode*

The fast damping mode appears as a direct manifestation of the rapid reduction in the relative velocity of the two species caused by strong friction in the resonantly interacting regime. Figure 6.7(a) demonstrates the basic behavior as observed for resonant interspecies interaction ($x = 0$). Right after the dipole-mode excitation in the weakly interacting regime and a rapid quench onto resonance, which effectively takes about $20\,\mu s$ [5], the initial velocities (at zero hold time) of the K and Dy clouds differ substantially. Then, within less than one millisecond, the system reaches the regime of locked oscillations (inset). Our fitting model (solid lines) reproduces the observed behavior very well, including the initial transient. Figure 6.7(b) demonstrates the evolution of the velocity difference with time. The fast mode shows the expected exponential decay with a short damping time of about $1/\Gamma_{fast} = 170\,\mu s$. It appears on a slowly varying background, which is caused by the slow damping mode together with the oscillating crossover mode.

The fast damping also highlights the very large rate of elastic collisions in the resonantly interacting mixture. With the approximation $\beta \approx \Gamma_{fast}$, see Eq. (6.5), we obtain $\Gamma_{coll} = 2.0 \times 10^8\,\mathrm{s}^{-1}$ for the total rate of elastic collisions, see App. 6.9.1 for details. This corresponds to mean rates per Dy atom and per K atom as large as $\Gamma_{coll}/N_{Dy} = 2\,300\,\mathrm{s}^{-1}$ and $\Gamma_{coll}/N_K = 10\,500\,\mathrm{s}^{-1}$, respectively.

6.4.3.2 *Slow damping mode*

The slow damping mode corresponds to an overdamped motion, in which the spatially displaced clouds relax slowly towards the equilibrium position in the trap center. In Fig. 6.8, we show an example, which was recorded on resonance by in situ imaging. Here the initial position difference is about $10\,\mu m$, with the K cloud being nearly in the trap center, while the Dy cloud is displaced. In panel (a), the center-of-mass positions of both components show damped harmonic oscillations, which result from an excitation of the crossover mode (discussed before in Sec. 6.4.2). In the position difference, as shown in panel (b), the oscillations are reduced and an exponentially decaying background shows up clearly. The latter corresponds to the slow damping mode.

A fit based on our theoretical model (solid lines in Fig. 6.8) reproduces the observed behavior and yields a value of $130\,\mathrm{s}^{-1}$ for the damping rate Γ_{slow} on resonance. However, from corresponding measurements using the time-of-flight method (not shown), we obtain a

---

5 During our $200\text{-}\mu s$ linear ramp from the preparation field ($\delta = -132\,\mathrm{mG}$) onto resonance, the systems spends only about $20\,\mu s$ in the strongly interacting regime. Thus, the interaction quench is almost an order of magnitude faster than the fastest response of the system.
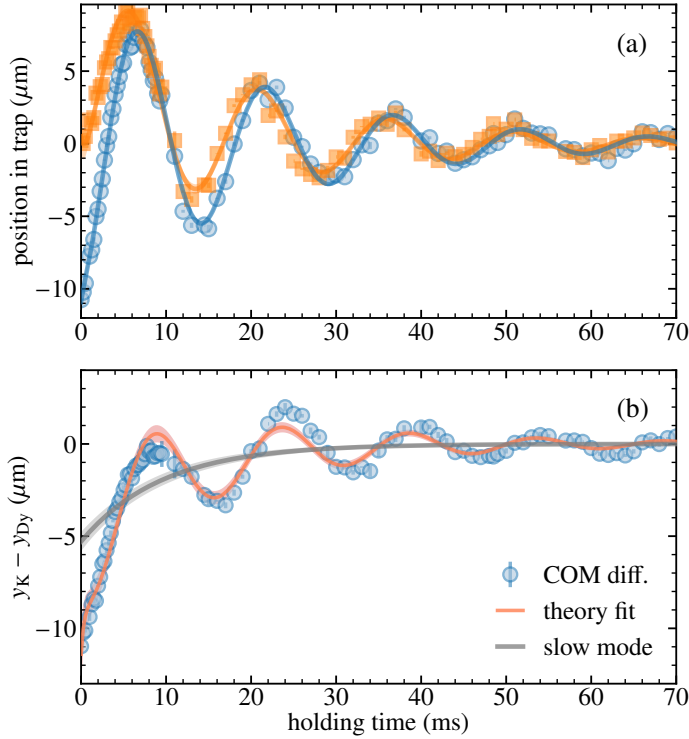
Figure 6.8: Slow damping mode on resonance for $N_{Dy}/N_K = 4.5$. (a) Temporal evolution of the COM positions of the Dy (blue) and K (orange) clouds in the ODT. The solid curves are the fits based on our theoretical model and procedures outlined in Sec. 6.3.4 ($t_{TOF} = 0$ for *in*-situ imaging). (b) Difference between COM positions for the Dy and K clouds. The red solid curve corresponds to the full theoretical model with all three modes, and the gray solid curve shows the contribution of the slow damping mode. The blue symbols represent the experimental data point with standard errors obtained from five repetitions per point. The shaded region around the fit curves indicates the 95% confidence band.

somewhat higher value of $190\,s^{-1}$, which is not consistent with the above value within the statistical uncertainties. A closer inspection of the fitting analysis reveals an apparent effect of systematic differences between the observed behavior and the fitting model. Although these differences remain rather small, we find that the best estimates obtained for the values of the fit parameters can significantly depend on the initial conditions and the time window selected for the fits. This problem does not occur for all other modes, where the fitting turns out to be very robust. Nevertheless, our results clearly confirm the existence of the slow damping mode on resonance and show that it is damped with a rate between the crossover mode ($\Gamma_c = 35\,s^{-1}$) and the fast damping mode ($\Gamma_{fast} = 5600\,s^{-1}$). Our result is also consistent with Eq. (6.4), which predicts $\Gamma_{slow} = 150\,s^{-1}$.

6.4.3.3 *Resonance crossover*

We now consider the damping behavior of the dipole modes across the resonance. The experimental data in Fig. 6.9 show how, for strong interactions, the oscillating K mode splits into the two damping modes, while the Dy crossover modes exhibits the continuous behavior already discussed in Sec. 6.4.2. To analyze the data we carry out a combined fit to the damping rates of the observed modes in the same way as done for the crossover mode in Sec. 6.4.2.2. The fit is carried out with only two free parameters, β^* for the overall dissipative coupling strength and x_c for the effective finite-momentum limitation; see Eq. (6.11). Here, the reactive coupling constant is set to $\kappa^* = 0$ as the effect is too weak to be resolved in this data set [6]. For the weakly damped Dy crossover mode, as in Sec. 6.4.2, we take into account a background damping rate of $6 \, \mathrm{s}^{-1}$, which was measured in the absence of interspecies interactions.

The combined fit reproduces the experimental data well and yields the parameter values $\beta^* = 1090(60) \, \mathrm{s}^{-1}$ and $x_c = 0.45(3)$, corresponding to $\beta_0 = \beta^*/x_c^2 \approx 5400 \, \mathrm{s}^{-1}$ on resonance. For the critical value of the friction parameter, above which the damping modes appear, we extract $\beta_{cr} = 2100 \, \mathrm{s}^{-1}$. For the conditions of the present set of experiments, this corresponds to $|x| \leq 0.56$ ($|a| \geq 1800 \, a_0$). This is rather close to the set of measurements on the crossover mode analyzed in Sec. 6.4.2.2 and shows that the particular number ratio ($N_{Dy}/N_K = 4.5$ instead of 2.4) does only weakly affect the extension of the resonant range in which the system exhibits hydrodynamic behavior.

It is worth to note a detail of the fit. Because of the systematic deviations of unclear origin encountered for the slow damping mode, we have given zero weight to the corresponding data points (marked 'slow' and 'in situ'). The solid curve for the slow mode is derived from the combined fit to the other modes and shows good agreement with the questionable data points. This gives an *a posteriori* justification for our measurements on the slow damping mode.

Our measurements clearly demonstrate the overall behavior predicted by our theoretical model as presented in Sec. 6.2. In particular, we have studied the resonance crossover, where we have observed the splitting of one of the two oscillating modes (K mode) into two non-oscillating exponentially damped modes.

---

6 In contrast to the fit analysis of the crossover mode data in Fig. 6.4, we cannot extract a meaningful value for the reactive coupling constant κ^* from the damping rate data of Fig. 6.9. This is a result of a combination of different reasons: The larger number ratio N_{Dy}/N_K reduces the damping rate asymmetry of the Dy component, statistical uncertainties are larger, since less data points have been taken in the relevant range, and frequency data are not considered here. A fit with κ^* as an additional free parameter would produce a small value with a large uncertainty, which would be consistent with both zero effect and the small value that we would expect from the model in App. 6.9.2
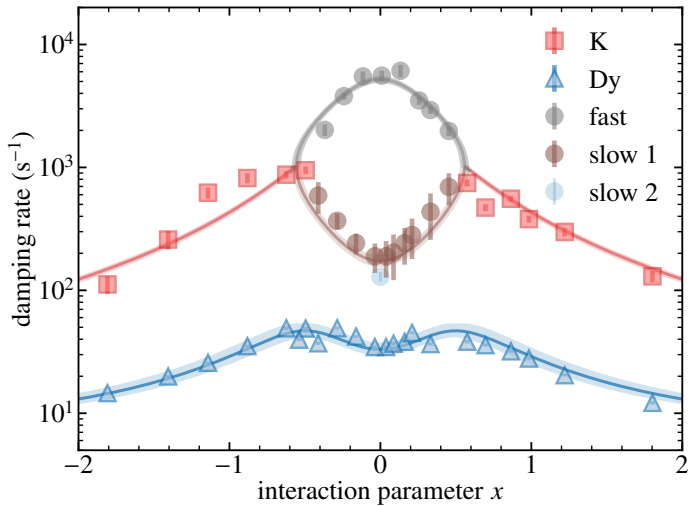
Figure 6.9: Damping rates of all dipole modes across the resonance. The symbols represent the experimental measurements and the solid lines show the result of a combined fit to the data. While, close to resonance, the Dy crossover mode (blue triangles) makes a smooth transition into the hydrodynamic regime, the K mode (red squares) loses its oscillatory character and splits into two exponentially damped modes (circular symbols). All measurements have been taken with time-of-flight imaging, with the exception of the single data point for the slow mode (labeled 'slow 2'), for which we have applied *in* situ imaging.

6.5 MICROSCOPIC VIEW ON FRICTION

So far, we have described the mode damping in terms of the friction parameter β as introduced in Sec. 6.2.1. This parameter accounts for the total friction force between the two components and thus quantifies its effect on the relative center-of-mass motion. Here, in Sec. 6.5.1, we consider the local contributions to friction in the inhomogeneous mixture and introduce a microscopic quantity to describe the friction effect locally. We extract trap-averaged values for this microscopic friction coefficient from the measured damping rates reported in the previous section, and we demonstrate the corresponding resonance behavior. In Sec. 6.5.2, we finally focus on the resonant case of unitarity-limited interactions and interpret our results in terms of universality.

6.5.1   *Local friction*

In the inhomogeneous situation of the trapped mixture, the global friction effect can be understood by considering the sum of the local contributions originating from different regions of the trap. While the number densities of the two species, $n_1(\mathbf{r})$ and $n_2(\mathbf{r})$, are local quantities, their relative velocity $\delta\dot{y} = \dot{y}_1 - \dot{y}_2$ can be considered as uniform under our basic assumption of two rigid clouds with a relative

center-of-mass motion. Accordingly, we start with a general ansatz for the position-dependent volume density of the friction force acting between the two species:

$$f_1(\mathbf{r}) = -\gamma(\mathbf{r})\, n_1(\mathbf{r})\, n_2(\mathbf{r})\, \delta\dot{y}\,. \tag{6.13}$$

In this way, we define a *microscopic friction coefficient* $\gamma(\mathbf{r})$ as a local quantity. The basic idea underlying this ansatz is to separate two-body behavior in a thermal gas, which leads to friction proportional to the local number densities, from many-body effects. For elastic collisions in a thermal gas without degeneracy effects, it is straightforward to show that γ is independent of the position. This can be seen from the Boltzmann equation, where position and momentum dependence separate in this case. In principle, the friction coefficient γ allows for a characterization of the microscopic physics of interspecies friction, separated from macroscopic properties of the trapped mixture, such as cloud sizes and shapes.

In many-body interaction regimes, γ will become position-dependent and we have to take into account the inhomogeneity of the mixture to derive a trap-averaged value $\langle\gamma\rangle$. After integrating Eq. (6.13) over the volume and introducing the reduced total mass M_r as defined in App. 6.7, we obtain an expression for the global damping rate of the relative motion:

$$\beta = -\frac{\delta\dot{y}}{\delta\dot{y}} = \frac{1}{M_r} \int \mathrm{d}V\, \gamma(\mathbf{r})\, n_1(\mathbf{r})\, n_2(\mathbf{r})\,. \tag{6.14}$$

We now introduce a general definition for the trap average of any position-dependent quantity $\chi(\mathbf{r})$ as

$$\langle\chi\rangle \equiv \frac{1}{n_\Omega} \int \mathrm{d}V\, \chi(\mathbf{r})\, n_1(\mathbf{r})\, n_2(\mathbf{r})\,, \tag{6.15}$$

where $n_\Omega \equiv \int \mathrm{d}V n_1 n_2$ is the overlap density (App. 6.8). Applying this definition to $\gamma(\mathbf{r})$, Eq. (6.14) can be rewritten as a relation between the trap-averaged microscopic friction coefficient and the global friction parameter,

$$\langle\gamma\rangle = \frac{M_r}{n_\Omega}\, \beta\,. \tag{6.16}$$

To extract experimental values for $\langle\gamma\rangle$ from our damping rate measurements (Sec. 6.4.3), we first have to convert the damping rates measured for a specific mode to the corresponding values of β. For this purpose, we employ our theoretical model, inverting curves such as shown in Fig. 6.1(b). This is particularly straightforward for the fast mode, since its damping rate Γ_{fast} approaches β in the limit of strong friction (Sec. 6.2.3). The fast damping mode also has the great advantage that it acts on a very short timescale of typically much less than a millisecond, which is about two orders of magnitude faster
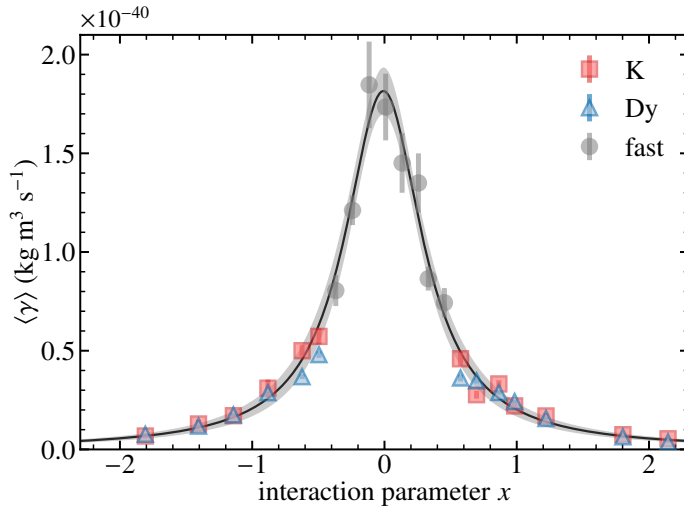
Figure 6.10: Experimental values for the trap-averaged microscopic friction coefficient $\langle\gamma\rangle$ across the resonance, based on the data shown in Fig. 6.9. The gray circles, red squares, and blue triangles (shown with standard errors) represent the values extracted from the fast damping mode, Dy crossover mode, and K mode, respectively. The black solid curve is a Lorentzian fit to the fast damping mode only, with the gray-shaded area representing the 1σ confidence band.

than the oscillation in the trap. In this short time, perturbations by losses and heating effects as well as distortions of the cloud can be completely neglected, which minimizes systematic effects compromising our measurements. We therefore expect measurements based on the fast damping mode to be superior to measurements based on the other modes.

Figure 6.10 shows the values that we obtained for the trap-averaged microscopic friction coefficient $\langle\gamma\rangle$ across the resonance, based on the data points shown in Fig. 6.9. We find that the dependence on the interaction parameter x is well described by a Lorentzian curve. A corresponding fit yields the on-resonance value

$$\langle\gamma_0\rangle = 1.8(2) \times 10^{-40}\,\text{kg}\,m^3\,s^{-1}\,, \tag{6.17}$$

which characterizes the strength of the interaction in the unitarity limit. For the width we obtain $x_c = 0.33(3)$, corresponding to $a_c = 3000(300)\,a_0$. This well agrees with the expectation $a_c = 3100\,a_0$ based on Eq. (6.38). We note that our fit only takes into account the fast-mode measurements (eight central data points, gray circles), which we consider to be essentially free of any systematic problems. Without any further fitting, the Lorentzian wings reproduce the damping behavior of the two oscillating modes very well, which nicely confirms the overall consistency of our damping analysis.

6.5.2 *Universality on resonance*

On resonance, the *s*-wave scattering length *a* diverges and no longer represents a relevant length scale for the theoretical description of the system. The resulting universal behavior has been widely discussed in the field of ultracold quantum gases. For the microscopic friction coefficient, dimensional analysis reveals a natural unit $\hbar/k$, with the inverse wavenumber $1/k$ representing the relevant length scale. The meaning of k depends on the particular regime.

In the *thermal regime*, the only relevant length scale is represented by the thermal wavenumber $1/k_{th} = \lambda_{th}/\sqrt{2\pi} = \hbar/\sqrt{m_r k_B T}$. For the microscopic friction coefficient on resonance we derive the theoretical prediction

$$\gamma_0 = \frac{8}{3}\sqrt{2\pi}\frac{\hbar}{k_{th}} = \frac{8}{3}\hbar\lambda_{th}\,, \tag{6.18}$$

which for the experimental parameters of Fig. 6.10 yields a unitarity-limited value of $2.4 \times 10^{-40}\,\mathrm{kg}\,m^3\,s^{-1}$. Note that in the thermal regime, γ does not depend on the position and thus $\langle\gamma\rangle = \gamma$.

Our experimental value of γ_0, see Eq. (6.17), lies just 25% below the theoretical prediction of Eq. (6.18) for the thermal regime. We believe that this rather small deviation can be attributed to the onset of Pauli blocking in our moderately degenerate sample, which we have verified by extending the numerical simulation approach of Refs. [109, 110] to mass-imbalanced mixtures.

In the *zero-temperature regime* of a degenerate Fermi gas (Fermi energy E_F), the inverse Fermi wavenumber $1/k_F$ takes the role of the only relevant length scale. Consequently, $\hbar/k_F$ represents the natural unit of the microscopic friction coefficient γ. For the connection between the two limiting regimes, note that $k_{th}/k_F = \sqrt{k_B T/(2E_F)}$.

For the two-species Fermi-Fermi system, we define [25] the local two-species Fermi wavenumber

$$k_{2F} = [3\pi^2(n_1 + n_2)]^{1/3} \tag{6.19}$$

and the corresponding local two-species Fermi energy resp. temperature

$$E_{2F} = k_B T_{2F} = \frac{\hbar^2 k_{2F}^2}{4m_r}\,. \tag{6.20}$$

Note that these definitions contain the ones commonly used for unpolarized spin mixtures, representing the special case of balanced masses and populations.

Using units $\hbar/k_{2F}$ for a general description at all temperatures, we write

$$\gamma_0 = \nu(\tau)\frac{\hbar}{k_{2F}}\,. \tag{6.21}$$

Here we have introduced the dimensionless function $\nu(\tau)$ of the reduced temperature $\tau = T/T_{2F}$ to describe the universal behavior of the microscopic friction effect. For the thermal regime ($\tau \gg 1$), Eq. (6.18) can be put in the simple form

$$\nu = 9.45\,\tau^{-1/2}. \tag{6.22}$$

Let us now interpret our experimental result in relation to the universal function $\nu(\tau)$. Here we have to account for the inhomogeneity of the trapped sample, which makes k_F and indirectly also ν position dependent. By taking the trap average of Eq. (6.21), we obtain

$$\langle \gamma_0 \rangle = \hbar \, \langle \nu/k_{2F} \rangle. \tag{6.23}$$

In a final approximation, we can assume that ν depends only weakly on the local value of τ, which is motivated by the temperatures being too high for a phase transition to a superfluid [25] and by the rather smooth temperature dependence observed in previous experiments in a similar regime [100, 102]. Thus regarding ν as a constant factor, we can take it out of the trap-average integral and derive an effective value

$$\tilde{\nu} = \frac{\langle \gamma_0 \rangle}{\langle 1/k_{2F} \rangle} = 7.8(9), \tag{6.24}$$

which characterizes the situation in our trap with an effective reduced temperature $\tilde{\tau} = T/\langle T_{2F} \rangle \approx 1.5$, where $\langle T_{2F} \rangle = 85\,\text{nK}$ is the trap-averaged Fermi temperature.

The present experimental result is indeed close to the thermal limit as described by Eq. (6.22). It just represents one data point to explore or test the universal function $\nu(\tau)$, but in view of future experiments it serves as an example for a general way to characterize friction in a resonant two-component Fermi gas on a microscopic level.

Regarding previous work, the *macroscopic* effect of friction between two resonantly interacting fermionic clouds has been investigated by groups at MIT [100] and at LENS [102] employing spin mixtures of ^{6}Li. They studied the relative center-of-mass motion and reported measurements of the spin drag rate Γ_{sd}, which according to their definition corresponds to the friction parameter β as defined in our work. For this quantity of interest, $E_F/\hbar$ represents the natural unit (where E_F is the local Fermi energy in the center of the trap [100] or the global Fermi energy characterizing the harmonic trap [102]). The MIT group reported normalized values of $\hbar\Gamma_{sd}/E_F \approx 0.1$ in a temperature range between $T/T_F = 0.3$ and 3, while the measurements at LENS provided somewhat higher values varying from $\hbar\Gamma_{sd}/E_F \approx 0.1$ to 0.4 in a temperature range between $T/T_F = 0.1$ and 0.7.

In our work, the macroscopic drag effect is described by the parameter β, which corresponds to the spin drag coefficient. For a reduced

temperature $T/T_F(0) \approx 1.0$ in the center of the trap, we have measured (data of Fig. 6.9) an on-resonance value of $\beta \approx 5400\,\mathrm{s}^{-1}$, which corresponds to a normalized value of $\hbar\beta/E_F(0) \approx 0.34$. This result lies in the range of the measurements in spin mixtures, which have explored essentially the same interaction regime. However, a more accurate and detailed comparison is hampered by the complications related to the inhomogeneity of the harmonically trapped mixtures. Here, a comparison on the level of the microscopic friction coefficient would be highly desirable.

6.6   CONCLUSIONS AND OUTLOOK

In a comprehensive set of experiments, we have investigated the complete dipole-mode spectrum in a two-species fermionic mixture of ^{161}Dy and ^{40}K, which features mass imbalance and a widely tunable interspecies interaction. While, in the non-interacting case, the two components exhibit individual oscillations with largely different frequencies, dissipative coupling at increasing interaction strength induces damping and finally a crossover into the hydrodynamic regime, leading to a variety of interesting effects. The two oscillating modes exhibit large frequency shifts and, beyond a critical coupling strength in the hydrodynamic regime, one of these modes loses its oscillating character and splits into two purely exponential damping modes.

The most evident signature of hydrodynamics is locking of the individual oscillations to a joint oscillation, in which both species oscillate together with the same frequency. While this effect has been demonstrated in previous work on spin [104], isotopic [116], or species mixtures [90, 105] with uncoupled frequencies lying rather close to each other (difference at most a few 10%), our experiments have been carried out in a more extreme regime with individual frequencies differing by a relatively large factor (frequency ratio of $\sim$3). We have measured the mode frequencies, damping rates along with their relative amplitudes and phases, which fully characterizes the resonance crossover. These results also reveal an effect beyond the mere effect of elastic scattering and resulting friction, demonstrating demonstrating an asymmetry in the damping rate and phase difference, which can be attributed to the reactive mean-field interaction.

Exceeding a critical strength of the interspecies friction, one of the two oscillating modes disappears by splitting into two purely exponential damping modes. The resulting slow damping mode essentially corresponds to the overdamped spatial motion in position space, while the fast mode represents the rapidly damped relative motion in momentum space. We have observed both modes and measured their damping rates in the hydrodynamic crossover. We find that the latter mode is largely insensitive against experimental imperfections, as

unwanted effects such as losses and heating or dynamics related to the shape of the cloud appear on a much longer time scale.

All our observations can be understood in terms of a rather simple model from the literature [104–107], which considers the one-dimensional relative motion of the clouds' mass centers. The interaction coefficients describing the dissipative and reactive coupling can be determined experimentally by fitting the model predictions to the measurements. We found the extracted values to be consistent with theoretical calculations based on collisional dynamics and the mean-field interaction. In this approach, the clouds are considered as rigid mass distributions, which is a benefit of the excellent spatial overlap between the two species in our particular two-species system.

Our interpretation of the observed interspecies friction goes beyond a description of the macroscopic drag effect between the two components, which is complicated by the inhomogeneous trap environment. We have introduced a microscopic friction coefficient as a local quantity and extracted corresponding trap-averaged values from our measurements of mode damping in the strongly interacting regime. We have also shown how the result obtained on resonance, where the scattering length diverges, can be interpreted in terms of universal behavior in the thermal or degenerate Fermi regime. This facilitates a comparison of experiments carried out with a wide range of different two-species systems in the resonantly interacting regime.

In view of future experiments on strongly interacting two-species quantum mixtures, measurements of dipole modes offer a versatile tool-box to investigate phenomena related to hydrodynamic behavior. In particular, the fast damping mode, demonstrated in this work, constitutes a promising new tool for precision experiments related to the fast dissipative dynamics of interspecies friction. It represents an experimental implementation of the general idea [117] to study the response of a mixture to a sudden, species-selective perturbation on a short timescale. This method may even be applied to quantum gases with resonantly interacting bosonic components [68], where the much shorter lifetimes will not permit the observation of oscillation modes.

In ongoing experiments on the Dy-K system, after various improvements of the preparation process, we are now able to produce colder mixtures near the Feshbach resonance [7]. Advancing in near-future work into more deeply degenerate regimes, we can expect substantial manifestations of additional effects beyond collisional hydrodynamics to become observable. With deeper cooling, increased Pauli blocking effects will first reduce the damping rates, before pair correlations and

---

7 As the main problem we identified heating when the deeply degenerate mixture is transferred from the low magnetic field (250 mG), where evaporative cooling is performed, to higher fields near the 7.3 G Feshbach resonance, which is used for the present experiments. This heating is due to a combination of detrimental effects from interspecies [12] and intraspecies [6] Feshbach resonances.

eventually the formation of a superfluid will strongly affect the mode frequencies [118].

In a broader sense, our work on two-species dipole modes generalizes previous work on fermionic spin mixtures [100, 101], which addressed fundamental transport properties in a strongly interacting gas along with their quantum limits. In this context, the microscopic friction coefficient introduced in our work will represent an important building block for understanding the full dynamics in future investigations.

6.7   APPENDIX A: EQUATIONS OF MOTION AND SOLUTION

The two components are treated as rigid masses $M_i = N_i m_i$, where N_i is the atom number of each species and m_i represents the respective atomic mass. The total force on each of the two clouds is a sum of three contributions: (1) The external, species-dependent force exerted by the trap is characterized by the corresponding trap frequencies ω_1 and ω_2, (2) the dissipative friction force is proportional to the relative velocity of both components with the coefficient B, and (3) the reactive force is proportional to the relative displacement, which is assumed to be small compared with the cloud sizes. This force represents the attraction or repulsion between the two components and is quantified by a spring constant K.

The equations of motion for the mass centers of the two components can be written as

$$M_1 \ddot{y}_1 = -M_1 \omega_1^2 y_1 - B(\dot{y}_1 - \dot{y}_2) - K(y_1 - y_2) \qquad (6.25a)$$
$$M_2 \ddot{y}_2 = -M_2 \omega_2^2 y_2 - B(\dot{y}_2 - \dot{y}_1) - K(y_2 - y_1) \qquad (6.25b)$$

In the explicit form, the system of two coupled, second-order linear differential equations reads:

$$\ddot{y}_1 = -\omega_1^2 y_1 - \beta_1(\dot{y}_1 - \dot{y}_2) - \kappa_1(y_1 - y_2) \qquad (6.26a)$$
$$\ddot{y}_2 = -\omega_2^2 y_2 - \beta_2(\dot{y}_2 - \dot{y}_1) - \kappa_2(y_2 - y_1) \qquad (6.26b)$$

where $\beta_i = B/M_i$ and $\kappa_i = K/M_i$.

Expressing the system of equations in matrix form

$$\begin{pmatrix} \dot{y}_1 \\ \dot{y}_2 \\ \ddot{y}_1 \\ \ddot{y}_2 \end{pmatrix} = \begin{pmatrix} 0 & 0 & 1 & 0 \\ 0 & 0 & 0 & 1 \\ -\omega_1^2 - \kappa_1 & \kappa_1 & -\beta_1 & \beta_1 \\ \kappa_2 & -\omega_2^2 - \kappa_2 & \beta_2 & -\beta_2 \end{pmatrix} \begin{pmatrix} y_1 \\ y_2 \\ \dot{y}_1 \\ \dot{y}_2 \end{pmatrix} \qquad (6.27)$$

facilitates a solution by standard numerical routines, which finally yields the complex-valued eigenfrequencies and eigenvectors of the different modes.

For the discussion in the main text, we introduce the reduced total mass $M_r = M_1 M_2/(M_1 + M_2)$ and we define the mass factors $q_1 = M_r/M_1$ and $q_2 = M_r/M_2$. The two parameters

$$\beta \equiv \frac{B}{M_r} = \frac{\beta_1}{q_1} = \frac{\beta_2}{q_2} \tag{6.28}$$

and

$$\kappa \equiv \frac{K}{M_r} = \frac{\kappa_1}{q_1} = \frac{\kappa_2}{q_2} \tag{6.29}$$

then characterize the strength of the dissipative and the reactive interaction between the two clouds.

6.8 APPENDIX B: SPATIAL OVERLAP

Throughout this work, we model the Dy and K clouds as rigid mass distributions with spatial equilibrium shapes corresponding to non-interacting Fermi gases. Figure 6.11(a) shows the number density profiles $n_{Dy}(r)$ and $n_K(r)$ calculated for both species under typical experimental conditions in our harmonic trap. The profiles exhibit near spatial matching and thus a good overlap between both components. The Dy cloud is somewhat larger than the K cloud, but only a small fraction in the outer region does not show any significant overlap with K atoms.

To quantify the spatial overlap between the two components, we define the *overlap density*

$$n_\Omega = \int dV n_{Dy}(\mathbf{r}) \, n_K(\mathbf{r}) \,. \tag{6.30}$$

For spherical symmetry the volume integral simplifies to

$$n_\Omega = 4\pi \int_0^\infty dr \, r^2 \, n_{Dy}(r) \, n_K(r) \,. \tag{6.31}$$

For the interpretation of the overlap density, note that $n_\Omega/N_K = \langle n_{Dy}\rangle_K$ represents the mean density of Dy atoms as 'seen' by the K atoms (and vice versa).

A spatial displacement d between the two clouds reduces the overlap density. In Fig. 6.11(b), we show $n_\Omega(d)$ (solid line) as calculated numerically from Eq. (6.30). For small displacements, a Taylor expansion can be applied:

$$n_\Omega(d) = n_\Omega(0) + \frac{1}{2} d^2 n_\Omega''(0) \,. \tag{6.32}$$

For the conditions of Fig. 6.11, we obtain $n_\Omega = 3.51 \times 10^{22} \, \text{m}^{-3}$ and $n_\Omega''(0) = -2.31 \times 10^{32} \, \text{m}^{-5}$ by numerically evaluating the overlap integrals. The dotted curve in Fig. 6.11(b) illustrates that the second-order
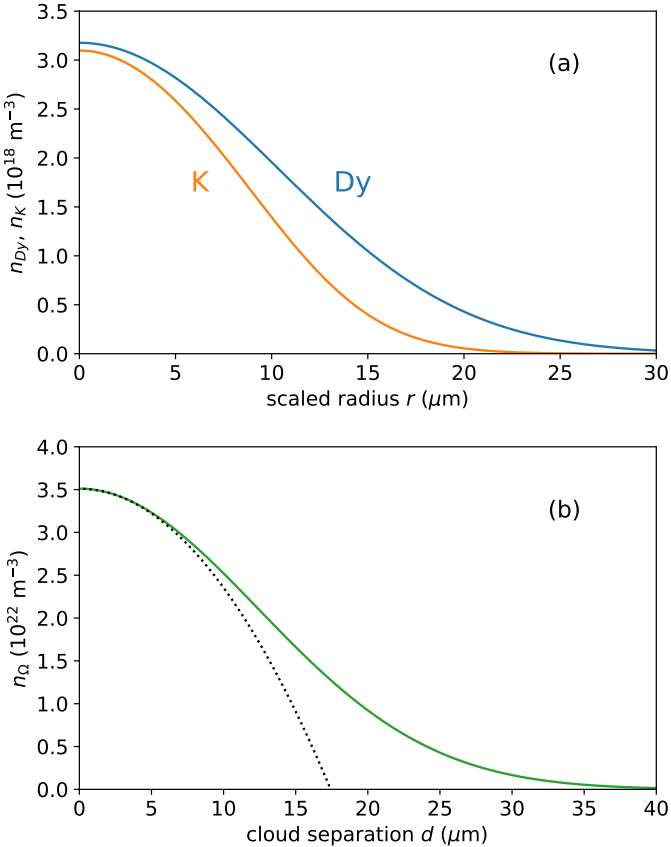
Figure 6.11: Species overlap in the mixture. (a) Spatial profiles for typical experimental conditions $N_{Dy} = 5 \times 10^4$, $N_K = 2 \times 10^4$, $T = 100\,\text{nK}$ in a spherically symmetric trap with mean frequencies $\bar{\omega}_{Dy}/2\pi = 37\,\text{Hz}$ and $\bar{\omega}_K/2\pi = 112\,\text{Hz}$. The reduced temperatures $T_{Dy}/T_F^{Dy} = 0.84$ and $T_K/T_F^K = 0.38$ correspond to moderate Fermi degeneracy. (b) Overlap integral n_Ω as a function of a spatial displacement between the cloud centers (solid line) with a second-order Taylor expansion (dotted line).

expansion remains a good approximation up to displacements of about 10^-m, which corresponds to the linear regime of the reactive force between the two clouds.

We finally have to take into account the anisotropy of our cigar-shaped harmonic trap, which has radial frequencies $\omega_x = \omega_y$ ($2\pi \times$ 59 Hz for Dy, $2\pi \times$ 177 Hz for K), but about four times lower axial frequencies ω_z. We introduce the scaled radius

$$r = \sqrt{(\alpha x)^2 + (\alpha y)^2 + (\alpha^{-2} z^2)} \tag{6.33}$$

with a scaling parameter $\alpha \equiv (\omega_x/\omega_z)^{1/3} \approx 1.6$. Using this definition, the local density approximation allows us to map the situation onto the spherically symmetric case and to apply the above approach. Finally the results can be scaled back to the anisotropic trap. This has no effect on $n_\Omega(0)$, but $n_\Omega''(0)$ has to be multiplied by the factor $\alpha^2 \approx 2.5$. Moreover, the linear regime shrinks by the factor α to displacements less than about 6^-m.

6.9 APPENDIX C: MODELLING THE INTERSPECIES INTERACTION

Here we describe the interaction between the two species in a collisional mean-field model. We introduce the functions $\beta(x)$ and $\kappa(x)$ used in the main text to describe the resonance behavior of the dissipative and reactive interaction between the two species. Within the approximation of rigid mass distributions, we neglect any interaction-induced changes of the cloud profiles.

6.9.1 Dissipative interaction (friction)

We first consider elastic collisions with a fixed s-wave scattering cross section $\sigma = 4\pi a^2$. For the moderate Fermi degeneracy in our experiments, we neglect Pauli blocking effects on the collisions and we assume a mean relative velocity of $\bar{v}_{rel} = \sqrt{8k_B T/(\pi m_r)}$, which corresponds to the thermal limit, where m_r is the individual particle reduced mass. With this assumption, we obtain

$$\Gamma_{coll} = n_\Omega \sigma \bar{v}_{rel} \tag{6.34}$$

for the total elastic collision rate [47]; here n_Ω respresents the overlap density as discussed in Appendix 6.8. Integrating over all collisions in the mixture we obtain the relation to the damping rate for the relative motion of the two species, for which we have introduced the friction parameter

$$\beta = \frac{4}{3} \frac{m_r}{M_r} \Gamma_{coll} . \tag{6.35}$$

We note that this result is in agreement with the model presented in Ref. [104]. We have also verified the relation between β and Γ_{coll}

independently within Monte-Carlo simulations of the damping of the relative interspecies motion.

Combining Eqs. (6.34) and (6.35), we obtain the general relation between the friction coefficient and the scattering cross section,

$$\beta = \frac{4}{3} \frac{m_r}{M_r} n_\Omega \bar{v}_{rel} \times \sigma. \tag{6.36}$$

In the resonance regime, where σ depends on the relative momentum, this equation remains valid, provided that a properly defined effective cross section σ_{eff} is introduced. We note that, staying with this definition, the collision rate Γ_{coll} according to Eq. (6.34) acquires an additional factor of 2, and the prefactor in Eq. (6.35) has to be changed to 2/3. One should also bear in mind that Eqs. (6.34-6.36) have been derived under the assumption of thermal velocity distributions. Deviations remain rather small under our present experimental conditions, but Fermi degeneracy will play a much more important role in future experiments at lower temperatures.

We model the resonance behavior of the cross section based on the imaginary part of the s-wave scattering amplitude, considering the unitarity-limitation imposed by the finite collision momenta. We neglect effective-range corrections to the scattering amplitude and thus momentum-dependent resonance shifts, which is a good approximation for the sufficiently broad Feshbach resonance employed in this work. By integration over all collisional momenta, we obtain an effective cross section, which can be well approximated by a Lorentzian

$$\sigma_{eff} = \frac{4\pi a^2}{1 + a^2/a_c^2}, \tag{6.37}$$

where the length a_c accounts for the finite-momentum limitation. From the theory of resonant scattering in a thermal gas, we can derive the approximation

$$a_c \approx 1.21 \frac{\lambda_{th}}{2\pi}, \tag{6.38}$$

where $\lambda_{th} = \sqrt{2\pi\hbar^2/(m_r k_B T)}$ represents the thermal de Broglie wavelength associated with the relative motion. While Eq. (6.37) reproduces the zero-temperature limit $4\pi a^2$ exactly, we note that within the Lorentzian approximation the on-resonance cross section $4\pi a_c^2 \approx 0.47 \lambda_{th}^2$ turns out to be about 7% lower than the exact result $\lambda_{th}^2/2$. This minor deviation is not relevant for the present experiments.

Combining the above Eqs. (6.34-6.37) and using the dimensionless parameter $x = 1000 a_0/a$, defined in Eq. (6.7) in the main text to characterize the interaction strength across the resonance, we obtain the function

$$\beta(x) = \frac{\beta^*}{x^2 + x_c^2}, \tag{6.39}$$

which describes the resonance behavior of the dissipative interaction (friction) between the two species. For the overall strength of this interaction, the collisional model predicts

$$\beta^* = \frac{16\pi}{3} \frac{m_r}{M_r} n_\Omega \bar{v}_{rel} \times (1000 \, a_0)^2 \,. \tag{6.40}$$

For the conditions of our experiments on the Dy crossover mode reported in Sec. 6.4.2 the relevant parameter values with estimated uncertainties are $m_r/M_r = 3.7(4) \times 10^{-5}$, $n_\Omega = 4.8(5) \times 10^{22} \, \mathrm{m}^{-3}$, and $\bar{v}_{rel} = 8.1(8) \, \mathrm{mm/s}$. This results in a parameter value of $\beta^* = 680(120) \, \mathrm{s}^{-1}$, where the rather large uncertainty of nearly 20% reflects our limited knowledge of the experimental conditions.

6.9.2 *Reactive interaction (mean field)*

The total potential energy resulting from the mean-field interaction between both species is given by the general expression

$$U_{\mathrm{m}f} = g \, n_\Omega \,, \tag{6.41}$$

where $g = (2\pi\hbar^2 a)/m_r$ represents the coupling constant. With the overlap density according to Eq. (6.32), which describes the effect of small displacements between the two clouds, we obtain

$$U_{\mathrm{m}f}(d) = U_{\mathrm{m}f}(0) + \frac{1}{2} g \, \alpha^2 n_\Omega''(0) \, d^2 \,. \tag{6.42}$$

The second term ($\propto d^2$) quantifies the reactive effect in a harmonic approximation, with $g \, \alpha^2 n_\Omega''(0)$ representing the spring constant. The latter corresponds to the coefficient $K = M_r \kappa$ in Eq. (6.25). We thus obtain

$$\kappa = \frac{g \, \alpha^2}{M_r} n_\Omega''(0) \tag{6.43}$$

which is positive for attractive interaction.

To model the unitarity-limited resonance behavior in a way analogous to Eq. (6.37), we introduce the effective coupling constant

$$g_{eff} = \frac{2\pi\hbar^2}{m_r} \frac{a}{1 + a^2/a_c^2} \,, \tag{6.44}$$

which results from real part of the s-wave scattering amplitude in the resonance regime.

Combining the above Eqs. (6.43 and 6.44) and again characterizing the interaction by the parameter $x = 1000 \, a_0/a$, we obtain the function

$$\kappa(x) = -\frac{\kappa^* x}{x^2 + x_c^2} \,, \tag{6.45}$$

where

$$\kappa^* = -\frac{2\pi\hbar^2\alpha^2 n_\Omega''}{M_r m_r} \times 1000\, a_0 \,. \tag{6.46}$$

For the experimental conditions of the experiments described in Sec. 6.4.2, $M_r = 8.7(9) \times 10^4\,$u, $\alpha^2 = 2.6(3)$, and $n_\Omega''(0) = -3.1(3) \times 10^{32}\,$m^{-5}, we finally obtain the parameter value $\kappa^* = 3.8(7) \times 10^4\,$s^{-2}. Regarding the uncertainty we note that a substantial additional uncertainty may arise from an interaction-induced deformation of the clouds, which we have neglected in our simple model and which presumably can have a large effect on the derivative n_Ω''.

7

ADDITIONAL MEASUREMENTS ON THE DY-K FESHBACH SPECTRUM

x

x

Part III

MAKING, PROBING, AND UNDERSTANDING
DyK FESHBACH MOLECULES

8

FESHBACH MOLECULES AS DOOR TO THE BEC-BCS CROSSOVER

compare with Li and K *here? or only in the real intro?*

Stability concerns and new, unexpected instabilities discovered

PUBLICATION: OPTICALLY TRAPPED FESHBACH MOLECULES OF FERMIONIC ^{161}Dy AND ^{40}K

Published as Editor's Suggestion:

Elisa Soave, Alberto Canali, Zhu-Xiong Ye, Marian Kreyer, Emil Kirilov, and Rudolf Grimm.

Author contribution: The author took a supporting role in the process of acquiring and analyzing the data described in this publication as well as writing the manuscript.

We report on the preparation of a pure ultracold sample of bosonic DyK Feshbach molecules, which are composed of the fermionic isotopes ^{161}Dy and ^{40}K. Employing a magnetic sweep across a resonance located near 7.3 G, we produce up to 5000 molecules at a temperature of about 50 nK. For purification from the remaining atoms, we apply a Stern-Gerlach technique based on magnetic levitation of the molecules in a very weak optical dipole trap. With the trapped molecules we finally reach a high phase-space density of about 0.1. We measure the magnetic field dependence of the molecular binding energy and the magnetic moment, refining our knowledge of the resonance parameters. We also demonstrate a peculiar anisotropic expansion effect observed when the molecules are released from the trap and expand freely in the magnetic levitation field. Moreover, we identify an important lifetime limitation that is imposed by the 1064-nm infrared trap light itself and not by inelastic collisions. The light-induced decay rate is found to be proportional to the trap light intensity and the closed-channel fraction of the Feshbach molecule. These observations suggest a one-photon coupling to electronically excited states to limit the lifetime and point to the prospect of loss suppression by optimizing the wavelength of the trapping light. Our results represent important insights and experimental steps on the way to achieve quantum-degenerate samples of DyK molecules and novel superfluids based on mass-imbalanced fermion mixtures.

9.1   INTRODUCTION

Over the past twenty years, the formation of molecules via magnetically tuned Feshbach resonances [17, 119] has been established as a powerful tool for experiments on ultracold quantum gases, which allows for coupling of the atomic to the much richer molecular world. Early experiments on Bose-Einstein condensates (BECs) have demonstrated atom-molecule coupling [120, 121] and the production of molecular samples near quantum degeneracy [65, 122, 123]. In ultracold Fermi gases, molecule formation [64, 124–126] plays a particular role because of the inherent change of the quantum statistics when pairs of fermions form composite bosons. This has led to the observation of molecular BEC [127–129], the demonstration of fermionic condensation [130] and superfluidity [131] and a great wealth of experiments on the crossover in strongly interacting Fermi gases from BEC to Bardeen-Cooper-Schrieffer (BCS) type pairing [19, 20].

In heteronuclear molecular systems, which in the laboratory can be realized with various two-species atomic mixtures [66, 132–139], the interest in Feshbach resonances has been to large extent driven

by the possibility to create polar molecules featuring strong electric dipole-dipole interactions. For mixtures of two fermionic species [2, 5, 29–34, 36, 37], however, another promising application is stimulating the interest in Feshbach resonances and molecules. Theoretical work has predicted fermionic quantum-gas mixtures with mass imbalance to favor exotic interaction regimes [22]. Mass-imbalanced systems hold particular promise in view of superfluid states with unconventional pairing mechanisms [23–25], most notably the elusive Fulde-Ferrell-Larkin-Ovchinnikov (FFLO) state [26–28]. In addition to the exciting prospects in many-body physics, a variety of interesting few-body phenomena have been predicted to emerge in resonant fermion mixtures [70, 76].

Our system is an ultracold Fermi-Fermi mixture of ^{161}Dy and ^{40}K atoms [2], which features a great variety of interspecies Feshbach resonances at high and low magnetic fields [5, 12]. In our recent work [12], we have identified a particularly interesting resonance in the low-field region near 7 G, which is isolated from other resonances and strong enough to facilitate accurate magnetic interaction tuning in combination with a significant universal range. We have also demonstrated the formation of Feshbach molecules by a magnetic sweep across the resonance.

In the present article, we report on the optical trapping of our DyK Feshbach molecules. In Sec. 9.2 we show how the molecular cloud is purified by a magnetic levitation technique, where the molecules are kept in the shallow optical dipole trap while the atoms are pulled out of it. In Sec. 9.3 we present a state-of-the-art characterization of the Feshbach resonance, based on the measurement of molecular binding energies and of the molecular magnetic moment. In Sec. 9.4 we discuss an anisotropic expansion effect that is observed when the cloud is released close to the resonance in the presence of the magnetic levitation field. In Sec. 9.5 we study the lifetime of the trapped molecular cloud and identify a light-induced one-body mechanism (and not inelastic collisions) as the main limiting factor. In Sec. 9.6 we summarize the main conclusions of our work and point to future prospects.

9.2 PREPARATION OF PURE MOLECULAR SAMPLES

In this section we present the main steps to produce a pure sample of trapped DyK Feshbach molecules. The molecules are associated using the resonance near 7G that we have identified in our recent work [12]. In Sec. 9.2.1 we briefly summarize how a double-degenerate sample of Dy and K is obtained and how it is transferred into the 7-G magnetic field region. In Sec. 9.2.2 we present the experimental procedure that results in the formation of a pure molecular sample. The purification is based on a Stern-Gerlach (SG) separation of the molecular cloud, held in a weak optical dipole trap (ODT), from the atomic clouds,

which are pulled out of the trap. As discussed in detail in Sec. 9.2.3, this procedure allows us to obtain a sample of about 5×10^3 DyK molecules at a temperature of about 50 nK. We reach a phase-space density (PSD) of about 0.14, only one order of magnitude away from degeneracy.

9.2.1 *Preparation of the mixture and transfer into the 7-G magnetic field region*

The starting point of every experimental cycle is the production of a degenerate sample of Dy and K at 250 mG in a near-infrared (1064 nm) ODT. Both species are spin polarized in their lowest hyperfine sublevels $|F, m_F\rangle = |21/2, -21/2\rangle$ and $|9/2, -9/2\rangle$, respectively. Following the procedures already presented in Refs. [2] and [12], we are able to reach the deeply degenerate regime with reduced temperatures $T_{Dy}/T_F^{Dy} \approx 0.13$ and $T_K/T_F^K \approx 0.13$, normalized to the respective Fermi temperatures. The sample is then transferred into a 1064 nm crossed ODT formed by a horizontal beam, with a waist of 100 μm (Azurlight ALS-IR-1064-5- I-CC-SF) and a vertical beam, waist of 65 μm (Mephisto MOPA 18 NE). A magnetic field gradient of 2.2 G/cm supports the trapping of Dy, without fully canceling the differential gravitational sag with respect to K. This guarantees that the two clouds are kept spatially separated throughout the subsequent phase, during which the magnetic field is ramped within 2 ms to $B = 7.775$ G, corresponding to a 500 mG detuning above resonance.

To address specific magnetic field strengths in the 7-G region, we employ a set of coils (offset coils) that provide a fixed stable offset, which remains unchanged for the rest of the sequence. These coils were originally designed to produce high magnetic fields of a few hundred gauss [5] and respond rather slowly to magnetic field changes. Therefore, the magnetic field ramps required for the rest of the sequence are performed employing an additional set of coils (fast coils), whose magnetic field adds to the constant field provided by the offset coils. Further details on the way we control the magnetic field during the experimental sequence are reported in App. 9.7.

9.2.2 *Molecule association and Stern-Gerlach purification*

Figure 9.1 schematically illustrates the part of the experimental sequence that takes place in the 7-G region. At the end of the transfer into the 7-G region, the two clouds are kept spatially separate for about 50 ms to let the field fully stabilize. The experimental sequence then proceeds in four further steps: (1) spatially overlapping the two clouds, (2) magnetic association of molecules, (3) SG purification of the molecular sample, and (4) adiabatic transfer to the desired target field and preparation for final experiments. The molecular state adiabati-
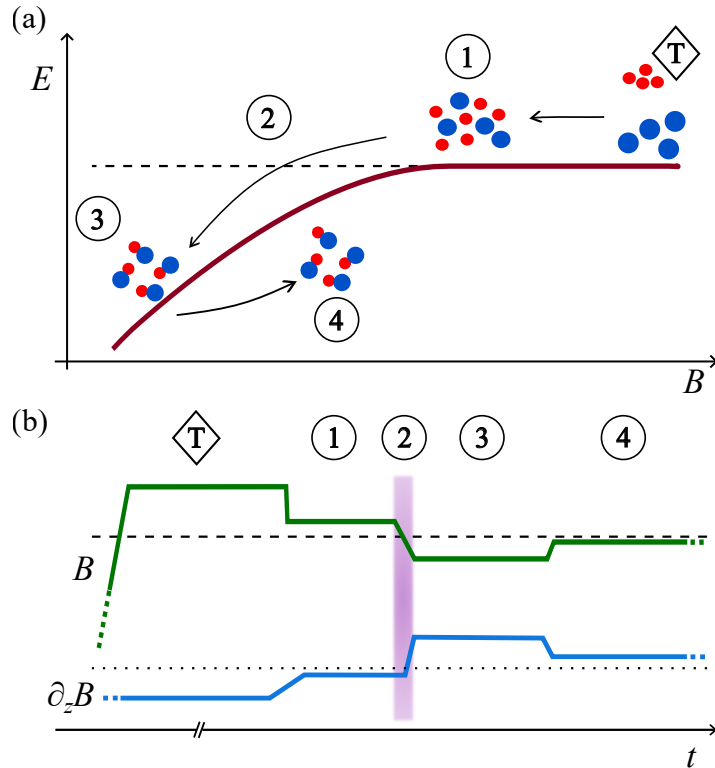
Figure 9.1: Procedure to prepare a pure sample of Feshbach molecules by magnetic field ramping. (a) Qualitative representation of the steps of the association process and the SG purification in relation to the magnetic field and the energy state of free atoms and molecules. The dashed line refers to the unbound atomic pair below resonance. (b) Qualitative representation of the corresponding ramping scheme for the magnetic field (green) and magnetic field gradient (blue); see main text for details. The dashed line represents the resonance pole position and the dotted line represents the magnetic field gradient that levitates dysprosium. After the transfer of the sample into the 7-G region (T, diamond symbol), the sequence proceeds with four main steps: 1) overlap of the two clouds; 2) magnetic field association of molecules (pink shaded region); 3) SG purification of the sample; 4) transfer to the desired magnetic field.

cally follows the changes in magnetic field. In order to account for the changes in the molecular magnetic moment, the magnetic field ramps performed in the steps (1) to (4) are accompanied by corresponding magnetic field gradient ramps, this ensures that the molecular sample experiences the same magnetic force.

We now discuss the four stages in more detail.

Stage (1): We apply a 12-ms ramp of the magnetic field gradient from its initial value to the one that cancels the differential gravitational sag between Dy and K so that the two clouds overlap. In the following this is referred to as "magic levitation" [46], realized at $\partial_z B = 2.69 \, \text{G/cm}$. Simultaneously with the gradient ramp, the trapping frequencies are reduced from $\bar{\omega}_{\text{Dy}} = 2\pi \times 50 \, \text{Hz}$ to about $2\pi \times 35 \, \text{Hz}$, where $\bar{\omega}$ is the geometrically averaged trap frequency ($\omega_K \approx 3.6 \, \omega_{\text{Dy}}$ [3]). Halfway during the ramp, the magnetic field is decreased within 1 ms to 7.325 G, about 50 mG above the resonance center.

Stage (2): By magnetic field association [17, 119] we create about 6×10^3 DyK molecules, corresponding to almost 30% conversion efficiency. We found the optimal ramp speed to be $\dot{B} = 0.43 \, \text{G/ms}$, which is in the range of typical experiments using Feshbach resonances of similar widths [17]. The 0.4-ms ramp ends at a magnetic detuning of about $-120 \, \text{mG}$, which corresponds to a molecular binding energy of $h \times 220 \, \text{kHz}$. We identify such a magnetic field as optimal for the purification of the molecular sample in the subsequent stage (3). The second half of the magnetic field sweep are accompanied by an increase of the magnetic field gradient from the magic levitation value to the one required to balance the gravitational force on the molecules at this detuning. For the sake of notation simplicity, we introduce the molecular levitation gradient $B'_{\text{mol}} = m_{\text{mol}} g / \mu_{\text{mol}}$, where m_{mol} is the molecular mass, g is the gravitational acceleration and μ_{mol} is the molecular magnetic moment. Note that μ_{mol} and thus B'_{mol} are B-dependent quantities. At the end of the magnetic field sweep, the sample consists of a three-component mixture made of DyK molecules and unbound Dy and K atoms.

Stage (3): We proceed with the purification of the molecular sample. The depth of the ODT is decreased to about $U_{\text{DyK}} = k_B \times 220 \, \text{nK}$, so that only the molecules, perfectly levitated at B'_{mol}, are kept in the trap. This naturally leads to a SG separation of the three components. Figure 9.2 demonstrates the SG separation process, showing a series of absorption images of the three clouds, taken at different hold times. The end of the magnetic field association sweep corresponds to $t = 0$. The molecular cloud remains at the same vertical position ($z = 0$) and does not expand, confirming that the molecules are indeed kept in the trap. Dy and K are instead accelerated vertically, being over- and under-levitated, respectively. In the figure the motion appears as a parabolic trajectory with positive (Dy) and negative (K) curvature. The magnetic field for the purification is chosen in order to maximize the
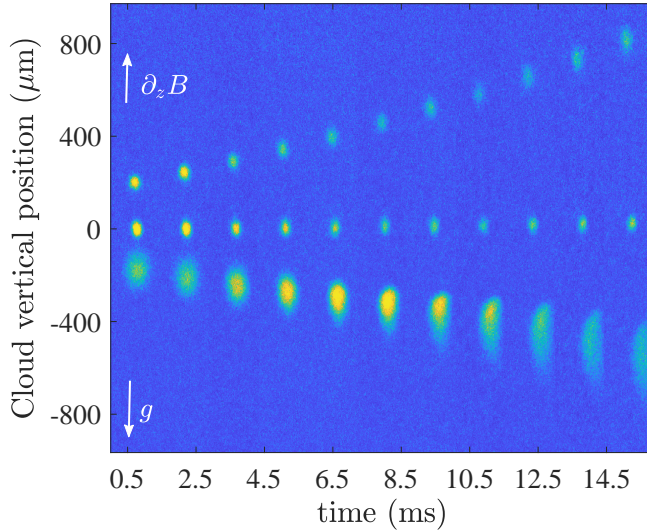
Figure 9.2: Demonstration of SG purification. After magnetic association, the molecules are held in an very shallow trap, at $B = 7.170\,\text{G}$. The magnetic field gradient is set to cancel the gravitational force experienced by the molecules, which therefore are kept in the ODT (central cloud, held at a fixed position $z = 0$). Dysprosium (at cloud positions $z > 0$) and potassium (at cloud positions $z < 0$) undergo a vertical acceleration. Each image is the average of four absorption pictures, taken after a variable hold time (plus a fixed expansion time of $4\,\text{ms}$). The molecular signal corresponds to the dissociated potassium component of the molecular cloud, and has been imaged together with the pure K atoms. The absorption pictures taken of K and Dy have been superposed for presentation purposes.

difference in accelerations between the three clouds (Sec. 9.3.3), while minimizing molecular losses (Sec. 9.5). After $4\,\text{ms}$ the atomic clouds are far enough from the ODT that they can no longer be recaptured. At this point we are left with a pure molecular sample. We note that a similar purification scheme, based on magnetic levitation and SG separation, was demonstrated for optically trapped RbCs Feshbach molecules in Ref. [137].

Stage (4): The magnetic field strength B is finally ramped to its target value within typically $0.5\,\text{ms}$, and the magnetic field gradient is varied accordingly to follow B'_{mol}. The trapping conditions (trap frequencies, depth, geometry) are modified depending on the specific measurement we want to perform with the pure sample of DyK Feshbach molecules in the last stage of the experimental cycle.

At the end of the sequence, the ODT is switched off. The molecular cloud is let to expand keeping the magnetic field and magnetic field gradient fixed. One ms before the imaging pulse, the magnetic field is ramped to positive detunings of the resonance and the molecules are dissociated. The main information about the molecules is obtained
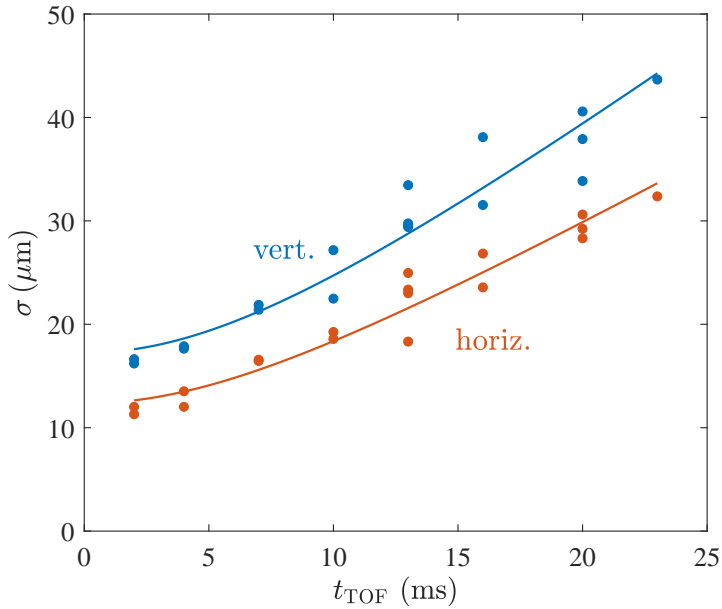
Figure 9.3: Vertical and horizontal size of the molecular cloud as a function of the time of flight t_{TOF}. The sample is let expand at $B = 7.22\,\text{G}$, upon switching off the magnetic levitation together with the ODT. A fit to the data, assuming a ballistic expansion, yields a vertical and horizontal temperature of $77(6)$ and $45(3)\,\text{nK}$, respectively.

from the absorption picture of the dissociated potassium component of the molecular cloud. We can also image the molecules without dissociating them, while keeping the magnetic field fixed. This possibility has the advantage of not altering the expansion of the molecules in time of flight, but the efficiency of the absorption imaging depends on the magnetic field detuning as for more deeply bounded molecular state (large negative B field detunings) only a fraction of the total molecule number can be imaged.

9.2.3 *Temperature and phase-space density*

The experimental scheme described above provides us with a pure molecular sample of about $N_{\text{mol}} = 5 \times 10^3$ molecules, at a temperature of few tens of nK. We derive the temperature of the molecular cloud from a time-of-flight expansion (Fig. 9.3 [1]). In this specific set of experiments, the molecules are not dissociated to avoid extra energy from the dissociation, but imaged directly [140]. A fit to the data reported in Fig. 9.3 yields a horizontal and a vertical temperature of $45(3)\,\text{nK}$ and $77(6)\,\text{nK}$, respectively. We attribute the difference in these results to additional excitations caused by the rapid changes of vertical magnetic forces during the ramping process. We indeed observe uncontrolled

---

1 See the **Supplemental Material** for the data files of all figures

vertical collective oscillations affecting the expansion, which can result in increased temperatures if measured vertically. The horizontal behavior is free of such effects and the expansion can be fully attributed to the temperature of the sample.

We are able to directly measure the trap frequencies of the molecules by observing the center of mass oscillations. Assuming typical trapping conditions ($\bar{\omega} = 2\pi \times 28\,\text{Hz}$), we calculate a phase-space density $\text{PSD} = N_{\text{mol}}(\hbar\bar{\omega}/k_B T_{\text{mol}})^3 \approx 0.14$, about one order of magnitude away from degeneracy. The conditions near quantum degeneracy represent an excellent starting point for further experiments. Comparable values of the PSD have been reached recently in a system of NaCs Bose-Bose Feshbach molecules [66]. While BEC has not yet been reached with bosonic heteronuclear Feshbach samples, quantum degenracy has been obtained in fermionic heteronuclear systems of KRb[141] and NaK [142].

9.3 BINDING ENERGY, MAGNETIC MOMENT, AND RESONANCE PARAMETERS

In this section, we provide a further characterization of the Feshbach resonance near 7 G, already introduced in our previous work [12]. We first, in Sec. 9.3.1, introduce the definitions of the relevant parameters and some basic relations. We then, in Secs. 9.3.2 and 9.3.3, report on two independent sets of experiments, based on measurements of the magnetic-field dependent molecular binding energy and the magnetic moment, which further confirm and refine the values of the key parameters describing the resonance. In Sec. 9.3.4, we summarize our results.

9.3.1 *Basic definitions and relations*

Close to the center of a single isolated *s*-wave Feshbach resonance, the scattering length *a* is large and can be approximated by

$$a = -\frac{A}{\delta B}a_0, \tag{9.1}$$

where A is a parameter characterizing the resonance strength, $\delta B = B - B_0$ is the magnetic detuning from the resonance center B_0, and a_0 denotes the Bohr radius. For a narrow Feshbach resonance [17], a proper characterization of the system also requires the knowledge of a third parameter, such as the difference in magnetic moments of the open channel (atom pair) and closed channel (uncoupled molecular state), which we define as $\delta\mu = \mu_{\text{open}} - \mu_{\text{closed}}$. For describing narrow Feshbach resonances it is convenient to introduce a characteristic length scale, the range parameter $R^* = \hbar^2/(2m_r a_0 \delta\mu A)$, with m_r being the reduced mass of the atom pair [43]. The condition $a \gtrsim R^*$ characterizes the crossover into the universal regime, where the two-, few- and

many-body interaction physics acquires universal properties [17, 143, 144]. For convenience, we introduce a corresponding magnetic-field scale δB^*, defined as the negative detuning where $a(-\delta B^*) = 4R^*$. In terms of the resonance parameters A and $\delta\mu$, this corresponds to

$$\delta B^* = m_r \, \delta\mu \, a_0^2 \, A^2 / (2\hbar^2). \tag{9.2}$$

In our case, a negative detuning gives a positive scattering length and corresponds to the magnetic field region where the pair can bind into a molecule. Knowing $B_0, \delta B^*$ and $\delta\mu$, the energy of the molecular state relative to the atomic pair state (negative binding energy) can be calculated as [43, 44]

$$E_{\mathrm{mol}} = -\delta\mu \, \delta B^* \left(\sqrt{1 - \frac{\delta B}{\delta B^*}} - 1 \right)^2. \tag{9.3}$$

The differential magnetic moment of the molecules is related to the binding energy via the differential relation

$$\delta\mu_{\mathrm{mol}} = \partial E_{\mathrm{mol}} / \partial B = \delta\mu \left(1 - \frac{1}{\sqrt{1 - \frac{\delta B}{\delta B^*}}} \right). \tag{9.4}$$

In the following two subsections, we report on measurements of the magnetic-field dependence of the molecular binding energy and the differential magnetic moment.

9.3.2 Binding energy spectroscopy

A common method to determine the resonance parameters is based on measuring the molecular binding energy as a function of the magnetic field by magnetic-field (wiggle) modulation spectroscopy [53, 121, 145].

The mixture is prepared at low magnetic-field strength and transferred in the 7-G region, as described in Sec. 9.2.1. By means of the fast coils, the field is then quickly ramped to the target field below the resonance center. We finally superpose the two clouds, ramping the magnetic field gradient to reach magic levitation conditions. At this point, our sample consists of $N_K = 1.5 \times 10^4$ atoms of potassium and $N_{\mathrm{Dy}} = 7 \times 10^4$ atoms of dysprosium at a temperature of about $160\,\mathrm{nK}$ (for this measurement we do not perform full evaporation). We associate the molecules by a sinusoidal modulation of the magnetic field around the bias field. The modulated field is produced by a coil with four loops, which is placed on the top viewport, tilted with respect to the magnetic field, and driven by a radio-frequency (RF) signal generator. Taking into account the relative kinetic energy E_{kin} of the thermal motion of an atom pair, the association of a dimer happens when the resonance condition $hf_{\mathrm{mod}} = -E_{\mathrm{mol}} + E_{\mathrm{kin}}$ is fulfilled [133, 146, 147],
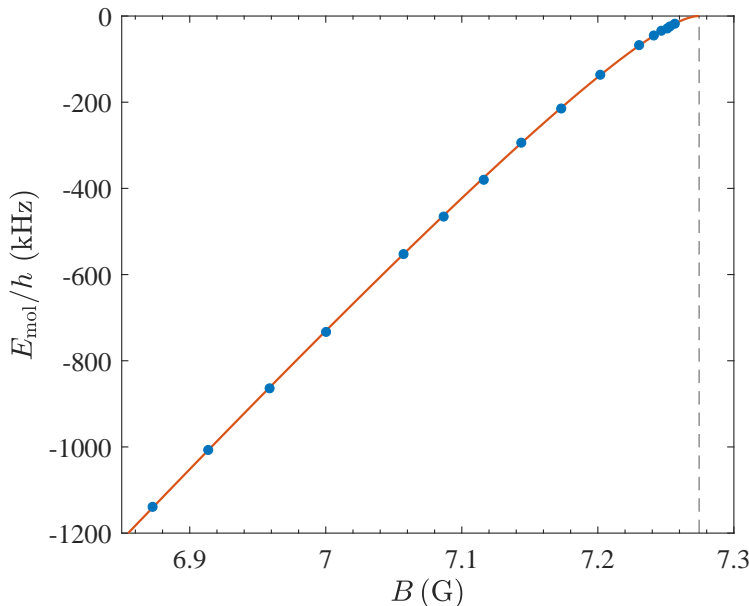
Figure 9.4: Molecular state energy as a function of the magnetic field, measured via modulation of the magnetic field (wiggle spectroscopy). The experimental data have been corrected by the small thermal shift of $\sim 5\,\text{kHz}$. Uncertainties are smaller than the symbol size. The solid line is a fit to the data according to Eq. (10.2). The dashed line indicates the position of the resonance pole.

and manifests itself in atomic loss. With a cloud temperature T of about $150\,\text{nK}$, the average relative kinetic energy of the pairs translates into a small thermal frequency shift $(3/2)k_B T/h$ of about $5\,\text{kHz}$. The strength and the duration of the modulation are adjusted in order to optimize the signal, the width and amplitude of which depend on the measurement. A Gaussian fit to the loss features yields widths (2 standard deviations) of 10 to $20\,\text{kHz}$ and amplitudes ranging from 30 to 100% of the atom number of the minority component (potassium). In Fig. 9.4 we plot the binding energies measured as a function of the magnetic field. The data are fitted with Eq. (10.2). The fit results for the resonance parameters B_0, δB^* and $\delta\mu$ are reported in Table 9.1 and discussed in Sec. 9.3.4.

As for all the other measurements reported in this article, the magnetic field is calibrated performing RF spectroscopy on the atomic K transition $|F, m_f\rangle = |\frac{9}{2}, -\frac{9}{2}\rangle \to |\frac{9}{2}, -\frac{7}{2}\rangle$. The signal is fitted with a Lorentzian function and the uncertainty typically amounts to about $1.5\,\text{mG}$, as described in Ref. [12].

9.3.3 Magnetic moment spectroscopy

Applying an alternative method, we determine the resonance parameters by magnetic moment spectroscopy [65, 148]. The molecules are
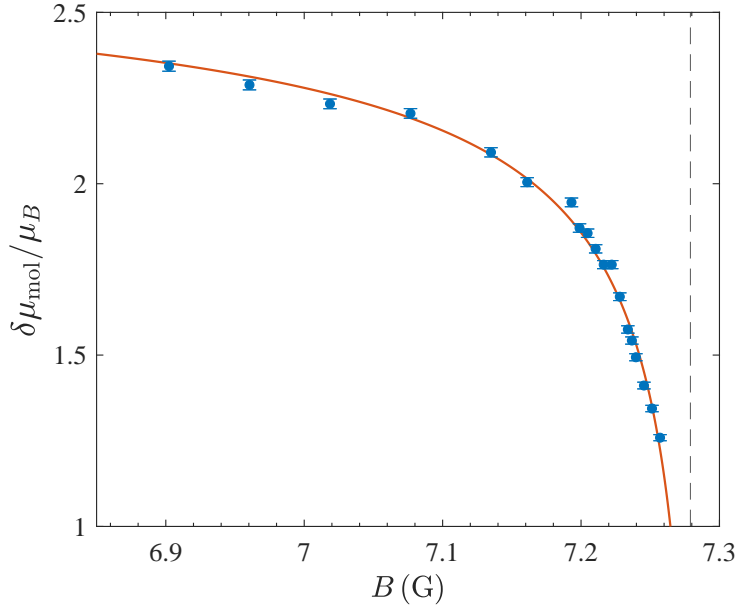
Figure 9.5: Differential magnetic moment of the molecules as a function of the magnetic field. The magnetic moment is measured by determining the perfect magnetic field gradient that balances the gravitational force at the given magnetic field. The solid line is a fit to the data according to Eq. (9.4). The dashed line indicates the position of the resonance pole.

prepared as described in Sec. 9.2. After the SG purification phase, we ramp the magnetic field to the target field. The magnetic field gradient is ramped accordingly to always allow the molecules to stay in the trap. At the target field we hold the molecules for 4 ms and then switch off the ODT. Both the magnetic field and the magnetic field gradient remain unchanged. We observe the vertical position of the molecular cloud during the expansion and determine the magnetic field gradient that perfectly compensates the gravitational force. The magnetic field gradient is calibrated performing corresponding measurements on Dy alone, the magnetic moment of which is well known ($\mu_{Dy} = 10\mu_B$, where μ_B is the Bohr magneton). In Fig. 9.5 we plot the differential molecular magnetic moment $\delta\mu_{mol}$ as a function of the magnetic field strength, the magnetic moment μ_K of potassium being $1\mu_B$. We fit the experimental data with Eq. (9.4). The parameter values derived from the fit are reported in Table 9.1.

We point out that magnetic moment spectroscopy is a practical and powerful tool. It does not only provide us with an alternative way to determine the Feshbach resonance parameters, but also gives a direct measurement of the closed-channel fraction [17, 149]

$$Z(B) = \delta\mu_{mol}(B)/\delta\mu. \tag{9.5}$$

We note that magnetic moment spectroscopy offers a great practical advantage. Knowing the resonance parameters δB^* and $\delta\mu$, a single measurement of the magnetic gradient that balances gravity directly provides the magnetic detuning δB and thus also the scattering length close to resonance.

9.3.4 *Summary of the 7-G resonance parameters*

The values of the Feshbach resonance parameters $\delta B^*, \delta\mu$ and B_0 obtained from the binding energy spectroscopy and the magnetic moment spectroscopy are reported in Table 9.1. The two methods give consistent results. We also present combined values for the three parameters, which represent our best knowledge.

The resonance center position derived in the present work is 20 mG lower than the value of $B_0 = 7.295(1)$ G reported in our previous work [12]. We attribute the discrepancy between the two values to small uncontrolled magnetic field deviations affecting the previous measurements. The experiments reported in the present work have been conducted under improved magnetic field control. In particular, the combination of the fast coils and the digital proportional-integral-derivative (PID) controller leads to a faster stabilization of the magnetic field around the desired set point, minimizing uncontrolled departures of the magnetic field from the target value. Our present results for the parameter values of δB^* and $\delta\mu$ are consistent with the previous results within one and two standard errors, respectively.

For the two parameters R^* and A, which can be calculated from δB^* and $\delta\mu$, we obtain the updated values $R^* = 604(20)a_0$ and $A = 24.0(6)$ G.

9.4 MAGNETIC ANTITRAPPING IN LEVITATION FIELD

The magnetic field dependence of the molecular magnetic moment translates, in the presence of a magnetic field gradient, into a position-dependent force. For perfect levitation with a constant magnetic gradient along the vertical axis, this force balances gravity in the trap center, while it pushes up the molecules above the center and pulls down

Table 9.1: Summary of the parameter values determined for the 7-G Feshbach resonance.

	δB^* (mG)	$\delta\mu / \mu_B$	B_0 (G)
Binding energy spectroscopy	9.8(7)	2.77(3)	7.274(1)
Magnetic moment spectroscopy	10.2(1.2)	2.81(5)	7.279(2)
Combined	9.9(6)	2.78(2)	7.276(2)
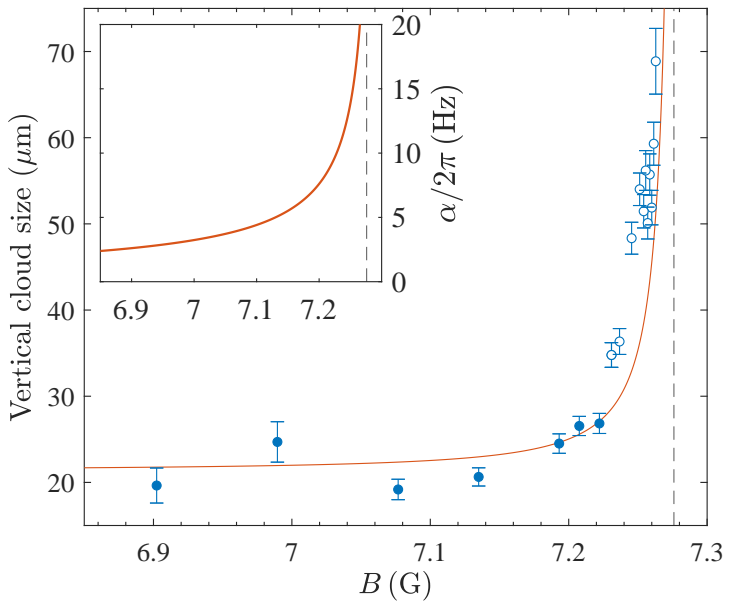
Figure 9.6: Measured vertical size of the levitated molecular cloud after 20 ms expansion as a function of the magnetic field. The error bars show the sample standard deviation of four individual measurements at the same magnetic field. The solid line is a fit to the data at the large detunings (filled circles) according to Eq. (9.10). The inset shows the antitrapping frequency $\alpha/2\pi$ calculated according to Eq. (9.9). For both plots the dashed line indicates the position of the pole of the resonance.

the ones below the center. In first order of the vertical position z with respect to the trap center, this anti-trapping force can be expressed as

$$F(z) = (\partial_z \mu_{\mathrm{mol}})(\partial_z B)\, z \,, \tag{9.6}$$

where $\mu_{\mathrm{mol}} = \mu_{\mathrm{Dy}} + \mu_{\mathrm{K}} - \delta\mu_{\mathrm{mol}}$ is the total molecular magnetic moment. With $\partial_z \mu_{mol} = (\partial_B \mu_{mol})(\partial_z B)$ and $\partial_B \mu_{mol} = -\partial_B^2 E_{mol}$ the force can be rewritten in terms of the second derivative of the binding energy:

$$F(z) = -(\partial_z^2 E_{\mathrm{mol}})(\partial_z B)^2\, z \,. \tag{9.7}$$

Interpreting the positive factor $-(\partial_z^2 E_{\mathrm{mol}})(\partial_z B)^2$ as a negative spring constant, we now define the "anti-trapping frequency"

$$\alpha = \sqrt{-m_{\mathrm{mol}}^{-1}\, \partial_z^2 E_{mol}}\; \partial_z B \,, \tag{9.8}$$

where $m_{\mathrm{mol}} = m_{\mathrm{Dy}} + m_{\mathrm{K}}$ is the molecular mass. Combining with Eq. 10.2) and applying some straightforward algebra, we finally obtain

$$\alpha = \sqrt{\frac{\delta\mu}{2m_{\mathrm{mol}}\delta B^*}}\, \frac{\partial_z B}{\left(1 - \frac{\delta B}{\delta B^*}\right)^{3/4}}. \tag{9.9}$$

In the resonance limit $\delta B \to 0$, where the levitation gradient takes the value $\partial_z B = m_{\mathrm{mol}} g / (\mu_{\mathrm{Dy}} + \mu_{\mathrm{K}}) = 3.21\,\mathrm{G/cm}$, the anti-trapping frequency approaches its maximum $\alpha_{max} = g\sqrt{\delta\mu\, m_{\mathrm{mol}}/(2\delta B^*)}/(\mu_{\mathrm{Dy}} + \mu_{\mathrm{K}}) = 2\pi \times 31.8(8)\,\mathrm{Hz}$. The calculated anti-trapping frequency is shown in the inset of Fig. 9.6: The closer to resonance, the stronger is the antitrapping force. At detunings larger than about $50\,\mathrm{mG}$, α decreases to few Hz, with negligible effects both on the expansion dynamics and the trapping potential.

The magnetic anti-trapping effect can have considerable impact on molecules in the ODT. The vertical trap frequency is reduced from its bare value ω_z to an effective value $\sqrt{\omega_z^2 - \alpha^2}$. Moreover, with the harmonic anti-trap competing with the Gaussian potential of the ODT, the overall depth of the trapping potential can be substantially reduced. When the ODT is switched off, the antitrapping force modifies the ballistic expansion, causing a vertical stretching of the cloud. After release, the particle motion along the vertical direction is described in terms of hyperbolic functions [45, 65]. Assuming a Gaussian distribution of the position and velocity of the molecular sample, the vertical rms size of the cloud is expected to expand as

$$\sigma_z = \sqrt{\frac{k_B T}{m_{\mathrm{mol}}}} \sqrt{\frac{\cosh^2(\alpha t_{\mathrm{TOF}})}{\omega_z^2 - \alpha^2} + \frac{\sinh^2(\alpha t_{\mathrm{TOF}})}{\alpha^2}}, \tag{9.10}$$

where T is the temperature of the sample and t_{TOF} the expansion time.

The stretching effect is shown in Fig. 9.6, where the vertical rms size of the molecular cloud after $t_{TOF} = 20$ ms of free expansion is plotted as a function of the magnetic field. The closer to the resonance pole, the more pronounced is the cloud elongation. For a magnetic field detuning larger than about 50 mG, the effect becomes less relevant and σ_z approaches the ballistic-expansion value of about 20 µm. Restricting our attention to the large detuning region, $|\delta B| > 50$ mG, we fit the data based on Eq. (9.10) with T being the only free parameter. The resulting value of $T = 27(5)$ nK is somewhat lower than what was obtained from other time of flight measurements. We attribute this discrepancy to a measurement artefact: The cloud was held in the ODT for a time interval that accidentally coincided with a minimum velocity spread during a breathing mode oscillation. Overall, the observed vertical stretching effect follows Eq. (9.10) well, which confirms our model of an anti-trapping effect described by the frequency α according to Eq. (9.9); see also inset in Fig. 9.6. Close to resonance the anti-trapping effect can substantially modify the free expansion. Only at larger magnetic field detuning ($|\delta B| \gg \delta B^*$) the effect becomes negligible.

9.5 LIFETIME

The stability of the molecular cloud against losses is of primary importance for many future experiments with our system. The fact that we work with a pure sample of molecules already eliminates collisions with free atoms as possible sources of losses. Inelastic collisions between the dimers and processes induced by the trap light thus remain as possible sources. In this section, we study the decay of the optically trapped dimer sample. We measure lifetimes up to 20 ms, and we identify trap-light induced losses as the dominant decay mechanism.

The molecular sample is prepared as described in Sec. 9.2. At the end of the purification phase, the cloud is transferred to the target field and the magnetic gradient is ramped accordingly. The molecules are held in the ODT for a variable time, after which they are released and let expand in time of flight. The molecules are dissociated 1 ms before the imaging pulse. Typical decay curves can be observed in Fig. 9.7(a) and (b), measured in a rather shallow trap ($\bar{\omega} \approx 2\pi \times 20$ Hz) at $B = 7.248$ and 6.895 G, respectively. The decay follows a simple exponential behavior, suggesting that the limiting loss process is a one-body mechanism. As the only plausible explanation, we assume that the infrared light of the ODT induces transitions into electronically excited molecular states [150].

The magnetic field detuning clearly has an impact on the lifetime of the sample: For the smaller detuning we measure a decay time almost two times longer than for the larger detuning. We systematically investigate the dependence of the lifetime on the magnetic field. The
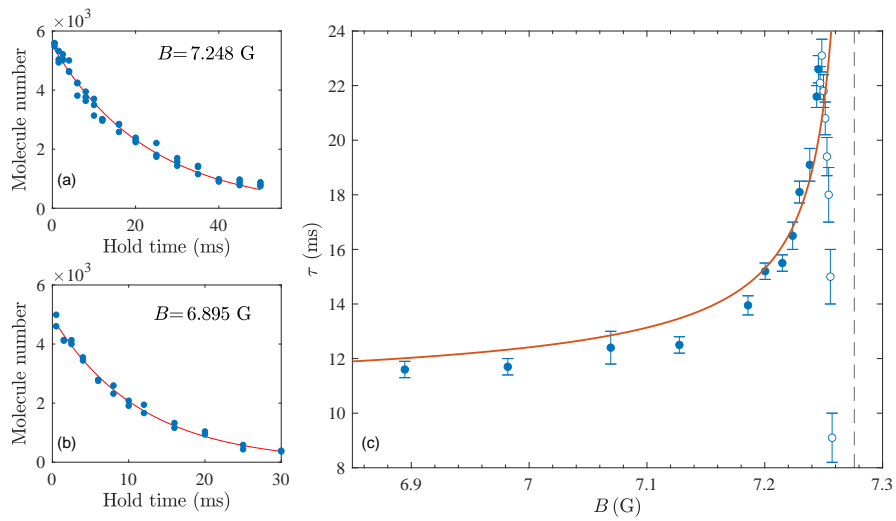
Figure 9.7: Decay of the pure trapped molecular sample. Typical decay curves are shown in panel (a) and (b); note the different time scales. The lifetimes have been measured in an ODT with trap frequency $\bar{\omega} \approx 2\pi \times 20$ Hz, at a magnetic detuning of -27 mG (a) and -380 mG (b). From an exponential fit to the data (solid lines) we derive decay times of $23.1(6)$ and $11.6(3)$ ms, respectively. In panel (c) we report decay times measured under the same experimental conditions, as function of the magnetic field strength. The solid line represents the result of a one-parameter fit (see text) to the data at large detunings ($|\delta B| > 30$ mG, filled circles). The dashed line indicates the position of the pole of the resonance.

decay times τ reported in Fig. 9.7(c) are derived from exponential fits to the corresponding lifetime curves. All curves have been recorded under essentially the same trapping conditions as for Figs. 9.7(a) and (b), with an initial molecular number varying between 5 and 6×10^3. At large detunings the sample features a relatively fast decay, with $\tau \approx 12$ ms. The lifetime of the sample rapidly increases when approaching the pole of the resonance, reaching decay times up to $\tau = 23$ ms for a magnetic field detuning of about 30 mG.

To explain the behavior we assume that the closed-channel fraction of the Feshbach molecules is responsible for the losses [150]. The optical excitation presumably couples the closed channel to some unknown electronically excited molecular states. We therefore model the lifetime by

$$\tau(B) = \tau_{closed}/Z(B), \tag{9.11}$$

where Z is the closed-channel fraction according to Eq. (9.5) and τ_{closed} is the lifetime of the closed-channel molecule. In Fig. 9.7(c) we show the corresponding behavior of $\tau(B)$ calculated with the resonance parameters as determined before and obtaining $\tau_{closed} = 10.1(4)$ ms from a single free parameter fit to the data for $|\delta B| > 30$ mG.

For $|\delta B| \lesssim 30$ mG, the observed lifetime changes dramatically, with τ rapidly decreasing while approaching the resonance pole. This different behavior can be understood in terms of the anti-trapping mechanism introduced in Sec. 9.4, which, close to to resonance pole, becomes sufficiently strong to effectively pull the molecules out of the weak ODT, thus reducing the lifetime of the sample.

To further verify that the observed losses are induced by the trap light, we measure the dependence of the loss rate on the intensity I of the trapping beam. The molecules are held in a single-beam ODT in the presence of a levitating magnetic field gradient. The lifetime curves have been recorded for different trap intensities, at a fixed magnetic field $B = 7.244$ G. Even at high intensity, for which the trap becomes very tight, the decay curves preserve a purely exponential behavior, suggesting that in the region of system parameters explored no density-dependent effects enter into play. Our results are reported in Fig. 9.8 and show a linear dependence of the loss rate on the beam intensity. This linearity indicates that the loss mechanism is not saturated, which suggests an off-resonant process to take place instead of a resonant excitation of a specific transition.

Following basically the same protocols, we have also carried out measurements on the lifetime of trapped Feshbach molecules produced via the resonance near 51.2 G, which has a very similar character to the 7.3-G resonance [12]. Here we observed a much faster light-induced decay on the timescale of one millisecond. This shows that the decay depends very sensitively on the particular closed-channel molecular state underlying the Feshbach resonance, and on its coupling to electronically excited states.
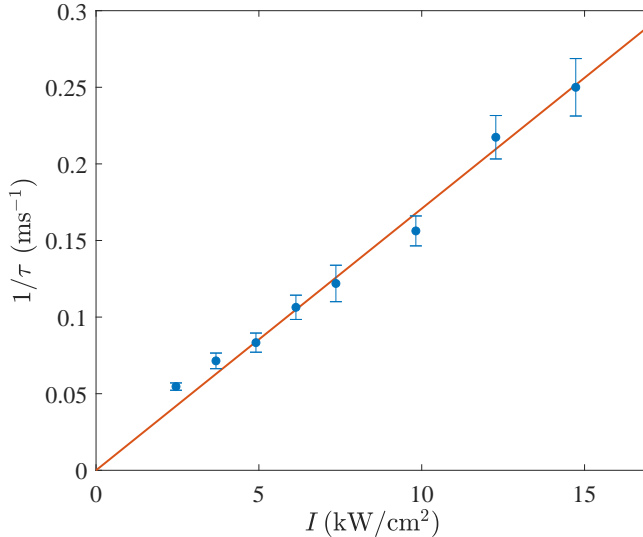
Figure 9.8: Linear dependence of the measured loss rate on the beam intensity. The rates have been measured in a single-beam ODT with a waist of 90 μm and a wavelength of 1064 nm. All data have been taken at a constant magnetic field detuning of about 30 mG. A linear fit to the data (solid line) yields a slope of $1.71(3) \times 10^{-2}\,\mathrm{cm^2s^{-1}}/\mathrm{kW}$.

Light-induced one-body losses of optically trapped Feshbach molecules have been observed in Ref. [151]. Here single KRb molecule were trapped in individual sites of an optical lattice, which shielded them and thus suppressed collisional losses. The dependence of decay times on the closed-channel fraction was also studied with similar findings as in our experiment. Trap-light-induced losses were also investigated as possible limitations to experiments with single Feshbach molecules of NaCs or RbCs in optical tweezers [152, 153]. Decay measurements on samples of optically trapped pure Feshbach molecules of RbCs [137], very similar to our experiments, also showed an exponential loss behavior, which we interpret as a result of dominant one-body losses. Such trap-light induced losses seem to be rather the rule than the exception, although they have not received much attention so far.

9.6 CONCLUSIONS AND OUTLOOK

We have demonstrated the preparation of a pure sample of ultracold DyK Feshbach molecules in an optical dipole trap, with high-phase space densities of the order of 0.1. The weakly bound molecules are composed of the fermionic isotopes ^{161}Dy and ^{40}K, which makes the sample an interesting starting point for experiments addressing the few- and many-body physics of resonantly interacting fermions with mass imbalance.

The efficient purification scheme applied in our experiments is based on a Stern-Gerlach method, where magnetic levitation keeps

the molecules in a shallow trap, while the atoms are removed by the combined action of gravity and the magnetic gradient force. We have shown that the measured dependence of the molecular magnetic moment on the magnetic field strength provides an accurate characterization of the underlying Feshbach resonance and complements spectroscopic measurements of the molecular binding energy. We have also demonstrated a peculiar effect appearing in the free expansion of the molecular cloud in the magnetic gradient field. The sharp dependence of the magnetic moment in the universal regime close to the resonance center manifests itself in a vertical antitrapping force, which leads to an anisotropy (vertical stretching) of the expanding cloud.

Lifetime studies have revealed a one-body mechanism induced by the trap light as the main limitation. We have observed that the decay rate is proportional to the closed-channel fraction of the Feshbach molecules and also proportional to the trap light intensity. This suggests an off-resonant photoexcitation mechanism that couples the closed-channel molecular state to the manifold of electronically excited states and leads to losses, possibly by photodissociation or optical pumping. Understanding and suppressing this effect needs more investigations, in particular by variation of the trap wavelength. Tuning the trap light, which was not feasible in our present setup employing fixed-frequency laser sources, will allow us to mitigate and possibly cancel photo-excitation loss processes. Generally, it can be expected that using trap light much further in the infrared than the standard 1064-nm wavelength (e.g. in the 1550 nm or 2 µm regions) will strongly reduce these losses because of a decreasing density of electronically excited molecular states that can couple to the Feshbach dimer.

Reaching quantum degeneracy with the molecular sample and thus the observation of a BEC of heteronuclear Feshbach molecules will presumably require a final stage of evaporative cooling. Under the current conditions, however, it can be estimated the a molecule only undergoes roughly one elastic collision in the limited lifetime of the sample. Overcoming this limitation demands both a substantial improvement of the lifetimes (by optimizing the trap wavelength) and an increase in the elastic collision rate. The latter can be achieved by working at small magnetic detunings very close to the resonance center. Deep in the universal regime, the molecular s-wave scattering length is predicted to follow the atomic scattering length, $a_{\mathrm{mol}} \approx 0.77 \, a$ [39], and will thus also be resonantly enhanced. Moreover, the increasing Pauli blocking of inelastic collisions near resonance [38, 39] will strongly suppress collisional losses, which is a well-established effect in spin-mixtures of fermions [18] and has also been observed in a heteronuclear K-Li Fermi-Fermi mixture [40]. The magnetic antitrapping effect that is caused by the levitation field may be overcome by, e.g., using a standing-wave trap that provides tight vertical confinement. Taking advantage of all these potential improvements, we are

confident that a sufficiently high ratio of elastic vs. inelastic molecule-molecule collisions can be reached to implement efficient evaporative cooling towards quantum degeneracy.

9.7 APPENDIX A: MAGNETIC FIELD CONTROL

Precise magnetic field control is crucial for an efficient production of the molecular sample, as well as for the precise determination of the Feshbach resonance parameters. In this regard, we put a lot of efforts into the implementation of an effective magnetic-field ramping protocol, as well as into the development of a precise current actuator for the coils that produce the magnetic field. The Feshbach magnetic field is produced employing two pairs of coils.

The offset magnetic field B_{off} is generated by a slow set of coils (offset coils), whose proportional-integral-derivative (PID) actuator settings are optimized to perform the large magnetic field ramp within 2 ms. Every magnetic field ramp unavoidably induces some eddy currents in the apparatus, which delay the response of the actual magnetic field with respect to the targeted behavior. We minimize this undesired effect by applying a feed-forward scheme on the current ramp. Furthermore, we wait about 50 ms after the ramp, to allow the magnetic field to fully stabilize to the set point. The magnetic field noise is measured to be below 2 mG peak to peak. The residual magnetic-field produced by the offset coils provides a fixed stable offset, which is left unvaried for the rest of the sequence.

The magnetic field ramps discussed in Sec. 9.2.2 are performed by means of a low-inductance coils (fast coils) whose magnetic field is superimposed with B_{off} provided by the offset coils. The fast coils can handle a maximum current of about 10 A, corresponding to about 3 G. The current flow is regulated with a metal–oxide–semiconductor field-effect transistor (MOSFET) whose gate voltage is controlled digitally via a field programmable gate array (FPGA). Following the work reported in Ref. [154], the FPGA is programmed to optimize the feedback loop and to set the PID parameters accordingly during the current ramp. The quality of the digital PID controller and the low current-to-field conversion factor are such that the fast coils do not introduce extra magnetic field noise in the system.

PUBLICATION: OPTICALLY TRAPPED FESHBACH MOLECULES OF FERMIONIC ^{161}DY AND ^{40}K: ROLE OF LIGHT-INDUCED AND COLLISIONAL LOSSES

Alberto Canali, Chun-Kit Wong, Luc Absil,
Zhu-Xiong Ye, Marian Kreyer, Emil Kirilov, and
Rudolf Grimm.

Author contribution: The author took a supporting role in the process of acquiring and analyzing the data described in this publication as well as writing the manuscript.

We study the decay of a dense, ultracold sample of weakly bound DyK dimers stored in an optical dipole trap. Our bosonic dimers are composed of the fermionic isotopes ^{161}Dy and ^{40}K, which is of particular interest for experiments related to pairing and superfluidity in fermionic systems with mass imbalance. We have realized dipole traps with near-infrared laser light in four different wavelength regions between 1050 and 2002 nm. We have identified trap-light-induced processes as the overall dominant source of losses, except for wavelengths around 2000 nm, where light-induced losses appeared to be much weaker. In a trap near 1550 nm, we found a plateau of minimal light-induced losses, and by carefully tuning the wavelength we reached conditions where losses from inelastic collisions between the trapped dimers became observable. For very weakly bound dimers close to the center of a magnetically tuned Feshbach resonance, we demonstrate the Pauli suppression of collisional losses by about an order of magnitude.

10.1 INTRODUCTION

Since its first demonstration almost 40 years ago [155], the trapping of atoms by the optical dipole force in off-resonant laser light [156] has become a key technique in modern atomic physics and quantum sciences [157]. Optical dipole traps (ODTs) have found numerous applications, e.g. for ultraprecise atomic clocks [158, 159], for precision measurements [3, 160, 161], and for quantum computation and simulation [162–165]. In the broad research field of ultracold quantum gases [18, 68, 166], optical dipole trapping schemes have, in many cases, served as the enabling tool to achieve quantum degeneracy [45, 167, 168] and to create novel quantum-degenerate systems with single species, spin mixtures, and mixtures of different species.

In the rapidly developing field of ultracold molecules, ODTs are widely employed for the preparation of cold and dense atomic samples, serving as a starting point to create molecules by subsequent photo- [169, 170] or magneto-association [17, 119] techniques. A multitude of different experiments have been carried out on optically trapped molecules, such as collisional studies [171–173] and the manipulation of internal states [148, 174, 175]. The most prominent example of this is the transfer of dimers to their rovibronic ground state [176–178]. Quantum degeneracy of molecular samples was achieved more than 20 years ago with the observation of molecular Bose-Einstein condensation (BEC) of weakly bound pairs of fermionic atoms [127–129] and the experimental realization of the crossover from BEC to Bardeen-Cooper-Schrieffer (BCS) type systems [19, 20, 130, 179, 180]. The condensation of weakly bound molecules made of bosonic atoms

was demonstrated in Ref. [181] and, most recently, BEC of ground-state dipolar molecules was achieved [182, 183]. Another important development in the field is the optical dipole trapping and manipulation of diatomic [152, 184, 185] and polyatomic [186, 187] molecules using optical tweezers and tweezer arrays. To fully exploit the wide application potential of ODTs for experiments on ultracold molecular samples, thorough understanding of the limiting processes is required. The complex interactions between molecules along with their very rich level structure can lead to additional effects not relevant for trapped atomic samples.

In our laboratory, we have demonstrated [89] the preparation of optically trapped samples of weakly bound bosonic dimers, composed of two different fermionic constituents, ^{161}Dy and ^{40}K. We have achieved efficient molecule production by applying standard magneto-association techniques ('Feshbach ramps' [17, 119]) to a double-degenerate atomic mixture. The samples of 'Feshbach molecules' created in this way are of great interest in view of molecular Bose-Einstein condensation in heteronuclear systems and, in a more general sense, as a starting point for the realization of many-body states of strongly interacting fermions with mass imbalance in BEC-BCS crossover regimes [5, 37, 188]. Such systems are particularly promising for the realization of asymmetric superfluids with unconventional pairing mechanisms [22–25], most notably the elusive Fulde-Ferrell-Larkin-Ovchinnikov (FFLO) state [26–28]. In addition to that, a variety of interesting few-body phenomena has been predicted to emerge in resonant fermion mixtures [70, 76, 189].

A question of central importance concerns the stability of the trapped dimer sample against inelastic dimer-dimer collisions. For homonuclear dimers in fermionic spin mixtures, it is well known that a Pauli suppression effect [18, 38] can strongly reduce collisional losses, thus greatly enhancing the stability of the system. We would expect a similar effect to be present for our weakly bound DyK molecules [39, 40], however, our early attempts to study collisional effects [89] were obstructed by another, by far dominant loss mechanism. Our experiments provided strong evidence for a light-induced decay caused by the ODT itself. The loss effect has been noted before in a few bi-alkali molecular systems [151–153], but it appears to play a much more important role for more complex dimers like LiCr [90] and DyK.

In the present work, we report on systematic studies of losses from an optically trapped, dense sample of weakly bound DyK molecules. After summarizing the main properties of the dimers in the vicinity of a Feshbach resonance (Sec. 10.2) and outlining the main experimental procedures and conditions in (Sec. 10.3), we present detailed measurements of trap-light-induced losses (Sec. 10.4). We investigate four different wavelength regions in the near-infrared, carrying out spectroscopic wavelength scans in certain regions of interest and measuring

the linear coefficient that characterizes intensity-dependent losses. We also identify regions of minimal losses. With a proper choice of the trap wavelength mitigating the detrimental effect of light-induced losses, we identify the losses caused by inelastic dimer-dimer collisions (Sec. 10.5) and we measure the corresponding rate coefficient as a function of the magnetic detuning from resonance. We indeed observe a reduction of collisional losses close to resonance by about an order of magnitude, which is in accordance with theoretical expectations for the Pauli suppression effect. Finally (Sec. 10.6), we discuss the implications of our findings for future experiments.

10.2   DYK FESHBACH MOLECULES

As our essential tool to control the s-wave interaction between ^{161}Dy and ^{40}K atoms and to form molecules, we employ a low-field interspecies Feshbach resonance near 7.3 G [12, 89]. The narrow resonance is well isolated from other interspecies resonances and can thus be described in terms of a standard two-channel model well established in the literature [17, 43]. Moreover, the resonance is not contaminated by intraspecies resonances [12]. To set the stage, we summarize the main properties of this resonance and the relevant parameter values, which were accurately determined in our previous work [12, 89].

Close to the resonance, the s-wave scattering length can be expressed as

$$a(B) = a_{\mathrm{bg}} - \frac{A}{\delta B}\, a_0, \frac{num}{den} \qquad (10.1)$$

where A characterizes the strength of the resonance, $\delta B = B - B_0$ represents the magnetic detuning from the resonance center, a_{bg} denotes the background scattering length, and a_0 is the Bohr radius. To our best knowledge, resonance parameters are $B_0 = 7.276(2)\,\mathrm{G}$, $A = 24.0(6)\,\mathrm{G}$, and $a_{\mathrm{bg}} = 23(5)\,a_0$ [12, 89]. In Fig. 10.1(a), we show the scattering length in proximity to the resonance.

In the case of a 'narrow' Feshbach resonance, also referred to as 'closed-channel dominated resonance' [17], it is necessary to introduce an additional parameter to fully characterize the interaction properties. For this purpose, it is convenient to consider the range parameter $R^* = \hbar^2/(2m_r a_0 \delta \mu A)$ [43], where m_{r} is the reduced mass and $\delta \mu = \mu_{\mathrm{open}} - \mu_{\mathrm{closed}}$ is the difference in magnetic moments between the atomic scattering state (open channel) and the molecular state underlying the Feshbach resonance (closed channel). For $a \gtrsim R^*$, the interaction physics acquires universal behavior in the sense that a single parameter, such as the scattering length, is sufficient to describe the underlying physics [143]. For the resonance considered here $R^* = 604(20)\,a_0$, which corresponds to a universal regime accessible for $|\delta B| \lesssim 40\,\mathrm{mG}$.

The molecular state energy related to a narrow Feshbach resonance can be expressed as

$$E_{\text{mol}}(B) = -\delta\mu\,\delta B^* \left(\sqrt{1 - \frac{\delta B}{\delta B^*}} - 1 \right)^2 . \tag{10.2}$$

Here, for brevity, we have introduced the magnetic field scale $\delta B^* = m_r\,\delta\mu\,a_0^2\,A^2/(2\hbar^2)$, for which $a(-\delta B^*) = 4R^*$, which corresponds to $\delta B^* = 9.9(6)\,\text{mG}$, in our case. In Fig. 10.1(b), we show the binding energy of the DyK dimers according to Eq. (10.2), in the magnetic detuning range $-500\,\text{mG} < \delta B < 0$.

The closed-channel fraction quantifies the admixture between the bare molecular state and the free-atom scattering state in the wavefunction of the Feshbach molecules. It can be obtained from the molecular binding energy through the differential magnetic moment, $\delta\mu_{\text{mol}}(B) = \partial E_{\text{mol}}/\partial B$. The closed-channel fraction is then given by

$$Z(B) = \delta\mu_{\text{mol}}(B)/\delta\mu, \tag{10.3}$$

and Fig. 10.1(c) shows the resulting $Z(B)$ for DyK molecules near the 7.3-G resonance.

10.3 EXPERIMENTAL SEQUENCE

The preparation of the molecular sample closely follows the procedures developed in our previous work [2, 12, 89]. As a starting point, a double-degenerate mixture of ^{161}Dy and ^{40}K is prepared with both species spin-polarized in their lowest hyperfine states, $|F, m_F\rangle = |21/2, -21/2\rangle$ and $|9/2, -9/2\rangle$, respectively. This is particularly relevant in the present work, as molecules formed in the lowest hyperfine spin channel are immune against spontaneous dissociation, thus avoiding fast corresponding losses as studied for homo- and heteronuclear Feshbach molecules in Refs. [40, 190].

We first prepare the double-degenerate atomic mixture at low magnetic field and then ramp the field to the vicinity of the 7.3 G-Feshbach resonance. DyK molecules are subsequently associated by performing a magnetic field sweep across this resonance [17, 89]. The molecular sample obtained by this Feshbach ramp is then purified by removing the remaining atoms using a Stern-Gerlach technique [89]. With this procedure, we produce a pure molecular sample of typically 10 000 DyK molecules at a temperature of around 70 nK, with mean trap frequency $\bar{\omega} = 2\pi \times 31\,\text{Hz}$. Compared with our previous work, we are now able to obtain twice the number of molecules. We achieve this improvement by carefully optimizing both the mixture preparation sequence and the Stern-Gerlach purification scheme. In particular, we perform the cleaning sequence at a detuning of $\delta B = -40\,\text{mG}$, which is 80 mG closer to resonance than previously, and reduces light-induced losses of molecules during the process.
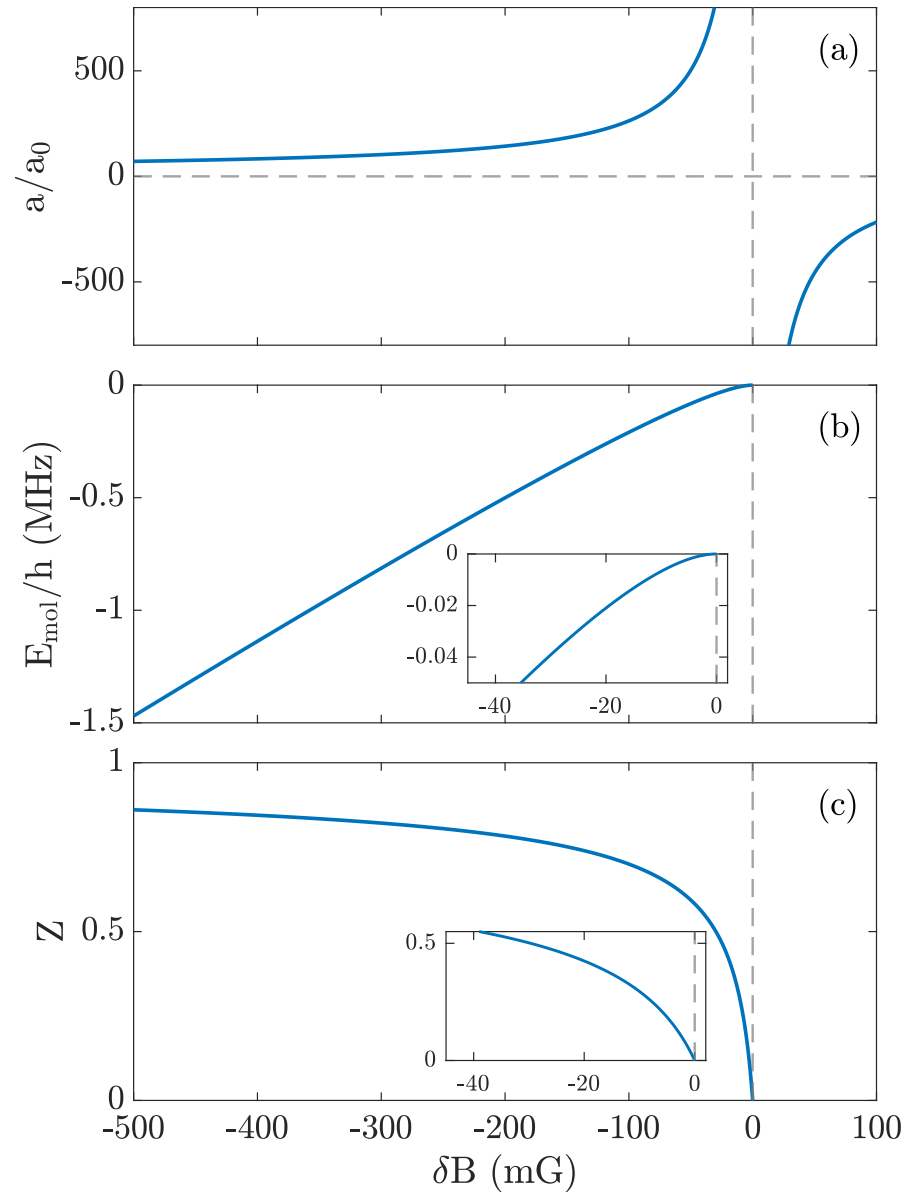
Figure 10.1: Properties of the 7.3-G Feshbach resonance. (a) Scattering length a, (b) molecular state energy E_{mol}, and (c) closed-channel fraction Z as functions of the magnetic detuning δB. The insets in (b) and (c) focus on the near-universal region close to resonance.

All results presented in this work are based on measuring the number of the molecules after a variable hold time in a target ODT. After the purification process, the molecular sample is transferred into the ODT under investigation, where the measurement takes place. At the end of the investigation time, the ODT is switched off and the magnetic field is quickly ramped across the resonance to positive detunings, thus dissociating the molecules. The number of molecules is finally obtained from absorption images of the resulting K atoms [1].

10.4 LIGHT-INDUCED LOSSES

We investigate the dependence of light-induced losses on wavelength and intensity of the near-infrared light used for the ODT. In Sec. 10.4.1, we report the results of spectroscopic measurements performed on the DyK Feshbach dimers in two different wavelength regions. In Sec. 10.4.2, we compare light-induced losses at different wavelengths by observing the dependence of loss rate on intensity.

10.4.1 *Spectroscopy in two regions of interest*

We perform spectroscopy on the DyK Feshbach molecules by scanning the wavelength of the near-infrared trapping light and observing losses from the ODT. For generating the trap light, we have the choice between two fiber lasers, with wavelengths centered around 1051 nm (NKT Koheras BOOSTIK Y10, linewidth < 20 kHz) and 1547 nm (NKT Koheras BOOSTIK E15, linewidth < 0.1 kHz). Both lasers feature a tuning range of around 1 nm.

The molecules are loaded within 1 ms from a 1064-nm crossed-beam ODT into the single-beam ODT used for spectroscopy. The molecules are then held at a magnetic detuning of $\delta B = -60$ mG for a fixed amount of time, while being levitated by a magnetic field gradient. We choose a hold time of 10 ms for the 1051-nm case and 33 ms for the 1547-nm case, in order to obtain a similar contrast for loss features in the two signals. We report the main results of these measurements in Fig. 10.2 [2]. For the 1051-nm case, the ODT has a waist of 72 μm and a power of 46 mW, corresponding to a peak intensity of 0.55 kW/cm². For the 1547-nm case, the ODT has a waist of 90 μm and the measurements were taken using a power of 220 mW, corresponding to a peak intensity of 1.7 kW/cm².

In Fig. 10.2(a), we report the result of the trap-loss spectroscopy for the 1051-nm case. Our main observation is a broad loss feature, showing a large width of about 0.2 nm (~ 60 GHz) together with very

---

1 The potassium imaging provides a better quality signal compared to the Dy ones, due to the higher absorption cross section.

2 See Supplemental Material at link to be added by publischer for the data files of all figures
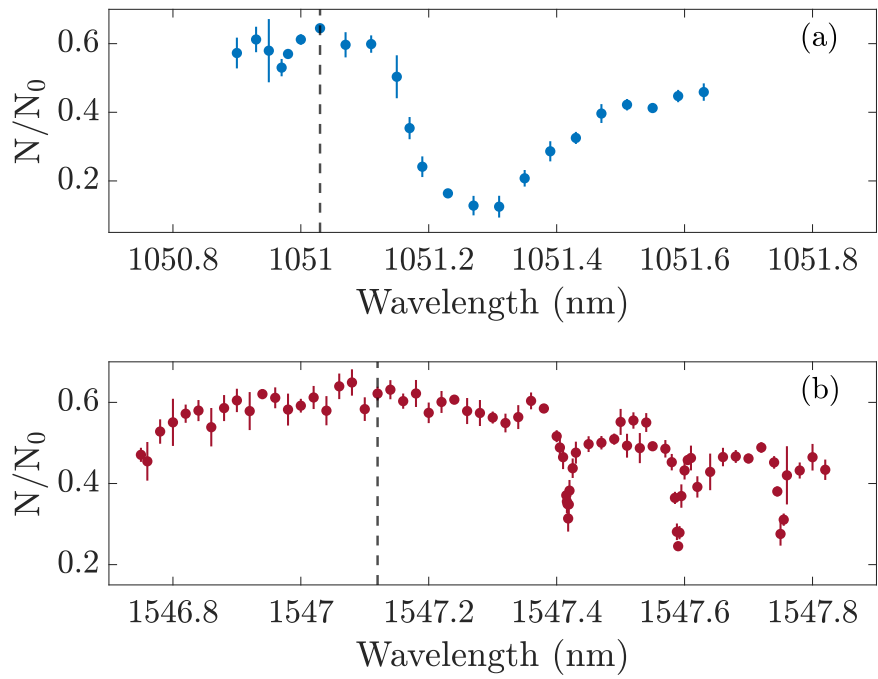
Figure 10.2: Trap-loss spectroscopy on DyK Feshbach molecules by variation of the ODT wavelength. Panel (a) refers to the region around 1051 nm, with initial number $N_0 = 1.1 \times 10^4$ and a hold time of 10 ms. Panel (b) refers to the region around 1547 nm, with $N_0 = 9 \times 10^3$ and a hold time of 33 ms. The error bars represent 1σ standard errors, calculated from multiple repetitions. The vertical dashed lines in (a) and (b) indicate the selected wavelengths 1051.03 nm and 1547.12 nm, respectively, used for all further measurements presented in this work.

fast losses. This suggests a strong, resonant transition into the manifold of electronically excited molecular states, which presumably leads to dissociation of the molecules [169]. We also identify a plateau with a local maximum of the molecular lifetime on the shorter wavelength side of the resonance.

In Fig. 10.2(b), we show a corresponding spectroscopic measurement in the region around 1547 nm. In contrast to the 1051-nm case, we do not observe any broad resonance features. Instead, we identify three much sharper loss features on a slowly varying background. By performing individual Lorentzian fits on each of the features, we extract a typical linewidth (full width at half maximum) of approximately 1.2 GHz and a separation between neighboring lines of about 20 GHz. This separation between the lines is of the order of typical rotational splittings in diatomic molecules, as observed in other heteronuclear systems, like KRb [191], and NaRb [192, 193]. However, without any knowledge of the DyK molecular structure, a comprehensive interpretation is not possible.

10.4.2 *Dependence on light intensity*

Here we investigate the dependence of the observed light-induced losses on the intensity of the trapping light. For the two wavelength regions discussed before, we avoid loss resonances by choosing the specific wavelengths where we have identified plateaus with minimal losses, at 1051.03 nm and 1547.12 nm (vertical dashed lines in Fig. 10.2). In addition to these two wavelengths, we operate an ODT based on a single-frequency fiber laser at 2002 nm (Precilaser FL-SF-2001-20-CW, linewidth $\sim$ 5 kHz), and we reanalyze our earlier measurements with a single-frequency laser at 1064.04 nm (Azurlight ALS-IR-1064-5-I-CC-SF, linewidth $<$ 50 kHz) [89]. The experiments with four different laser sources allow us to investigate and compare the loss behavior in four different near-infrared wavelength regions.

The 1064-nm laser source is not tunable and therefore does not allow for a search of points of minimal losses. This makes the choice of the wavelength a matter of chance, but with a reasonable probability to avoid detrimental resonances. Regarding the 2002-nm light, we performed similar wavelength scans as the ones near 1051 nm and 1547 nm, but strong interference effects in our optical set-up, which was not designed for this wavelength, masked the signal and we could not identify any resonance structure related to light-induced losses. As an arbitrary choice for our further experiments, we set the wavelength to 2002.00 nm.

All measurements on the intensity dependence are carried out with the molecules held in a single-beam ODT, with a waist of 72, 90, 90, and 120 μm for the wavelengths 1051, 1064, 1547, and 2002 nm, respectively.

To extract the loss rates for the different cases, we record decay curves for hold times of up to 1 s. Assuming one-body effects (processes involving one molecule) to dominate, we fit the different loss curves, except the 2002-nm case, with a simple exponential decay, $N(t) = N_0 \exp\{(-\alpha t)\}$, where the initial molecule number N_0 and the loss rate coefficient α are kept as free parameters. For the 2002-nm case, the one-body contribution to loss is strongly reduced and two-body contributions (dimer-dimer collisions) to the decay process can no longer be neglected. Consequently, we fit the lifetime data, taking into account both one- and two-body contributions according to the expression [40]

$$N(t) = N_0 \frac{\exp\{(-\alpha t)\}}{1 + \frac{N_0\,\beta}{\alpha\,V_{\text{eff}}}[1 - \exp\{(-\alpha t)\}]}, \tag{10.4}$$

where β is the two-body loss coefficient, and $V_{\text{eff}} = [(4\pi k_B T)/(m\bar{\omega}^2)]^{3/2}$ is the effective volume of the sample, with m being the mass of the dimer, T the temperature and $\bar{\omega}$ the mean trapping frequency. We will discuss in detail the role of collisional losses in Sec. 10.5.
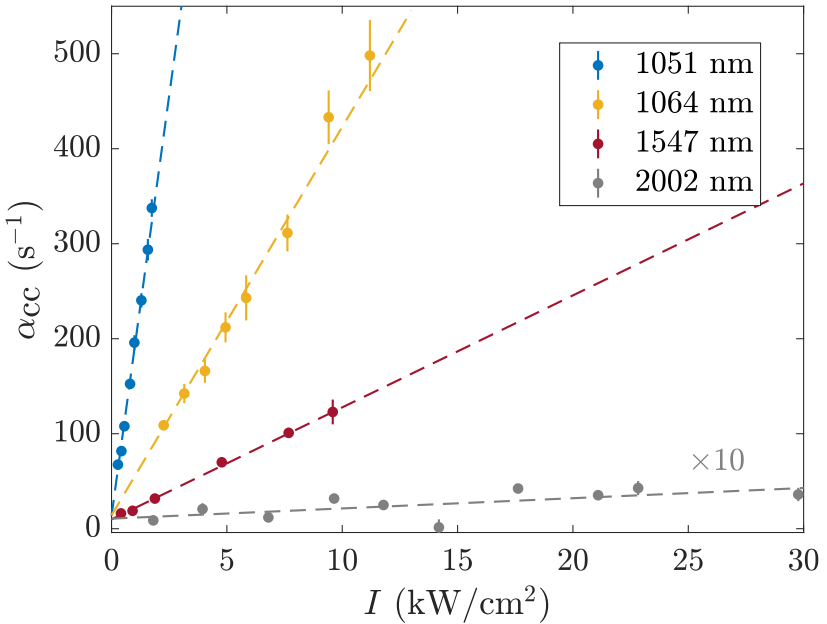
Figure 10.3: Loss rate as a function of the trapping beam peak intensity. We show the closed-channel one-body loss rates measured in the experiments for the 1051.03 nm, 1547.12 nm, and 2002.00 nm ODTs in blue, red and gray dots, respectively. Note that the data and fit result for the 2002-nm case have been scaled by a factor of 10 for better visibility. For comparison, we also show the data for a trap at 1064.04 nm in yellow, already reported in [89]. The data are shown with 1σ error bars derived from the lifetime fits (in some cases smaller than the symbol size). For conversion of intensity (in kW/cm^2) to optical potential depth (in μK) use the factors 1.76, 1.81, 1.25, and 1.15 for the wavelength 1051 nm, 1064 nm, 1547 nm, and 2002 nm, respectively.

Trap-light-induced losses in Feshbach molecules can essentially be attributed to the coupling between the trapping light and the closed-channel fraction of the weakly bound dimers. The role of the closed-channel fraction has been studied for the case of Li$_2$ molecules [150], for KRb molecules [151], and in our group for DyK molecules [89]. To facilitate a comparison between our different measurements, taken at magnetic-field detunings between -30 mG and -60 mG, we convert the measured values of the loss rate α, which depend on the magnetic field, to the asymptotic loss rate α_{cc} using the relation

$$\alpha(B) = \alpha_{\mathrm{cc}} Z(B), \tag{10.5}$$

where $Z(B)$ is the closed-channel fraction as calculated according to Eq. (10.3). The different values for closed-channel fraction for each measurement are reported in Table 10.1.

Wavelength (nm)	Z	Γ_{cc} ($s^{-1}\,cm^2$/kW)
1051.03	0.62	177(7)
1064.04	0.50	41(2)
1547.12	0.58	8.4(7)
2002.00	0.58	0.11(5)

Table 10.1: Measured values for the coefficient Γ_{cc}, which for light-induced losses characterizes proportionality between loss rate and light intensity. The 1051-nm and 1547-nm values are obtained after careful optimization of the wavelength to avoid resonant processes, while the 1064-nm and 2002-nm case are at an arbitrary wavelength (see text for details). We also report the values of the closed-channel fraction $Z(B)$ used to calculate the closed-channel loss rates for each wavelength, according to Eq. (10.3).

In Fig. 10.3, we show the closed-channel loss rate α_{cc} as function of the light intensity I for the different ODTs, together with a linear fit

$$\alpha_{cc} = \Gamma_{cc} I + \alpha_0, \tag{10.6}$$

to each data set. These fits yield a wavelength-specific coefficient Γ_{cc}, which quantifies the slope for each data set [3]. The resulting values are summarized in Table 10.1. They show a dramatic variation of Γ_{cc} over more than three orders of magnitude. The linear fit also indicates the presence of weak, residual background losses (parameter α_0), which are not induced by the trap light and play no role for our present experiments. Similar measurements on light-induced decay have been reported for LiCr Feshbach molecules in Ref. [90], also demonstrating an order-of-magnitude reduction with increasing wavelength in the infrared.

The observed decrease of the light-induced loss rates with larger wavelengths, i.e. lower photon energies, can be explained by a reduced density of electronically excited molecular states that can resonantly couple to the Feshbach molecules. Below a certain threshold wavelength, which is given by the energy difference between the lowest molecular state (the rovibronic ground-state of lowest molecular potential), resonant excitation is no longer possible. This wavelength sets a natural scale for the appearance or disappearance of light-induced losses. For diatomic molecules in ultracold gases, it typically lies in a range between 1.7 μm and 2.8 μm [4].

---

3 Because of the thermal spatial distribution in the trap, the molecules sample a mean intensity, which is typically 25 % below the peak intensity. Therefore our values of Γ_{cc}, which are simply calculated with the peak intensity, underestimate the true values. This, however, is a small effect regarding the enormous variation of Γ_{cc} in our experiments.

4 Examples for the threshold wavelength of bi-alkali molecules are 1820 nm for KRb [176], 1890 nm for NaCs [194], 2000 nm for RbCs [138]. For dimers involving other atoms: 2200 nm for RbSr [195], 2660 nm for LiCr [90].

Our results highlight the benefit of laser sources in the wavelength region of $2\,\mu m$ for trapping of ultracold molecules. They combine extreme detuning (previously realized in quasi-electrostatic traps based on CO_2 laser light at $10.6\,\mu m$ [156, 196]) to avoid any molecular excitations with the practical advantages of modern fiber laser technology. Currently, the $2\,\mu m$ wavelength region is not common in molecular quantum-gas experiments, but it holds great potential for future experiments.

Our present setup was not designed to use such a wavelength. In particular, the viewports of the vacuum apparatus are not anti-reflection coated for this wavelength, and we observed reflections of the light up to 30%. Scanning the laser wavelength, we observed that these reflections caused interference effects, such as a parasitic lattice. However, in future experiments, this technical limitation can be overcome by using dedicated optics in an improved setup, which will allow us to take full advantage of the wavelength region around $2\,\mu m$.

10.5   COLLISIONAL LOSSES AND PAULI SUPPRESSION

Having understood the role of losses induced by the trap light, we are now in a position to thoroughly investigate the contribution of inelastic collisions to the decay of the molecular sample. In particular, it is well known that, in the universal regime close to the resonance center, collisional losses are reduced by Pauli suppression. This has been observed in samples of weakly bound bosonic molecules composed of fermionic atoms (^{6}Li [125, 126], ^{40}K [58] and ^{6}Li^{40}K [40]).

In order to observe collisional processes in the DyK molecular sample, it is essential to minimize light-induced decay while achieving a high collisional rate. Besides optimization of the trap light wavelength, this requires an ODT that provides tight confinement at a relatively low central intensity. This means that tightly focused laser beams need to be applied. Because of the technical limitations in our present set-up, this is not possible with the 2002-nm light, and we therefore conducted this measurement with the 1547-nm laser light.

The trap consists of a crossed-beam ODT at 1547 nm. The main trapping beam propagates along the horizontal plane and is focused on the molecules with a waist of $25\,\mu m$. For additional confinement in the axial direction of the tight trap, we add a vertical beam, with a waist of $120\,\mu m$. A magnetic gradient is applied to levitate the molecules. In this ODT, the geometrically averaged trap frequency is $\bar{\omega} = 2\pi \times 32\,\text{Hz}$. With this configuration, we obtain between 5500 and 7000 molecules, at a temperature of around $90\,\text{nK}$, corresponding to peak densities up to $7.6 \times 10^{11}\,\text{cm}^{-3}$, entering the regime where collisional losses play an important role. The power used for the horizontal (vertical) beam is $4.6\,\text{mW}$ ($51\,\text{mW}$). The total light intensity
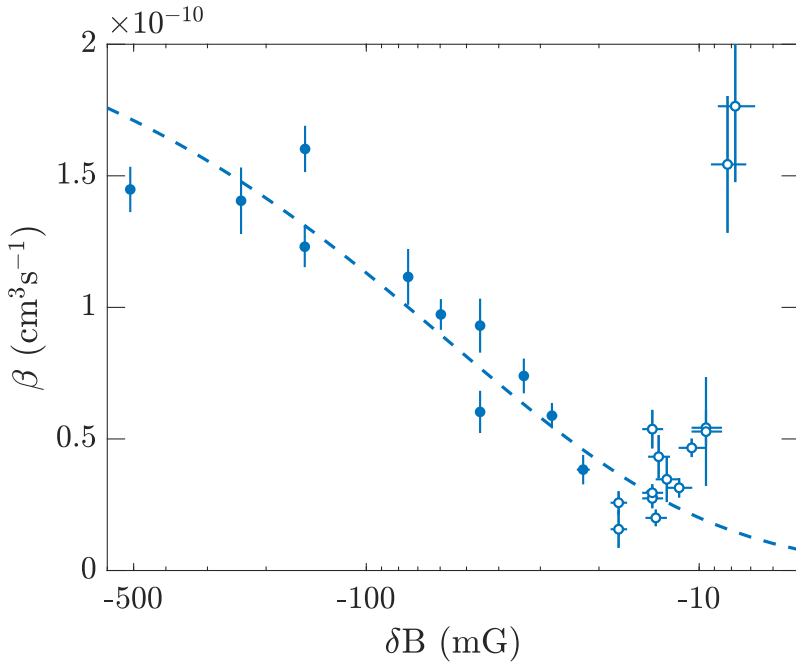
Figure 10.4: Two-body loss rate coefficient versus magnetic detuning from resonance. The dashed line represents a one-parameter fit of Eq. (10.7) to the data points for detunings $\delta B < -20\,\text{mG}$ (filled symbols). Additional measurements (open symbols) closer to resonance, presumably beyond the limitations of our simple model, have not been taken into account for the fit. Vertical error bars indicate 1σ errors, derived from fits to the decay curves. The horizontal error bars represent the 2-mG peak-to-peak magnetic field noise.

is $0.71\,\text{kW/cm}^2$. Based on the results of Sec. 10.4.2, we can expect a closed-channel loss rate of $\alpha_{cc} = 6.0(7)\,\text{s}^{-1}$.

In order to study the Pauli suppression of inelastic collisions expected close to resonance, we measure the two-body coefficient β for different detunings from the Feshbach resonance. We extract values for β by analyzing the decay of the sample at different magnetic field strengths and fitting Eq. (10.4) to the data, with N_0, α, and β as free parameters. The values obtained in this way for α (not shown) follow the general behavior according to Eq. (10.5) and yield $\alpha_{cc} = 6.2(2)\,\text{s}^{-1}$, which is fully consistent with the results of Sec. 10.4.2, and follows the behavior observed in Ref. [89]. Our experimental values for the magnetic-field dependent two-body coefficient β are displayed in Fig. 10.4. We indeed observe a clear reduction of β for magnetic fields approaching the resonance center, which we interpret as the expected suppression effect.

In Ref. [40], collisional relaxation of weakly bound dimers composed of fermionic atoms has been modeled, considering the situation near a narrow Feshbach resonance. In this work, DyK molecules have served as a specific example. According to the model, collisional

relaxation takes place in three different channels, the two atom-dimer channels (atoms of Dy or K with closed-channel DyK dimers) and the dimer-dimer channel. Consequently, the total collisional relaxation rate is obtained as a linear combination of the relaxation rates for each channel weighted with a specific suppression function that contains the Pauli blocking effect.

For magnetic detunings outside of the universal range ($a \lesssim R^*$ corresponding to $|\delta B| \gtrsim 4\delta B^*$), the model can be further simplified. Here the dimer-dimer channel dominates the relaxation and the contribution of the two atom-dimer channels can be neglected. The suppression function for the dimer-dimer channel simplifies to the squared closed-channel fraction, $Z^2(B)$, and we can approximate the relaxation rate coefficient by

$$\beta(B) = \beta_0 \, Z^2(B), \tag{10.7}$$

with β_0 as the only free parameter. A corresponding fit to the experimental data, shown by the dashed line reported in Fig. 10.4, describes well the data for $\delta B < -20 \, \text{mG}$, a range over which the closed-channel character of the molecules is expected to prevail. From the fit we obtain the closed-channel dimer-dimer asymptotic rate coefficient $\beta_0 = 2.3(1) \times 10^{-10} \, \text{cm}^3\text{s}^{-1}$. This value is comparable with predictions from a quantum Langevin model calculated for similar systems [197–199]. The minimum value $\beta \approx 2.5 \times 10^{-11} \, \text{cm}^3\text{s}^{-1}$ is obtained around the detuning $\delta B = -17 \, \text{mG}$, reported in Fig. 10.5, and shows a reduction of β by about an order of magnitude, compared to the asymptotic value.

Closer to resonance, a further decrease of β may be expected as a consequence of the increasing role of the fermionic nature of the dimer's constituents [40]. However, for $\delta B \gtrsim -13 \, \text{mG}$, we observe a rapid increase of the two-body coefficient. We attribute this to a combination of different effects leading to a dissociation of the very weakly bound dimers. One contribution is caused by the magnetic field gradient, which makes the exact resonance position dependent on the vertical position. At a detuning of $-10 \, \text{mG}$ the resonance pole is located only few tens of µm above the center of the molecular cloud, which is comparable with the vertical extension of the cloud. Moreover the transfer of the molecules between different traps excite a weak dipole mode in the vertical direction, bringing the molecules even closer to the resonance pole. Additionally, in this region of the magnetic field, the binding energy of the molecules is only a few hundred of nK, less than an order of magnitude above the thermal kinetic energy of the molecules. In this regime, endoergic collisions can lead to dissociation of the weakly bound dimers [126, 200]. Understanding the particular role and interplay of these dissociation effects will require more investigations, e.g. in optical trapping schemes combined with homogeneous magnetic fields. Closer to resonance there is potential for further enhancing the fermionic suppression effect.
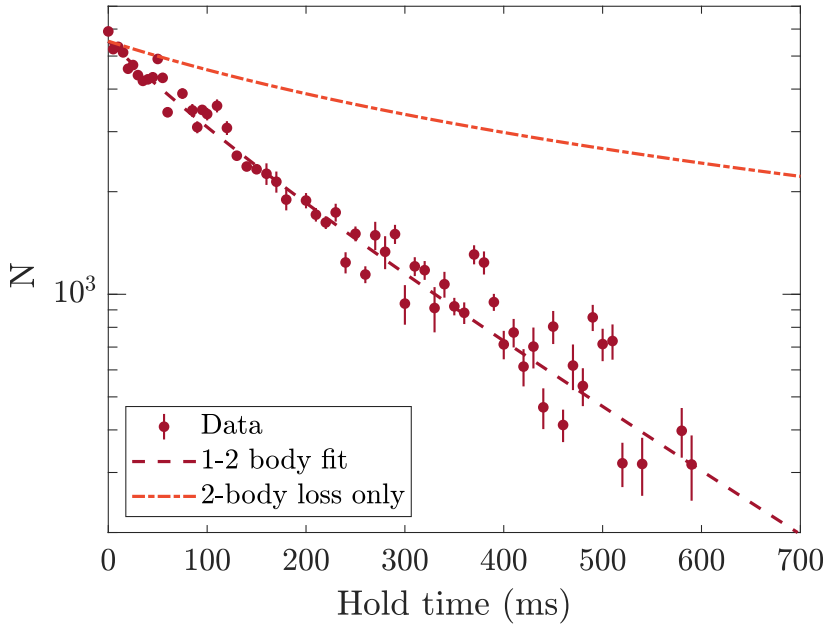
Figure 10.5: Collisional decay and the role of light-induced decay, observed in a 1547-nm trap. The red dots show the number of molecules measured after a variable hold time. The red dashed line represents a fit according to Eq. (10.4). The orange dot-dashed line shows a hypothetical loss curve with the same two-body loss in the complete absence of one-body losses.

In Fig. 10.5, we show the observed decay of the molecular sample at the detuning $\delta B = -17\,\text{mG}$, where we have identified minimal collisional losses (lowest value of β in Fig. 10.4), together with the best fit according to Eq. (10.4). As a guide for future experiments, we consider the hypothetical case where light-induced losses are completely absent and only two-body collisional losses remain. Thus setting $\alpha \to 0$ and using the fitted parameter values for N_0 and β, we obtain the decay curve expected in the absence of light-induced losses, shown as the orange line in the figure. This analysis demonstrates that, in a trapping regime free of light-induced losses, substantially longer decay times are achievable than in our present experiments.

Finally, it is very instructive to compare the elastic collision rate in the trapped dimer sample with the loss rate under the best conditions we could achieve ($\delta B = -17\,\text{mG}$). The elastic scattering rate can be calculated as $\gamma_{\text{el}} = \bar{n}\sigma\bar{v}_{\text{rel}}$, with the mean number density $\bar{n} = \frac{1}{\sqrt{8}}N(m\bar{\omega}^2/(2\pi k_B T))^{3/2}$, the mean relative velocity $\bar{v}_{\text{rel}} = (16k_B T/(\pi m))^{1/2}$, and the scattering cross section $\sigma = 8\pi a_{\text{mol}}^2$, where $a_{\text{mol}} = 0.77\,a$ represents the dimer-dimer scattering length [39, 201]. For the experimental parameters of Fig. 10.5 ($N = 5500$, $\bar{\omega} = 2\pi \times 32\,\text{Hz}$, $T = 90\,\text{nK}$), we obtain $\gamma_{\text{el}} = 48\,\text{s}^{-1}$. For the loss rate, we calculate $\gamma_{\text{loss}} = \bar{n}\beta = 3.4\,\text{s}^{-1}$. The ratio $\gamma_{\text{el}}/\gamma_{\text{loss}} \approx 14$ tells us that elastic collisions dominate over in-

elastic ones, but only by about one order of magnitude. Consequently, our attempts to implement evaporative cooling in the present set-up were not successful.

In view of prospective experiments involving quantum-degenerate molecular samples, it is an interesting question whether conditions can be reached for efficient evaporative cooling, which typically requires a good-to-bad collision ratio $\gamma_{el}/\gamma_{loss} \gg 100$ [202]. If we assume a reduction of the magnetic resonance detuning from the present optimum $\delta B = -17\,\text{mG}$ by just a factor of two, which corresponds to an increase of the scattering length a by a factor of two, this would increase the elastic scattering rate $\gamma_{el} \propto a^2$ by a factor of four. At the same time, according to the scaling predicted for the Dy-K mass ratio [39] $\gamma_{loss} \propto a^{1.8}$, the inelastic rate would drop by a factor of about 3.5. These two effects together would boost the good-to-bad collision ratio by a factor of 14 to $\gamma_{el}/\gamma_{loss} \approx 200$, which seems promising for evaporative cooling. To take full advantage of this in an experiment, a highly stable, homogeneous magnetic field would be necessary along with an optical trapping scheme that does not require magnetic levitation.

10.6 CONCLUSIONS AND OUTLOOK

We have studied the decay of a dense, ultracold sample of weakly bound DyK dimers stored in an optical dipole trap that operates with far red-detuned laser light. We consider the case of bosonic dimers composed of the fermionic isotopes ^{161}Dy and ^{40}K, which is of particular interest for experiments related to pairing and superfluidity in fermionic systems with mass imbalance. We have identified trap-light-induced and collisional processes as the two main sources of losses, and we have demonstrated ways to reduce these losses substantially.

Light-induced losses have been investigated in four selected spectral windows in a wide near-infrared wavelength range between 1051 and 2002 nm. We have measured corresponding loss rate coefficients, which we found to vary over four orders of magnitude with a clear general trend of strong decrease with larger wavelengths. In addition to that, we have observed resonant loss features, pointing to bound-bound electronic transitions, and plateaus of minimal losses, which are of particular interest for specific applications. Background losses seem to be present everywhere in the spectral range investigated, as our sample spectra suggest. Qualitatively, this behavior can be explained by the very complex and dense spectrum of molecular states in a dimer with complex electronic structure, which features a multitude of different potential curves. With increasing wavelength, i.e. lower photon energy, less molecular potentials become accessible and the resonance density decreases until resonant excitation is no longer possible beyond a certain point (wavelengths typically $\gtrsim 2\,\mu\text{m}$).

A comprehensive interpretation of all the features observed in our experiments would require detailed knowledge of the spectrum of molecular states, which is currently not available for the DyK system.

Collisional losses result from inelastic dimer-dimer collisions. For their observation in our experiments, it was necessary to minimize light-induced decay by carefully choosing the wavelength of the ODT (1547.21 nm regarding the available laser sources). For dimer binding energies exceeding $\sim h \times 1\,\mathrm{MHz}$, we measured collisional decay rates typical for cold dimers in high-lying vibrational states. For a much lower binding energy of about 20 kHz (closer to the center of the Feshbach resonance employed), we observed a clear suppression of inelastic collisional losses by roughly one order of magnitude. We interpret this observation in terms of the famous Pauli suppression effect that stabilizes weakly bound dimer samples and fermionic mixtures near Feshbach resonances and enables experiments in the resonance regime. In principle, much stronger loss suppression can be expected closer to the resonance, but our present experiments were technically limited by magnetic field inhomogeneities caused by the magnetic levitation gradient that was needed to keep the cold sample in the trap.

In view of future experiments, our work conveys important messages. Optically trapped molecules, in particular those with complex electronic structure, will be in general much more susceptible to detrimental light-induced processes than we are used from the bi-alkali dimers commonly used in many experiments. Thus, experiments will require a careful choice of the particular trap-light wavelength. The wavelength region around 2 μm, where high-power fiber laser sources are now available, appears to be particularly promising for eliminating light-induced losses. For our special application related to mass-imbalanced Fermi gases, we could confirm the presence of Pauli suppression of collisional losses near a Feshbach resonance. However, to take full advantage of this effect in the DyK system, a trap set-up is needed that allows one to work in a precisely controllable homogeneous magnetic field. These insights will be essential for planning a second-generation set up.

Part IV

CONCLUSIONS

WHAT HAVE WE LEARNED?

Evaporative cooling in the Dy-K mixture has been found to be mostly effective for low magnetic field, in a region below $500\,\mathrm{mG}$.

12

OUTLOOK

Part V

APPENDIX

BIBLIOGRAPHY

[1] Annual Register 1896. The University of Chicago, 1896 (cit. on p. 3).

[2] Cornelis Ravensbergen et al. Production of a degenerate Fermi-Fermi mixture of dysprosium and potassium atoms. In: *Phys. Rev. A* 98 (2018). *ibid.* 101, 059903(E) (2020)., p. 063624 (cit. on pp. 11, 18, 20–21, 27, 40–41, 49, 54–55, 93–94, 117).

[3] C. Ravensbergen et al. Accurate Determination of the Dynamical Polarizability of Dysprosium. In: *Phys. Rev. Lett.* 120 (22 2018), p. 223001 (cit. on pp. 11, 20, 55, 63, 96, 114).

[4] Marian Kreyer et al. Measurement of the dynamic polarizability of Dy atoms near the 626-nm intercombination line. In: *Phys. Rev. A* 104 (3 2021), p. 033106 (cit. on p. 11).

[5] C. Ravensbergen et al. Resonantly Interacting Fermi-Fermi Mixture of ^{161}Dy and ^{40}K. In: *Phys. Rev. Lett.* 124 (20 2020), p. 203402 (cit. on pp. 11, 15–16, 18, 22–23, 27, 29, 31–35, 37, 39, 49–50, 93–94, 115).

[6] E. Soave et al. Low-Field Feshbach Resonances and Three-Body Losses in a Fermionic Quantum Gas of ^{161}Dy. In: *Ukr. J. Phys.* 67 (2022), p. 334 (cit. on pp. 11, 16, 19, 21, 26, 31, 34–36, 49, 55, 77).

[7] Cornelis Ravensbergen. "Creation of a Fermi-Fermi mixture of dysprosium and potassium with resonant interactions." PhD thesis. University of Innsbruck, 2020 (cit. on p. 11).

[8] Slava Tzanova. "Realization and characterization of two unconventional ultracold mixtures." PhD thesis. University of Innsbruck, 2020 (cit. on p. 11).

[9] Marian Kreyer. "Double-stage magneto-optical trap system for fermionic potassium atoms." MA thesis. University of Innsbruck, 2017 (cit. on p. 11).

[10] Elisa Soave. "Interaction Properties of an Ultracold Fermi-Fermi Mixture of Dysprosium and Potassium Atoms." PhD thesis. Unijversity of Innsbruck, 2022 (cit. on p. 11).

[11] D. Dreon et al. Optical cooling and trapping of highly magnetic atoms: the benefits of a spontaneous spin polarization. In: *J. Phys. B* 50 (2017), p. 065005 (cit. on p. 12).

[12] Zhu-Xiong Ye et al. Observation of low-field Feshbach resonances between ^{161}Dy and ^{40}K. In: *Phys. Rev. A* 106 (4 2022), p. 043314 (cit. on pp. 12, 49, 54–56, 77, 93–94, 99, 101, 103, 108, 116–117).

[13]   Mingwu Lu, Seo Ho Youn, and Benjamin L. Lev. Spectroscopy of a narrow-line laser-cooling transition in atomic dysprosium. In: *Phys. Rev. A* 83 (1 2011), p. 012510 (cit. on pp. 12, 41).

[14]   M. Lu, N. Q. Burdick, and B. L. Lev. Quantum Degenerate Dipolar Fermi Gas. In: *Phys. Rev. Lett.* 108 (2012), p. 215301 (cit. on pp. 13, 54).

[15]   K. Aikawa et al. Reaching Fermi Degeneracy via Universal Dipolar Scattering. In: *Phys. Rev. Lett.* 112 (1 2014), p. 010404 (cit. on pp. 13, 54).

[16]   Milan Krstajić et al. Characterization of three-body loss in ^{166}Er and optimized production of large Bose-Einstein condensates. In: *Phys. Rev. A* 108 (6 2023), p. 063301 (cit. on p. 13).

[17]   Cheng Chin et al. Feshbach resonances in ultracold gases. In: *Rev. Mod. Phys.* 82 (2010), pp. 1225–1286 (cit. on pp. 18–19, 24, 27, 37–38, 48, 57, 92, 96, 99–100, 102, 114–117).

[18]   M. Inguscio, W. Ketterle, and C. Salomon, eds. Ultra-cold Fermi Gases. Proceedings of the International School of Physics "Enrico Fermi", Course CLXIV, Varenna, 20-30 June 2006. IOS Press, Amsterdam, 2008 (cit. on pp. 18, 48–49, 110, 114–115).

[19]   Wilhelm Zwerger, ed. The BCS-BEC Crossover and the Unitary Fermi Gas. Springer, Berlin Heidelberg, 2012 (cit. on pp. 18, 48, 92, 114).

[20]   Giancarlo Calvanese Strinati et al. The BCS-BEC crossover: From ultra-cold Fermi gases to nuclear systems. In: *Phys. Rep.* 738 (2018), pp. 1–76 (cit. on pp. 18, 48, 92, 114).

[21]   Karl-Heinz Bennemann and John B. Ketterson. Novel Superfluids: Volumes 1 and 2. Oxford University Press, Oxford, 2013, 2014 (cit. on pp. 18, 49).

[22]   K. B. Gubbels and H. T. C. Stoof. Imbalanced Fermi gases at unitarity. In: *Phys. Rep.* 525 (2013), pp. 255 –313 (cit. on pp. 18, 34, 49, 93, 115).

[23]   K. B. Gubbels, J. E. Baarsma, and H. T. C. Stoof. Lifshitz Point in the Phase Diagram of Resonantly Interacting ^{6}Li-^{40}K Mixtures. In: *Phys. Rev. Lett.* 103 (19 2009), p. 195301 (cit. on pp. 18, 49, 93, 115).

[24]   Jibiao Wang et al. Enhancement effect of mass imbalance on Fulde-Ferrell-Larkin-Ovchinnikov type of pairing in Fermi-Fermi mixtures of ultracold quantum gases. In: *Sci. Rep.* 7 (2017), p. 39783 (cit. on pp. 18, 34, 49, 93, 115).

[25]   M. Pini et al. Beyond-mean-field description of a trapped unitary Fermi gas with mass and population imbalance. In: *Phys. Rev. A* 103 (2 2021), p. 023314 (cit. on pp. 18, 34, 49, 74–75, 93, 115).

[26] Peter Fulde and Richard A. Ferrell. Superconductivity in a Strong Spin-Exchange Field. In: *Phys. Rev.* 135 (1964), A550–A563 (cit. on pp. 18, 49, 93, 115).

[27] A. I. Larkin and Yu. N. Ovchinnikov. Neodnorodnoye sostoyanie sverkhprovodnikov. In: *Zh. Eksp. Teor. Fiz.* 47 (1964). [Sov. Phys. JETP 20, 762 (1965)]., pp. 1136–1146 (cit. on pp. 18, 49, 93, 115).

[28] Leo Radzihovsky and Daniel E. Sheehy. Imbalanced Feshbach-resonant Fermi gases. In: *Rep. Prog. Phys.* 73 (2010), p. 076501 (cit. on pp. 18, 49, 93, 115).

[29] M. Taglieber et al. Quantum Degenerate Two-Species Fermi-Fermi Mixture Coexisting with a Bose-Einstein Condensate. In: *Phys. Rev. Lett.* 100, 010401 (2008), p. 010401 (cit. on pp. 18, 49, 93).

[30] E. Wille et al. Exploring an Ultracold Fermi-Fermi Mixture: Interspecies Feshbach Resonances and Scattering Properties of ^{6}Li and ^{40}K. In: *Phys. Rev. Lett.* 100, 053201 (2008), p. 053201 (cit. on pp. 18, 49, 93).

[31] A.-C. Voigt et al. Ultracold Heteronuclear Fermi-Fermi Molecules. In: *Phys. Rev. Lett.* 102 (2009). *ibid.* **1**05, 269904(E) (2010)., p. 020405 (cit. on pp. 18, 49, 93).

[32] D. Naik et al. Feshbach resonances in the ^{6}Li-^{40}K Fermi-Fermi mixture: Elastic versus inelastic interactions. In: *Eur. Phys. J. D* 65 (2011), pp. 55–65 (cit. on pp. 18, 49, 93).

[33] Hideaki Hara et al. Quantum Degenerate Mixtures of Alkali and Alkaline-Earth-Like Atoms. In: *Phys. Rev. Lett.* 106 (20 2011), p. 205304 (cit. on pp. 18, 49, 93).

[34] Alaina Green et al. Feshbach Resonances in p-Wave Three-Body Recombination within Fermi-Fermi Mixtures of Open-Shell ^{6}Li and Closed-Shell ^{173}Yb Atoms. In: *Phys. Rev. X* 10 (3 2020), p. 031037 (cit. on pp. 18, 49, 93).

[35] E. Neri et al. Realization of a cold mixture of fermionic chromium and lithium atoms. In: *Phys. Rev. A* 101 (6 2020), p. 063602 (cit. on pp. 18, 49).

[36] A. Ciamei et al. Exploring Ultracold Collisions in ^{6}Li$-^{53}$Cr Fermi Mixtures: Feshbach Resonances and Scattering Properties of a Novel Alkali-Transition Metal System. In: *Phys. Rev. Lett.* 129 (9 2022), p. 093402 (cit. on pp. 18, 49, 93).

[37] A. Ciamei et al. Double-degenerate Fermi mixtures of ^{6}Li and ^{53}Cr atoms. In: *Phys. Rev. A* 106 (5 2022), p. 053318 (cit. on pp. 18, 49, 93, 115).

[38]   D. S. Petrov, C. Salomon, and G. V. Shlyapnikov. Weakly Bound Dimers of Fermionic Atoms. In: *Phys. Rev. Lett.* 93 (2004), p. 090404 (cit. on pp. 18, 20, 34, 110, 115).

[39]   D. S. Petrov, C. Salomon, and G. V. Shlyapnikov. Diatomic molecules in ultracold Fermi gases – novel composite bosons. In: *J. Phys. B* 38 (2005), S645–S660 (cit. on pp. 18, 20, 34, 110, 115, 127–128).

[40]   M. Jag et al. Lifetime of Feshbach dimers in a Fermi-Fermi mixture of ^{6}Li and ^{40}K. In: *Phys. Rev. A* 94 (6 2016), p. 062706 (cit. on pp. 18, 20, 110, 115, 117, 121, 124–126).

[41]   Nathaniel Q. Burdick, Yijun Tang, and Benjamin L. Lev. Long-Lived Spin-Orbit-Coupled Degenerate Dipolar Fermi Gas. In: *Phys. Rev. X* 6 (3 2016), p. 031022 (cit. on pp. 19, 34, 49).

[42]   A. J. Moerdijk, B. J. Verhaar, and A. Axelsson. Resonances in ultracold collisions of ^{6}Li, ^{7}Li, and ^{23}Na. In: *Phys. Rev. A* 51 (1995), p. 4852 (cit. on p. 19).

[43]   D. S. Petrov. Three-Boson Problem near a Narrow Feshbach Resonance. In: *Phys. Rev. Lett.* 93 (2004), p. 143201 (cit. on pp. 19–20, 39, 99–100, 116).

[44]   Rianne S. Lous et al. Probing the Interface of a Phase-Separated State in a Repulsive Bose-Fermi Mixture. In: *Phys. Rev. Lett.* 120 (24 2018), p. 243403 (cit. on pp. 20, 29, 37, 100).

[45]   T. Weber et al. Bose-Einstein Condensation of Cesium. In: *Science* 299 (2003), pp. 232–235 (cit. on pp. 21, 55, 105, 114).

[46]   Rianne S. Lous et al. Thermometry of a deeply degenerate Fermi gas with a Bose-Einstein condensate. In: *Phys. Rev. A* 95 (5 2017), p. 053627 (cit. on pp. 21, 55, 96).

[47]   A. Mosk et al. Mixture of ultracold lithium and cesium atoms in an optical dipole trap. In: *Appl. Phys. B* 73 (2001), p. 791 (cit. on pp. 22–23, 27, 81).

[48]   T. Maier et al. Emergence of Chaotic Scattering in Ultracold Er and Dy. In: *Phys. Rev. X* 5 (4 2015), p. 041029 (cit. on pp. 23, 40).

[49]   V. A. Khlebnikov et al. Random to Chaotic Statistic Transformation in Low-Field Fano-Feshbach Resonances of Cold Thulium Atoms. In: *Phys. Rev. Lett.* 123 (21 2019), p. 213402 (cit. on p. 23).

[50]   Tino Weber et al. Three-Body Recombination at Large Scattering Lengths in an Ultracold Atomic Gas. In: *Phys. Rev. Lett.* 91 (12 2003), p. 123201 (cit. on p. 23).

[51]   F. Schäfer, N. Mizukami, and Y. Takahashi. Feshbach resonances of large-mass-imbalance Er-Li mixtures. In: *Phys. Rev. A* 105 (1 2022), p. 012816 (cit. on p. 24).

[52] Maykel L. González-Martínez and Piotr S. Żuchowski. Magnetically tunable Feshbach resonances in Li+Er. In: *Phys. Rev. A* 92 (2 2015), p. 022708 (cit. on pp. 24, 40).

[53] N. R. Claussen et al. Very-high-precision bound-state spectroscopy near a ^{85}Rb Feshbach resonance. In: *Phys. Rev. A* 67, 083201(R) (2003), p. 060701 (cit. on pp. 24, 100).

[54] Yaakov Yudkin and Lev Khaykovich. Efimov scenario for overlapping narrow Feshbach resonances. In: *Phys. Rev. A* 103 (6 2021), p. 063303 (cit. on p. 26).

[55] Ang Li et al. Efimov resonance position near a narrow Feshbach resonance in a ^{6}Li$-^{133}$Cs mixture. In: *Phys. Rev. A* 105 (5 2022), p. 053304 (cit. on p. 26).

[56] Michael Jag et al. Observation of a Strong Atom-Dimer Attraction in a Mass-Imbalanced Fermi-Fermi Mixture. In: *Phys. Rev. Lett.* 112 (7 2014), p. 075302 (cit. on pp. 29, 36, 49).

[57] Marko Cetina et al. Ultrafast many-body interferometry of impurities coupled to a Fermi sea. In: *Science* 354 (2016), pp. 96–99 (cit. on p. 29).

[58] C. A. Regal, M. Greiner, and D. S. Jin. Lifetime of Molecule-Atom Mixtures near a Feshbach Resonance in ^{40}K. In: *Phys. Rev. Lett.* 92, 083201 (2004), p. 083201 (cit. on pp. 34, 124).

[59] T. Bourdel et al. Measurement of the Interaction Energy near a Feshbach Resonance in a ^{6}Li Fermi Gas. In: *Phys. Rev. Lett.* 91 (2003), p. 020402 (cit. on p. 34).

[60] K. Dieckmann et al. Decay of an Ultracold Fermionic Lithium Gas near a Feshbach Resonance. In: *Phys. Rev. Lett.* 89 (2002), p. 203201 (cit. on p. 34).

[61] J. Levinsen and D. S. Petrov. Atom-dimer and dimer-dimer scattering in fermionic mixtures near a narrow Feshbach resonance. In: *Eur. Phys. J. D* 65 (2011), pp. 67–82 (cit. on p. 36).

[62] Ruth S. Bloom et al. Tests of Universal Three-Body Physics in an Ultracold Bose-Fermi Mixture. In: *Phys. Rev. Lett.* 111 (10 2013), p. 105301 (cit. on p. 37).

[63] L. J. Wacker et al. Universal Three-Body Physics in Ultracold KRb Mixtures. In: *Phys. Rev. Lett.* 117 (16 2016), p. 163201 (cit. on p. 37).

[64] C. A. Regal et al. Creation of ultracold molecules from a Fermi gas of atoms. In: *Nature (London)* 424 (2003), pp. 47–50 (cit. on pp. 37, 92).

[65] J. Herbig et al. Preparation of a pure molecular quantum gas. In: *Science* 301 (2003), p. 1510 (cit. on pp. 37, 92, 101, 105).

[66] Aden Z. Lam et al. High phase-space density gas of NaCs Feshbach molecules. In: *Phys. Rev. Research* 4 (2 2022), p. L022019 (cit. on pp. 38, 92, 99).

[67] M. Inguscio et al., eds. Quantum Matter at Ultralow Temperatures. Proceedings of the International School of Physics "Enrico Fermi", Course CXCI, Varenna, 7-15 July 2014. IOS Press, Amsterdam, 2014 (cit. on p. 48).

[68] R. Grimm et al., eds. Quantum Mixtures with Ultra-cold Atoms. Proceedings of the International School of Physics "Enrico Fermi", Course CCXI, Varenna, 18-23 July 2022. IOS Press, Amsterdam, 2025 (cit. on pp. 48, 77, 114, 152).

[69] V. Efimov. Energy levels of three resonantly interacting particles. In: *Nucl. Phys. A* 210 (1973), pp. 157–188 (cit. on p. 49).

[70] Oleg I. Kartavtsev and Anastasiya V. Malykh. Low-energy three-body dynamics in binary quantum gases. In: *J. Phys. B: At. Mol. Opt. Phys.* 40 (2007), p. 1429 (cit. on pp. 49, 93, 115).

[71] Yusuke Nishida and Shina Tan. Universal Fermi Gases in Mixed Dimensions. In: *Phys. Rev. Lett.* 101 (2008), p. 170401 (cit. on p. 49).

[72] D. Blume and K. M. Daily. Breakdown of Universality for Unequal-Mass Fermi Gases with Infinite Scattering Length. In: *Phys. Rev. Lett.* 105 (17 2010), p. 170403 (cit. on p. 49).

[73] B. Bazak and D. S. Petrov. Five-Body Efimov Effect and Universal Pentamer in Fermionic Mixtures. In: *Phys. Rev. Lett.* 118 (8 2017), p. 083002 (cit. on p. 49).

[74] Charles J. M. Mathy, Meera M. Parish, and David A. Huse. Trimers, Molecules, and Polarons in Mass-Imbalanced Atomic Fermi Gases. In: *Phys. Rev. Lett.* 106 (16 2011), p. 166404 (cit. on p. 49).

[75] J. Levinsen et al. Atom-dimer scattering and long-lived trimers in fermionic mixtures. In: *Phys. Rev. Lett.* 103 (2009), p. 153202 (cit. on p. 49).

[76] Pascal Naidon and Shimpei Endo. Efimov physics: a review. In: *Rep. Prog. Phys.* 80 (2017), p. 056001 (cit. on pp. 49, 93, 115).

[77] Chris H. Greene, P. Giannakeas, and J. Pérez-Ríos. Universal few-body physics and cluster formation. In: *Rev. Mod. Phys.* 89 (3 2017), p. 035006 (cit. on p. 49).

[78] Cosetta Baroni et al. Mediated interactions between Fermi polarons and the role of impurity quantum statistics. In: *Nat. Phys.* 20 (2024), pp. 68–73 (cit. on p. 49).

[79] Pietro Massignan et al. Polarons in atomic gases and two-dimensional semiconductors. In: (2025). arXiv: 2501.09618 [cond-mat.quant-gas] (cit. on p. 49).

[80]   W. Vincent Liu and Frank Wilczek. Interior Gap Superfluidity. In: *Phys. Rev. Lett.* 90 (2003), p. 047002 (cit. on p. 49).

[81]   Michael McNeil Forbes et al. Stability Criteria for Breached-Pair Superfluidity. In: *Phys. Rev. Lett.* 94 (2005), p. 017001 (cit. on p. 49).

[82]   M. Iskin and C. A. R. Sá de Melo. Two-Species Fermion Mixtures with Population Imbalance. In: *Phys. Rev. Lett.* 97, 100404 (2006), p. 100404 (cit. on p. 49).

[83]   M. M. Parish et al. Polarized Fermi Condensates with Unequal Masses: Tuning the Tricritical Point. In: *Phys. Rev. Lett.* 98 (16 2007), p. 160402 (cit. on p. 49).

[84]   M. A. Baranov, C. Lobo, and G. V. Shlyapnikov. Superfluid pairing between fermions with unequal masses. In: *Phys. Rev. A* 78 (2008), p. 033620 (cit. on p. 49).

[85]   Alexandros Gezerlis et al. Heavy-light fermion mixtures at unitarity. In: *Phys. Rev. Lett.* 103 (2009), p. 060403 (cit. on p. 49).

[86]   J. E. Baarsma and H. T. C. Stoof. Inhomogeneous superfluid phases in ^{6}Li-^{40}K mixtures at unitarity. In: *Phys. Rev. A* 87 (6 2013), p. 063612 (cit. on p. 49).

[87]   Ruijin Liu, Wei Wang, and Xiaoling Cui. Quartet Superfluid in Two-Dimensional Mass-Imbalanced Fermi Mixtures. In: *Phys. Rev. Lett.* 131 (19 2023), p. 193401 (cit. on p. 49).

[88]   A. Trenkwalder et al. Hydrodynamic Expansion of a Strongly Interacting Fermi-Fermi Mixture. In: *Phys. Rev. Lett.* 106 (2011), p. 115304 (cit. on pp. 49–50).

[89]   E. Soave et al. Optically trapped Feshbach molecules of fermionic ^{161}Dy and ^{40}K. In: *Phys. Rev. Res.* 5 (3 2023), p. 033117 (cit. on pp. 49, 54–57, 115–117, 121–122, 125).

[90]   S. Finelli et al. Ultracold LiCr: A New Pathway to Quantum Gases of Paramagnetic Polar Molecules. In: *PRX Quantum* 5 (2 2024), p. 020358 (cit. on pp. 49–50, 65, 76, 115, 123).

[91]   Florian Schäfer, Yuki Haruna, and Yoshiro Takahashi. Observation of Feshbach Resonances in an ^{167}Er–^{6}Li Fermi–Fermi Mixture. In: *J. Phys. Soc. Jpn.* 92 (2023), p. 054301 (cit. on p. 49).

[92]   Stefano Giorgini, Lev P. Pitaevskii, and Sandro Stringari. Theory of ultracold atomic Fermi gases. In: *Rev. Mod. Phys.* 80 (2008), pp. 1215–1273 (cit. on p. 49).

[93]   K. M. O'Hara et al. Observation of a Strongly Interacting Degenerate Fermi Gas of Atoms. In: *Science* 298 (2002), pp. 2179–2182 (cit. on pp. 49–50).

[94]   J. Kinast et al. Evidence for Superfluidity in a Resonantly Interacting Fermi Gas. In: *Phys. Rev. Lett.* 92 (2004), p. 150402 (cit. on p. 49).

[95] M. Bartenstein et al. Collective Excitations of a Degenerate Gas at the BEC-BCS Crossover. In: *Phys. Rev. Lett.* 92 (2004), p. 203201 (cit. on p. 49).

[96] A. Altmeyer et al. Dynamics of a strongly interacting Fermi gas: The radial quadrupole mode. In: *Phys. Rev. A* 76, 033610 (2007), p. 033610 (cit. on p. 49).

[97] M. J. Wright et al. Finite-temperature collective dynamics of a Fermi gas in the BEC-BCS crossover. In: *Phys. Rev. Lett.* 99 (2007), p. 150403 (cit. on p. 49).

[98] S. Nascimbène et al. Collective Oscillations of an Imbalanced Fermi Gas: Axial Compression Modes and Polaron Effective Mass. In: *Phys. Rev. Lett.* 103 (17 2009), p. 170402 (cit. on p. 49).

[99] Meng Khoon Tey et al. Collective Modes in a Unitary Fermi Gas across the Superfluid Phase Transition. In: *Phys. Rev. Lett.* 110 (5 2013), p. 055303 (cit. on p. 49).

[100] Ariel Sommer et al. Universal spin transport in a strongly interacting Fermi gas. In: *Nature (London)* 472 (2011), pp. 201–204 (cit. on pp. 50, 75, 78).

[101] Ariel Sommer, Mark Ku, and Martin W. Zwierlein. Spin transport in polaronic and superfluid Fermi gases. In: *New J. Phys.* 13 (2011), p. 055009 (cit. on pp. 50, 78).

[102] G. Valtolina et al. Exploring the ferromagnetic behaviour of a repulsive Fermi gas through spin dynamics. In: *Nat. Phys.* 13 (2017), pp. 704–709 (cit. on pp. 50, 75).

[103] L. Vichi and S. Stringari. Collective oscillations of an interacting trapped Fermi gas. In: *Phys. Rev. A* 60 (1999), pp. 4734–4737 (cit. on p. 51).

[104] S. D. Gensemer and D. S. Jin. Transition from collisionless to hydrodynamic behavior in an ultracold Fermi gas. In: *Phys. Rev. Lett.* 87 (2001), p. 173201 (cit. on pp. 51, 65, 76–77, 81).

[105] F. Ferlaino et al. Dipolar oscillations in a quantum degenerate Fermi-Bose atomic mixture. In: *J. Opt. B: Quantum Semiclassic. Opt.* 5 (2003), S3 (cit. on pp. 51, 65, 76–77).

[106] S. Chiacchiera, T. Macrì, and A. Trombettoni. Dipole oscillations in fermionic mixtures. In: *Phys. Rev. A* 81 (3 2010), p. 033624 (cit. on pp. 51, 77).

[107] Yoji Asano, Shohei Watabe, and Tetsuro Nikuni. Dipole oscillation of a trapped Bose-Fermi-mixture gas in collisionless and hydrodynamic regimes. In: *Phys. Rev. A* 101 (1 2020), p. 013611 (cit. on pp. 51, 77).

[108] Masato Narushima, Shohei Watabe, and Tetsuro Nikuni. Density and spin modes in imbalanced normal Fermi gases from collisionless to hydrodynamic regime. In: *J. Phys. B: At. Mol. Opt. Phys.* 51 (2018), p. 055202 (cit. on p. 51).

[109] Thomas Lepers et al. Numerical solution of the Boltzmann equation for the collective modes of trapped Fermi gases. In: *Phys. Rev. A* 82 (2 2010), p. 023609 (cit. on pp. 51, 74).

[110] O. Goulko, F. Chevy, and C. Lobo. Boltzmann equation simulation for a trapped Fermi gas of atoms. In: *New. J. Phys.* 14 (2012), p. 073036 (cit. on pp. 51, 74).

[111] I. Ferrier-Barbut et al. A mixture of Bose and Fermi superfluids. In: *Science* 345 (2014), pp. 1035–1038 (cit. on p. 53).

[112] Yu-Ping Wu et al. Coupled dipole oscillations of a mass-imbalanced Bose-Fermi superfluid mixture. In: *Phys. Rev. B* 97 (2 2018), p. 020506 (cit. on p. 53).

[113] Parinaz Barakhshan et al. *Portal for High-Precision Atomic Data and Computation* (version 2.0). University of Delaware, Newark, DE, USA. 2022. eprint: https://www.udel.edu/atom (cit. on p. 55).

[114] V. A. Dzuba, V. V. Flambaum, and Benjamin L. Lev. Dynamic polarizabilities and magic wavelengths for dysprosium. In: *Phys. Rev. A* 83 (3 2011), p. 032502 (cit. on p. 55).

[115] H. Li et al. Optical trapping of ultracold dysprosium atoms: transition probabilities, dynamic dipole polarizabilities and van der Waals C_6 coefficients. In: *J. Phys. B: At. Mol. Opt. Phys.* 50 (2017), p. 014005 (cit. on p. 55).

[116] Marion Delehaye et al. Critical Velocity and Dissipation of an Ultracold Bose-Fermi Counterflow. In: *Phys. Rev. Lett.* 115 (26 2015), p. 265303 (cit. on pp. 65, 76).

[117] Federico Carlini and Sandro Stringari. Spin drag and fast response in a quantum mixture of atomic gases. In: *Phys. Rev. A* 104 (2 2021), p. 023301 (cit. on p. 77).

[118] Hiroyuki Tajima, Alessio Recati, and Yoji Ohashi. Spin-dipole mode in a trapped Fermi gas near unitarity. In: *Phys. Rev. A* 101 (1 2020), p. 013610 (cit. on p. 78).

[119] T. Köhler, K. Goral, and P. S. Julienne. Production of cold molecules via magnetically tunable Feshbach resonances. In: *Rev. Mod. Phys.* 78 (2006), p. 1311 (cit. on pp. 92, 96, 114–115).

[120] Roahn Wynar et al. Molecules in a Bose-Einstein Condensate. In: *Science* 287 (2000), pp. 1016–1019 (cit. on p. 92).

[121] E. A. Donley et al. Atom-molecule coherence in a Bose-Einstein condensate. In: *Nature (London)* 417 (2002), pp. 529–533 (cit. on pp. 92, 100).

[122] K. Xu et al. Formation of Quantum-Degenerate Sodium Molecules. In: *Phys. Rev. Lett.* 91, 210402 (2003) (cit. on p. 92).

[123] Stephan Dürr et al. Observation of Molecules Produced from a Bose-Einstein Condensate. In: *Phys. Rev. Lett.* 92, 020406 (2004), p. 020406 (cit. on p. 92).

[124] Kevin E. Strecker, Guthrie B. Partridge, and Randall G. Hulet. Conversion of an Atomic Fermi Gas to a Long-Lived Molecular Bose Gas. In: *Phys. Rev. Lett.* 91 (2003), p. 080406 (cit. on p. 92).

[125] J. Cubizolles et al. Production of Long-Lived Ultracold Li_2 Molecules from a Fermi Gas. In: *Phys. Rev. Lett.* 91 (2003), p. 240401 (cit. on pp. 92, 124).

[126] S. Jochim et al. Pure Gas of Optically Trapped Molecules Created from Fermionic Atoms. In: *Phys. Rev. Lett* 91 (2003), p. 240402 (cit. on pp. 92, 124, 126).

[127] S. Jochim et al. Bose-Einstein Condensation of Molecules. In: *Science* 302 (2003), pp. 2101–2103 (cit. on pp. 92, 114).

[128] M. Greiner, C. A. Regal, and D. S. Jin. Emergence of a molecular Bose-Einstein Condensate from a Fermi gas. In: *Nature (London)* 426 (2003), pp. 537–540 (cit. on pp. 92, 114).

[129] M. W. Zwierlein et al. Observation of Bose-Einstein Condensation of Molecules. In: *Phys. Rev. Lett.* 91 (2003), p. 250401 (cit. on pp. 92, 114).

[130] C. A. Regal, M. Greiner, and D. S. Jin. Observation of Resonance Condensation of Fermionic Atom Pairs. In: *Phys. Rev. Lett.* 92 (2004), p. 040403 (cit. on pp. 92, 114).

[131] M. W. Zwierlein et al. Vortices and superfluidity in a strongly interacting Fermi gas. In: *Nature (London)* 435 (2005), pp. 1047–1051 (cit. on p. 92).

[132] C. Ospelkaus et al. Ultracold Heteronuclear Molecules in a 3D Optical Lattice. In: *Phys. Rev. Lett.* 97, 120402 (2006), p. 120402 (cit. on p. 92).

[133] C. Weber et al. Association of ultracold double-species bosonic molecules. In: *Phys. Rev. A* 78 (2008), 061601(R) (cit. on pp. 92, 100).

[134] F. M. Spiegelhalder et al. All-optical production of a degenerate mixture of ^{6}Li and ^{40}K and creation of heteronuclear molecules. In: *Phys. Rev. A* 81 (2010), p. 043637 (cit. on p. 92).

[135] Cheng-Hsun Wu et al. Ultracold Fermionic Feshbach Molecules of ^{23}Na^{40}K. In: *Phys. Rev. Lett.* 109 (8 2012), p. 085301 (cit. on p. 92).

[136] Myoung-Sun Heo et al. Formation of ultracold fermionic NaLi Feshbach molecules. In: *Phys. Rev. A* 86 (2 2012), p. 021602 (cit. on p. 92).

[137] Michael P. Köppinger et al. Production of optically trapped ^{87}RbCs Feshbach molecules. In: *Phys. Rev. A* 89 (3 2014), p. 033604 (cit. on pp. 92, 97, 109).

[138] Tetsu Takekoshi et al. Ultracold Dense Samples of Dipolar RbCs Molecules in the Rovibrational and Hyperfine Ground State. In: *Phys. Rev. Lett.* 113 (20 2014), p. 205301 (cit. on pp. 92, 123).

[139] Fudong Wang et al. Formation of ultracold NaRb Feshbach molecules. In: *New J. Phys.* 17 (2015), p. 035003 (cit. on p. 92).

[140] S. Dürr, T. Volz, and G. Rempe. Dissociation of ultracold molecules with Feshbach resonances. In: *Phys. Rev. A* 70 (2004), 031601(R) (cit. on p. 98).

[141] L. De Marco et al. A degenerate Fermi gas of polar molecules. In: *Science* 363 (2019), pp. 853–856 (cit. on p. 99).

[142] Marcel Duda et al. Transition from a polaronic condensate to a degenerate Fermi gas of heteronuclear molecules. In: *Nat. Phys.* 19 (2023), pp. 720–725 (cit. on p. 99).

[143] E. Braaten and H.-W. Hammer. Universality in few-body systems with large scattering length. In: *Phys. Rep.* 428 (2006), pp. 259–390 (cit. on pp. 100, 116).

[144] I. Bloch, J. Dalibard, and W. Zwerger. Many-body physics with ultracold gases. In: *Rev. Mod. Phys.* 80 (2008), p. 885 (cit. on p. 100).

[145] S. T. Thompson, E. Hodby, and C. E. Wieman. Ultracold molecule production via a resonant oscillating magnetic field. In: *Phys. Rev. Lett.* 95, 190404 (2005), p. 190404 (cit. on p. 100).

[146] Thomas M. Hanna, Thorsten Köhler, and Keith Burnett. Association of molecules using a resonantly modulated magnetic field. In: *Phys. Rev. A* 75, 013606 (2007), p. 013606 (cit. on p. 100).

[147] Abhishek Mohapatra and Eric Braaten. Harmonic and subharmonic association of universal dimers in a thermal gas. In: *Phys. Rev. A* 92 (1 2015), p. 013425 (cit. on p. 100).

[148] M. Mark et al. Spectroscopy of ultracold trapped cesium Feshbach molecules. In: *Phys. Rev. A* 76 (2007), p. 042514 (cit. on pp. 101, 114).

[149] G. M. Falco and H. T. C. Stoof. Atom-molecule theory of broad Feshbach resonances. In: *Phys. Rev. A* 71 (6 2005), p. 063614 (cit. on p. 102).

[150] G. B. Partridge et al. Molecular Probe of Pairing in the BEC-BCS Crossover. In: *Phys. Rev. Lett.* 95 (2005), p. 020404 (cit. on pp. 106, 108, 122).

[151] Amodsen Chotia et al. Long-Lived Dipolar Molecules and Feshbach Molecules in a 3D Optical Lattice. In: *Phys. Rev. Lett.* 108 (8 2012), p. 080405 (cit. on pp. 109, 115, 122).

[152] Jessie T. Zhang et al. Forming a Single Molecule by Magnetoassociation in an Optical Tweezer. In: *Phys. Rev. Lett.* 124 (25 2020), p. 253401 (cit. on pp. 109, 115).

[153] Stefan J. Spence. "Assembling Single RbCs Molecules with Optical Tweezers." PhD thesis. Durham University, 2023 (cit. on pp. 109, 115).

[154] R. Thomas and N. Kjærgaard. A digital feedback controller for stabilizing large electric currents to the ppm level for Feshbach resonance studies. In: *Rev. Sci. Instrum.* 91 (2020), p. 034705 (cit. on p. 111).

[155] Steven Chu et al. Experimental Observation of Optically Trapped Atoms. In: *Phys. Rev. Lett.* 57 (3 1986), pp. 314–317 (cit. on p. 114).

[156] R. Grimm, M. Weidemüller, and Yu. B. Ovchinnikov. Optical dipole traps for neutral atoms. In: *Adv. At. Mol. Opt. Phys.* 42 (2000), p. 95 (cit. on pp. 114, 124).

[157] Louise Wolswijk et al. *Trapping, manipulating and probing ultracold atoms: a quantum technologies tutorial*. 2025. arXiv: 2510.20790 [cond-mat.quant-gas] (cit. on p. 114).

[158] Andrew D. Ludlow et al. Optical atomic clocks. In: *Rev. Mod. Phys.* 87 (2 2015), pp. 637–701 (cit. on p. 114).

[159] Y. A. Yang et al. Clock Precision beyond the Standard Quantum Limit at 10^{-18} Level. In: *Phys. Rev. Lett.* 135 (19 2025), p. 193202 (cit. on p. 114).

[160] T. A. Zheng et al. Measurement of the Electric Dipole Moment of ^{171}Yb Atoms in an Optical Dipole Trap. In: *Phys. Rev. Lett.* 129 (8 2022), p. 083001 (cit. on p. 114).

[161] Premjith Thekkeppatt et al. Measurement of the *g* Factor of Ground-State ^{87}Sr at the Parts-per-Million Level Using Co-Trapped Ultracold Atoms. In: *Phys. Rev. Lett.* 135 (19 2025), p. 193001 (cit. on p. 114).

[162] Antoine Browaeys and Thierry Lahaye. Many-body physics with individually controlled Rydberg atoms. In: *Nat. Phys.* 16 (2020), pp. 132–142 (cit. on p. 114).

[163] Adam M. Kaufman and Kang-Kuen Ni. Quantum science with optical tweezer arrays of ultracold atoms and molecules. In: *Nat. Phys.* 17 (2021), pp. 1324–1333 (cit. on p. 114).

[164] Shraddha Anand et al. A dual-species Rydberg array. In: *Nat. Phys.* 20 (2024), pp. 1744–1750 (cit. on p. 114).

[165] D. S. Grün et al. Optical Tweezer Arrays of Erbium Atoms. In: *Phys. Rev. Lett.* 133 (22 2024), p. 223402 (cit. on p. 114).

[166] M. Inguscio, S. Stringari, and C. Wieman, eds. Bose-Einstein Condensation in Atomic Gases. Proceedings of the International School of Physics "Enrico Fermi", Course CXL, Varenna, 7-17 July 1998. North Holland, Amsterdam, 1999 (cit. on p. 114).

[167] Yosuke Takasu et al. Spin-singlet Bose-Einstein condensation of two-electron atoms. In: *Phys. Rev. Lett.* 91 (2003), p. 040404 (cit. on p. 114).

[168] A Griesmaier et al. Bose-Einstein condensation of chromium. In: *Phys. Rev. Lett.* 94 (2005), p. 160401 (cit. on p. 114).

[169] Kevin M. Jones et al. Ultracold photoassociation spectroscopy: Long-range molecules and atomic scattering. In: *Rev. Mod. Phys.* 78, 483 (2006), p. 483 (cit. on pp. 114, 120).

[170] J. Deiglmayr et al. Formation of Ultracold Polar Molecules in the Rovibrational Ground State. In: *Phys. Rev. Lett.* 101, 133004 (2008), p. 133004 (cit. on p. 114).

[171] C. Chin et al. Observation of Feshbach-like resonances in collisions between ultracold molecules. In: *Phys. Rev. Lett.* 94 (2005), p. 123201 (cit. on p. 114).

[172] F. Ferlaino et al. Collisions between tunable halo dimers: Exploring an elementary four-body process with identical bosons. In: *Phys. Rev. Lett.* 101, 023201 (2008), p. 023201 (cit. on p. 114).

[173] K. K. Ni et al. Dipolar collisions of polar molecules in the quantum regime. In: *Nature (London)* 464 (2010), pp. 1324–1328 (cit. on p. 114).

[174] K. Winkler et al. Coherent optical transfer of Feshbach molecules to a lower vibrational state. In: *Phys. Rev. Lett.* 98, 043201 (2007) (cit. on p. 114).

[175] F. Lang et al. Cruising through molecular bound-state manifolds with radiofrequency. In: *Nat. Phys.* 4 (2008), p. 223 (cit. on p. 114).

[176] K.-K. Ni et al. A High Phase-Space-Density Gas of Polar Molecules. In: *Science* 322 (2008), pp. 231–235 (cit. on pp. 114, 123).

[177] F. Lang et al. Ultracold Triplet Molecules in the Rovibrational Ground State. In: *Phys. Rev. Lett.* 101, 133005 (2008), p. 133005 (cit. on p. 114).

[178] J. G. Danzl et al. An ultracold high-density sample of rovibronic ground-state molecules in an optical lattice. In: *Nat. Phys.* 6 (2010), p. 265 (cit. on p. 114).

[179] M. Bartenstein et al. Crossover from a Molecular Bose-Einstein Condensate to a Degenerate Fermi Gas. In: *Phys. Rev. Lett.* 92 (2004), p. 120401 (cit. on p. 114).

[180]   M. W. Zwierlein et al. Condensation of Pairs of Fermionic Atoms near a Feshbach Resonance. In: *Phys. Rev. Lett.* 92 (2004), p. 120403 (cit. on p. 114).

[181]   Z. Zhang et al. Transition from an atomic to a molecular Bose–Einstein condensate. In: *Nature (London)* 592 (2021), p. 708 (cit. on p. 115).

[182]   Niccolo Bigagli et al. Observation of Bose–Einstein condensation of dipolar molecules. In: *Nature (London)* 631 (2024), pp. 289–293 (cit. on p. 115).

[183]   Zhaopeng Shi et al. *Bose-Einstein condensate of ultracold sodium-rubidium molecules with tunable dipolar interactions.* 2025. arXiv: 2508.20518 [cond-mat.quant-gas] (cit. on p. 115).

[184]   William B. Cairncross et al. Assembly of a Rovibrational Ground State Molecule in an Optical Tweezer. In: *Phys. Rev. Lett.* 126 (12 2021), p. 123402 (cit. on p. 115).

[185]   Daniel K. Ruttley et al. Formation of Ultracold Molecules by Merging Optical Tweezers. In: *Phys. Rev. Lett.* 130 (22 2023), p. 223401 (cit. on p. 115).

[186]   Loïc Anderegg et al. An optical tweezer array of ultracold molecules. In: *Science* 365 (2019), pp. 1156–1158 (cit. on p. 115).

[187]   Nathaniel B. Vilas et al. An optical tweezer array of ultracold polyatomic molecules. In: *Nature (London)* 628 (2024), pp. 282–286 (cit. on p. 115).

[188]   Zhu-Xiong Ye et al. Dipole-mode spectrum and hydrodynamic crossover in a resonantly interacting two-species fermion mixture. In: *Phys. Rev. Res.* 7 (2 2025), p. 023259 (cit. on p. 115).

[189]   M. Zaccanti. Mass-imbalanced Fermi mixtures with resonant interactions. In: *in Ref. [68]* (2025) (cit. on p. 115).

[190]   S. T. Thompson, E. Hodby, and C. E. Wieman. Spontaneous dissociation of ^{85}Rb Feshbach molecules. In: *Phys. Rev. Lett.* 94 (2005), p. 020401 (cit. on p. 117).

[191]   Shunji Kasahara et al. Doppler-free optical–optical double resonance polarization spectroscopy of the ^{39}K^{85}Rb $1^1\Pi$ and $2^1\Pi$ states. In: *J. Chem. Phys.* 111 (1999), pp. 8857–8866 (cit. on p. 120).

[192]   Mingyang Guo et al. Creation of an Ultracold Gas of Ground-State Dipolar ^{23}Na^{87}Rb Molecules. In: *Phys. Rev. Lett.* 116 (20 2016), p. 205303 (cit. on p. 120).

[193]   Mingyang Guo et al. High-resolution molecular spectroscopy for producing ultracold absolute-ground-state ^{23}Na^{87}Rb molecules. In: *Phys. Rev. A* 96 (5 2017), p. 052505 (cit. on p. 120).

[194]   Claire Warner et al. Efficient pathway to NaCs ground state molecules. In: *New J. Phys.* 25 (2023), p. 053036 (cit. on p. 123).

[195] , R. Guérout, and O. Dulieu. Ground- and excited-state properties of the polar and paramagnetic RbSr molecule: A comparative study. In: *Phys. Rev. A* 90 (1 2014), p. 012507 (cit. on p. 123).

[196] T. Takekoshi, B. M. Patterson, and R. J. Knize. Observation of optically trapped cold cesium molecules. In: *Phys. Rev. Lett.* 81 (1 1998), pp. 5105–5108 (cit. on p. 124).

[197] Bo Gao. Universal Model for Exoergic Bimolecular Reactions and Inelastic Processes. In: *Phys. Rev. Lett.* 105 (26 2010), p. 263203 (cit. on p. 126).

[198] Paul S. Julienne, Thomas M. Hanna, and Zbigniew Idziaszek. Universal ultracold collision rates for polar molecules of two alkali-metal atoms. In: *Phys. Chem. Chem. Phys.* 13 (1 2011), pp. 19114–19124 (cit. on p. 126).

[199] Goulven Quéméner et al. Universalities in ultracold reactions of alkali-metal polar molecules. In: *Phys. Rev. A* 84 (1 2011), p. 062703 (cit. on p. 126).

[200] Cheng Chin and Rudolf Grimm. Thermal equilibrium and efficient evaporation of an ultracold atom-molecule mixture. In: *Phys. Rev. A* 69, 033612 (1 2004), p. 033612 (cit. on p. 126).

[201] B. Marcelis et al. Collisional properties of weakly bound heteronuclear dimers. In: *Phys. Rev. A* 77 (1 2008), p. 032707 (cit. on p. 127).

[202] W. Ketterle and N. J. van Druten. Evaporative Cooling of Trapped Atoms. In: *Adv. At. Mol. Opt. Phys.* Advances In Atomic, Molecular, and Optical Physics 37 (1 1996), p. 181 (cit. on p. 128).

DECLARATION

Put your declaration here.

Innsbruck, February 2025

_____

Alberto Canali

We have seen that computer programming is an art,
because it applies accumulated knowledge to the world,
because it requires skill and ingenuity, and especially
because it produces objects of beauty.

— **knuth:1974 [knuth:1974]**

ACKNOWLEDGMENTS

Put your acknowledgments here.

Many thanks to everybody who already sent me a postcard!

Regarding the typography and other help, many thanks go to Marco Kuhlmann, Philipp Lehman, Lothar Schlesier, Jim Young, Lorenzo Pantieri and Enrico Gregorio, Jörg Sommer, Joachim Köstler, Daniel Gottschlag, Denis Aydin, Paride Legovini, Steffen Prochnow, Nicolas Repp, Hinrich Harms, Roland Winkler, Jörg Weber, Henri Menke, Claus Lahiri, Clemens Niederberger, Stefano Bragaglia, Jörn Hees, Scott Lowe, Dave Howcroft, José M. Alcaide, David Carlisle, Ulrike Fischer, Hugues de Lassus, Csaba Hajdu, Dave Howcroft, Anonymous, Konrad Höffner, and the whole LATEX-community for support, ideas and some great software.

Regarding LyX: The LyX port was intially done by *Nicholas Mariette* in March 2009 and continued by *Ivo Pletikosić* in 2011. Thank you very much for your work and for the contributions to the original style.